Trinity College Dublin

Doctoral Thesis

Spectroscopy and scattering of mesons containing charm quarks from lattice QCD

Author:

Graham Moir

Supervisor:

Dr. Michael Peardon

A thesis submitted in fulfilment of the requirements

for the degree of Doctor of Philosophy

in the

School of Mathematics

Trinity College Dublin

November 2013

Declaration of Authorship

This thesis has not been submitted as an exercise for a degree at this or any other university. It is entirely the candidate's own work unless where stated. The candidate agrees that the Library may lend or copy the thesis upon request. This permission covers only single copies made for study purposes, subject to normal conditions of acknowledgement.

This study was performed for the Hadron Spectrum Collaboration. Most of the material presented in chapters $2-7$ has been published in

- L. Liu *et al.* JHEP 1207, 126, (2012).
- G. Moir *et al.* JHEP 1305, 021, (2013).

Signed: Graham Moir

Abstract

Spectroscopy and scattering of mesons containing charm quarks from lattice QCD

by Graham Moir

We present excited spectra of mesons containing charm-light (D), charm-strange (D_s) and charm-charm (charmonium) combinations. We perform these spectroscopic calculations on two volumes, $16^3 \times 128$ and $24^3 \times 128$, of dynamical $N_f = 2 + 1$ configurations generated by the Hadron Spectrum Collaboration. These ensembles have unphysically-heavy degenerate up and down quarks, resulting in a pion mass of ~ 391 MeV. Our use of distillation and the variational method combined with a large basis of carefully constructed interpolators allows us to extract and reliably identify the continuum spin of an extensive set of states up to $J \leq 4$, while also allowing access to explicit gluonic degrees of freedom. For the first time in a lattice QCD calculation, we extract charmonium states with exotic quantum numbers 0^{+-}, 1^{-+} and 2^{+-}, and in all three sectors, we identify the lightest hybrid supermultiplet and evidence for an excited hybrid supermultiplet. Using a non-relativistic interpretation of some of our interpolators in the open-charm sectors, we calculate mixing angles for P-wave, D-wave and the hybrid 1^-, spin-singlet triplet states. We also present preliminary results for the isospin, $I = 3/2$, $D\pi$ multi-particle spectrum and map out, via the Lüscher formalism, the $l = 0$ elastic scattering phase shift. As expected we do not find a resonance in this channel.

Acknowledgements

First and foremost, I would like to thank my supervisor Dr. Michael Peardon, who not only introduced me to the world of lattice field theory, but whose friendliness, guidance and support was essential to all aspects of this work.

A big thank you is also warranted for Dr. Sinéad Ryan for her invaluable help and input during this work.

I would like to extend a special thank you to Dr. Christopher Thomas, who gave up so much of his time to answer my endless questions. Without his enthusiasm and insight this work would not have been possible.

I would also like to thank Dr. Darran McManus who organised the original 'black-board sessions' where I learnt a lot of interesting physics both in and outside of lattice field theory.

I extend a warm thank you to the other members of the lattice group: Stefan Sint, Pol Vilaseca, Tim Harris, Mattia Dalla Brida, Aoife Kelly, Liuming Liu, Nicholas Garron and John Bulava, who made studying lattice field theory at Trinity College very enjoyable.

I save my biggest thank you for my family; John, Aisling, Shannon, Dylan and Cían, and my girlfriend Siobhán, for their love and support over the last three years.

Contents

List of Figures

List of Tables

Chapter 1

Introduction

Since Maxwell's paper entitled 'A Dynamical Theory of the Electromagnetic Field' [1], theoretical physics has undergone many revolutions, and has produced one of the most successful physical theories to date; the Standard Model of particle physics. The Standard Model is written in the language of Quantum Field Theory, which is a mathematical framework that combines two of the major developments of the twentieth century; Special Relativity [2] and Quantum Mechanics [3–5]. The formulation of these two theories has led to some drastic changes in the way we view nature. For instance, Special Relativity leads to many unintuitive consequences, such as time dilation and length contraction, and has led to the inception of space-time as the fabric of the universe [6], while Quantum Mechanics brings with it the difficulty of interpretation; the famous (or infamous) 'no-go' theorems of Bell [7] and of Kochen and Specker [8] show the impossibility of using local hidden variables to describe the theory and seem to suggest an inherit randomness of the universe or a *spooky action at a distance* of entangled particles.

As previously mentioned, the marriage of these remarkable theories is achieved through Quantum Field Theory which was developed throughout the first half of the twentieth century. The first reasonably complete theory of Quantum Electrodynamics (QED) was achieved by Paul Dirac in the late 1920's [9]. As the theory progressed, it was clear that it possessed one major flaw; the self-energy and vacuum polarization effects led to divergences. This seemingly fatal problem was solved in the late 1940's by influential physicists such as Dyson, Schwinger, Tomonaga, Bethe and Feynman via the introduction of the concept of renormalisation which swept away the infinities that plagued QED by a redefinition of what is meant by the observable mass and charge of a particle (see [10] and refs therein).

There are many ways to formulate a Quantum Field Theory such as canonical quantization, the path integral and BRST quantization. Since the path integral approach produces Feynman rules in their final Lorentz covariant form, it is arguably the most elegant. In this approach one calculates expectation values of observables $\mathcal{O}$ via:

$$\langle 0 \,|\mathcal{O}(\phi)|\, 0\rangle = \int_A \mathcal{D}\phi \mathcal{O}(\phi) e^{iS(\phi)} \,, \tag{1.1}$$

where the integral is taken over the space of all possible field configurations A. $\mathcal{D}(\phi)$ is the measure on this space and the action $S(\phi)$ is given by an integral of the Lagrangian density over the desired space-time. When the action contains no interaction terms, the path integral can be performed exactly due to its Gaußian nature. On the other-hand, when describing interacting theories, the path integral looses its Gaußian form and alternate methods are required. Expanding the exponential of the path integral produces a series of free path integrals that can then be solved exactly. For this asymptotic expansion to be feasible, the coefficient of the interaction term in the action, known as the coupling, must be small enough so that each term in the series contributes less than its predecessor. This method, known as perturbation

theory, has had immense success in QED where it has matched experimental results to an incredible degree of accuracy. This consistency with experiment has led many physicists to disregard or simply ignore a theorem by Rudolf Haag [11] that was generalized by Arthur Wightman [12] to show that a single Hilbert space representation is insufficient for describing both free and interacting fields, and an equivalent theorem by Robert Schrader [13] that applies to the path integral formulation.

Following the success of describing the electromagnetic force as a quantum theory of fields, the attention of many theorists turned to the application of QFT to the remaining known forces of nature. The early 1960's brought about two major developments, each of which brought closer the unification of Electromagnetism and the Weak force. The first of these is known as the Nambu-Goldstone theorem [14, 15], which implies that the spontaneous breaking of a global symmetry brings with it massless bosons. The second was the use of the gauge principle as a basis to construct QFT's of interacting fundamental fields [16]. However, in the quest to unify the Electromagnetic and Weak forces, there was still one missing ingredient; the Higgs-Mechanism. Although named after Peter Higgs, it was developed by a number of physicists across a number of papers [17–21]. With all the required pieces in place, the theory of Electroweak interactions was constructed in the late 1960's for which Salam, Weinberg and Glashow were awarded the Nobel prize. The unification is based on the $SU(2) \times U(1)$ gauge group. At high enough energy, the electroweak symmetry is unbroken and all fundamental particles are massless. As the universe cools below a critical temperature, the symmetry is broken and the W and Z bosons acquire a mass.

With the Electromagnetic and Weak forces unified within a single gauge theory, the focus of many physicists turned quickly to the strong sector. By then, Faddeev and Popov had already shown how to construct Feynman rules for Yang-Mills gauge

theories [22], and Feynman had begun to construct the partonic picture of hadron collisions. A Lagrangian based on the $SU(3)$ gauge group describing the dynamical behaviour of the strong force was constructed in the early 1970's and brought with it two peculiar properties. The first of these, known as asymptotic freedom, was discovered independently by Politzer, and by Gross and Wilczek, and can be seen by calculating the one loop β-function of Quantum Chromodynamics (QCD) [23]. It is a consequence of the fact that the anti-screening effect of the gluons overcomes the screening effect of the quarks, at high energies. The second of these unusual properties is known as confinement. It implies that all physical observables are colour singlets, hence restricting experimentalists to indirect methods when attempting to detect colour charged objects. Although unproven, confinement is widely accepted as a property of QCD due to strong evidence arising from experiment and from non-perturbative methods such as Lattice QCD [24].

The Standard Model of particle physics, as it now stands, is based upon the unification of the strong and electro-weak sectors. Its gauge structure follows that of the $SU(3) \times SU(2) \times U(1)$ group and it is consistent with all experimental facts to date. While the recent discovery of a higgs-like boson at 125 GeV [25, 26] has rendered the Standard Model complete as a theory, there are still many open questions surrounding particle physics such as the strong CP and hierarchy problems, or how to unify gravity with the other forces in a quantum setting. Many extensions to the Standard Model exist and attempt to address some of these problems but, as of yet, there is no *Grand Unified Theory of Everything.*

This thesis is devoted to the exploration of the charm sector of QCD via the non-perturbative framework of lattice field theory, but before we discuss its lattice formulation let us briefly review QCD in the continuum.

1.1 Quantum Chromodynamics

The gauge group of QCD is based upon empirical evidence for the existence of a *colour* charge. Both theoretical and experimental evidence points to the existence of three such colours, suggesting that the fundamental matter fields should belong to a three dimensional irreducible representation of a gauge group that should be exactly realized in nature. From all of the simple compact Lie groups, only four have three dimensional irreducible representations (irreps). Of these, three are isomorphic to one another; $SO(3) \backsimeq SU(2) \backsimeq Sp(1)$, while the fourth is $SU(3)$. Experimental evidence requires that quarks and anti-quarks should be different states. This condition implies that the triplet representation of the gauge group should be complex, that is, $\underline{3}^* \neq \underline{3}$. Only $SU(3)$ survives this condition since the triplet representation of $SO(3)$ is real. The well known $SU(3)$ decompositions

$$\underline{3} \otimes \underline{3}^* = \underline{1} \oplus \underline{8} \tag{1.2}$$

$$\underline{3} \otimes \underline{3} = \underline{3}^* \oplus \underline{6} \tag{1.3}$$

$$\underline{3} \otimes \underline{3} \otimes \underline{3} = \underline{1} \oplus \underline{8} \oplus \underline{8} \oplus \underline{10} \tag{1.4}$$

$$\underline{3} \otimes \underline{3} \otimes \underline{3} \otimes \underline{3} = \underline{3} \oplus \underline{3} \oplus \underline{3} \oplus \underline{6} \oplus \underline{6}^* \oplus \underline{15} \oplus \underline{15} \oplus \underline{15} \oplus \underline{15}^* \tag{1.5}$$

guarantee that there are colour singlet states in the form of mesons ($q\bar{q}$) and baryons (qqq), while also ruling out the possibility of some combinations such as diquark (qq, $\bar{q}\bar{q}$) or four-quark states ($qqqq$, $\bar{q}\bar{q}\bar{q}\bar{q}$).

Assuming that the strong force can be described by a gauge theory based on the group $SU(3)$ with colour triplet matter fields, of which there are empirically six,

restricts us to the following Lagrangian density

$$\mathcal{L} = \sum_{f=1}^{6} \bar{q}_f (i\gamma^\mu D_\mu - m_f) q_f - \frac{1}{4} \sum_{a=1}^{8} F_a^{\mu\nu} F_{\mu\nu}^a \ , \tag{1.6}$$

where γ_μ are the Dirac matrices following the Dirac algebra $\{\gamma_\mu, \gamma_\nu\} = 2\eta_{\mu\nu}$. D_μ is the covariant derivative

$$D_\mu = \partial_\mu - i g_0 A_\mu \ , \tag{1.7}$$

where the vector field A_μ is a linear combination of the generators of the Lie-algebra of $SU(3)$, and g_0 is the bare strong coupling constant. $F_{\mu\nu}^a$ is the gluonic field strength tensor given by

$$F_{\mu\nu}^a = \partial_\mu A_\nu^a - \partial_\nu A_\mu^a + g_0 f^{abc} A_\mu^b A_\nu^c \ , \tag{1.8}$$

which explicitly shows that the non-abelian nature of $SU(3)$ leads to self-interactions of the gluonic fields A_μ^a. f^{abc} are the structure constants of $SU(3)$ satisfying the relation

$$[\lambda^a, \lambda^b] = 2i f^{abc} \lambda^c \ , \tag{1.9}$$

while the Gell-Mann matrices, λ^a, are the aforementioned generators of $\mathfrak{su}(3)$.

The Lagrangian of QCD only specifies the theory at the classical level. Quantization brings with it a number of complications that arise due to the fact that not all of the degrees of freedom in the gauge fields are physical. To restrict to solely the physical degrees of freedom, one must gauge fix (when using a perturbative expansion). However, in the non-abelian case, the gauge fixed path integral contains a functional determinant, which can be calculated by re-expressing it as a fermionic path integral. These fictitious fermions are known as *ghosts*. They are not physical, but rather a procedure introduced by Faddeev and Popov for maintaining a theory

with physical degrees of freedom [22]. Once the formulation of the Feynman rules has been achieved, one has a formal perturbative expansion. Of course, the regularization and renormalisation of the theory must be achieved, but once this is so, the perturbative definition of the quantum theory that corresponds to the classical Lagrangian is completed.

Due to renormalisation, the coupling constant of QCD is energy dependent. It grows as energy is decreased, rendering perturbation theory inapplicable for low energy QCD. It is clear that non-perturbative effects will play a major role at the energy scales of hadrons, and in order to probe such non-perturbative phenomena, we would like to solve the path integral of QCD directly. Unfortunately, no such solution exists. One alternate approach is to evaluate the path integral numerically within a discretised finite volume scheme, known as Lattice Field Theory.

1.2 Lattice QCD

The Standard Model contains many non-perturbative phenomena such as the Higgs mechanism or Confinement, and in order to study them from first principles it is essential to define the theory beyond a perturbative expansion. Lattice regularisation provides a setting in which this can be achieved. By replacing continuous space-time with a regular grid of points, one reduces the degrees of freedom of the path integral to a countably infinite set. Then, by reducing the infinite extent of the grid to that of a finite one, the path integral becomes finite dimensional over a lattice $\Lambda \subset \mathbb{Z}^4$,

$$\langle 0 \left| \mathcal{O}(\phi) \right| 0 \rangle = \int_A \mathcal{D}\phi \mathcal{O}(\phi) e^{iS(\phi)} \tag{1.10}$$

$$\mathcal{D}\phi(n) = \prod_n d\phi(n). \tag{1.11}$$

This regularisation should not be viewed as an approximation to the continuum theory, but rather that it provides a definition of a theory whose continuum limit may correspond to a useful physical theory. Of course, in order to take the continuum limit, one must renormalise the theory. To achieve this, one sends the lattice spacing to zero while simultaneously adjusting the bare parameters (in an appropriate way). Taking the continuum limit also removes the cut-off placed upon the theory by the discretisation; the shortest physical distance is the lattice spacing a which defines an ultraviolet momentum cut-off $1/a$.

The most common approach to extracting physical parameters from a lattice path integral is to use numerical methods such as Monte Carlo. Importance sampling is vital when trying to accumulate gauge field configurations via Monte Carlo, but it is not very compatible with the integrand in equation (1.10). Due to its imaginary nature, the exponential function oscillates wildly reducing the efficiency of the importance sampling technique and rendering the process impractical. Fortunately, this problem has a simple solution via a Wick rotation; a rotation from real time to imaginary time $t \to -it$ resulting in a switch from Minkowski to Euclidean space. The path integral then becomes

$$\langle 0 \,|\mathcal{O}(\phi)|\, 0 \rangle = \int_A \mathcal{D}\phi \mathcal{O}(\phi) e^{-S(\phi)} \,, \tag{1.12}$$

which is now suited to Monte Carlo importance sampling techniques.

1.2.1 The Gauge Sector

Requiring the invariance of the action (1.6) under local rotations of the colour indices of the quark fields enforces the introduction of gauge fields, A_μ, mathematically

known as connections. However, on the lattice, one does not use these algebra-valued fields directly, but instead describes gauge fields through the use of a gauge transporter

$$G(x,y) = \exp(i \int_C A \cdot ds), \tag{1.13}$$

where C is some curve connecting the two space-time points x and y. One then defines group-valued *link variables* as

$$U_\mu = \exp(iaA_\mu(n)), \tag{1.14}$$

which *link* the lattice point n to the point $n + \hat{\mu}$. These objects are now considered as the fundamental variables in the path integral. The change from algebra-valued to group-valued fields has important consequences. For instance, gauge fixing is no longer a requirement, since the measure for the gauge fields becomes the so-called *Haar measure*, which is automatically finite [27].

The preservation of gauge invariance is key when constructing a lattice action. Only two types of object achieve this on the lattice. The first is known as the holonomy, which is a parallel transporter around a non-trivial closed curve, and the other is a parallel transporter connecting one fermionic field to another. In order to construct the simplest lattice gauge action, it is sufficient to consider the simplest holonomy, known as the 'plaquette'

$$U_{\mu\nu} = U_\mu(n)U_\nu(n+\hat{\mu})U_\mu^\dagger(n+\hat{\mu}+\hat{\nu})U_\nu^\dagger(n+\hat{\nu}). \tag{1.15}$$

We can now define the *Wilson gauge action* as a sum over all plaquettes, with each plaquette only counted with one orientation

$$S_G = \frac{2}{g_0^2} \sum_{n \in \Lambda} \sum_{\mu < \nu} \Re\{\mathrm{Tr}\,[1 - U_{\mu\nu}(n)]\}. \tag{1.16}$$

An obvious way to check that this action is correctly describing the gauge sector is to perform the naive continuum limit. By using the Campbell-Baker-Hausdorff formula and Taylor expanding the gauge fields of the form $A_\mu(n + \hat{\nu})$, one can show that the plaquette reduces to

$$U_{\mu\nu} = \exp(ia^2 F_{\mu\nu}(n) + \mathcal{O}(a^3)). \tag{1.17}$$

Placing this form of the plaquette into the gauge action produces the result

$$S_G = \frac{2}{g_0^2} \sum_{n \in \Lambda} \sum_{\mu < \nu} \Re\{\mathrm{Tr}\,[1 - U_{\mu\nu}(n)]\} = \frac{a^4}{2g_0^2} \sum_{n \in \Lambda} \sum_{\mu\nu} \mathrm{Tr}\left[F_{\mu\nu}^2(n)\right] + \mathcal{O}(a^2), \tag{1.18}$$

which shows that the Wilson gauge action does indeed reduce to the pure gauge part of the action (1.6) in the naive continuum limit $a \to 0$.

1.2.2 The Fermionic Sector

When describing fermionic fields on the lattice, the simplest starting point is to discretise the fermionic part of the action (1.6). This amounts to placing spinor fields at the lattice points only, $n \in \Lambda$, and discretising the derivative appearing within the Dirac operator. Using a symmetric discretisation, the derivative becomes

$$\Delta_\mu = \frac{1}{2a} \left[\psi(n + \hat{\mu}) - \psi(n - \hat{\mu})\right], \tag{1.19}$$

yielding the following expression for the *free fermionic lattice action*

$$S_F^{free} = a^4 \sum_{n\in\Lambda} \bar{\psi}(n) \left[\sum_{\mu} \frac{\psi(n+\hat{\mu}) - \psi(n-\hat{\mu})}{2a} + m\psi(n) \right]. \tag{1.20}$$

In QCD, fermions live within an external gauge background. We incorporate this feature by the introduction of gauge fields into the fermionic action, which leads us to the so-called *naive fermion action*

$$S_F = a^4 \sum_{n\in\Lambda} \bar{\psi}(n) \left[\sum_{\mu} \frac{U_\mu(n)\psi(n+\hat{\mu}) - U_\mu^\dagger \psi(n-\hat{\mu})}{2a} + m\psi(n) \right]. \tag{1.21}$$

Since fermions are anti-commuting, we must use Grassmann numbers to describe them. They appear in the path integral as a bilinear form allowing us to use the *Matthews-Salam formula* [28]

$$\int d\eta_N d\bar{\eta}_N ... d\eta_1 d\bar{\eta}_1 \exp\left(\sum_{i,j=1}^{N} \bar{\eta}_i M_{ij} \eta_j \right) = \det[M], \tag{1.22}$$

and to write the fermionic generating functional as

$$W\left[\theta, \bar{\theta}\right] = \det[M] \exp\left(- \sum_{i,j=1}^{N} \bar{\theta}_i M_{ij}^{-1} \theta_j \right). \tag{1.23}$$

We can now use *Wick's Theorem* to calculate n-point functions of fermionic fields

$$\langle \eta_{i_1} \bar{\eta}_{j_1} ... \eta_{i_n} \bar{\eta}_{j_n} \rangle = (-1)^n \sum_{P(1,2,...,n)} \mathrm{sign}(P)\, M^{-1}_{i_1 j_{P_1}} M^{-1}_{i_2 j_{P_2}} ... M^{-1}_{i_n j_{P_n}}, \tag{1.24}$$

where the inverse of the Dirac operator is known as a *fermionic propagator*.

The Fourier transform of the lattice Dirac operator for a trivial background gauge field, $U_\mu(n) = 1$, can be written as

$$\tilde{M}(p) = \frac{i}{a}\sum_{\mu=1}^{4}\gamma_\mu \sin(ap_\mu) \; + \; m, \tag{1.25}$$

and the momentum space propagator as

$$\tilde{M}^{-1}(p) = \frac{m - ia^{-1}\sum_\mu \gamma_\mu \sin(ap_\mu)}{m^2 + a^{-2}\sum_\mu \sin^2(ap_\mu)}. \tag{1.26}$$

For massless fermions, taking the naive continuum limit leaves us with

$$\tilde{M}^{-1}(p) = \frac{-i\sum_\mu \gamma_\mu p_\mu}{p^2}, \tag{1.27}$$

which clearly has a pole at $p_\mu = (0,0,0,0)$, representing the fermion described by the continuum Dirac operator. However, the momentum space lattice propagator (1.26) has sixteen poles since it lives in the first Brillouin zone. We now see a fundamental problem when discretising fermions; any hermitian Dirac operator (in even dimensions) which leaves the discretised action local and translationally invariant will either produce extra unphysical poles or break chirality [29].

As a simple solution to the problem of these unphysical poles, Wilson proposed the addition of what is commonly known as the *Wilson term* to the naive fermion action:

$$W_\mu = ar\Delta_\mu^2 \; , \tag{1.28}$$

where $0 < r < 1$ is a bounded free parameter, and the lattice Laplacian is defined as

$$\Delta_\mu^2 = \sum_\mu a^{-2}\left(2\psi(n) - \psi(n+\hat{\mu}) - \psi(n-\hat{\mu})\right) \; . \tag{1.29}$$

To easily see that this removes the unphysical poles we can look at the Wilson momentum space Dirac operator

$$\tilde{M}_W(p) = \frac{i}{a}\sum_{\mu=1}^{4}\gamma_\mu \sin(ap_\mu) + m + a^{-1}\sum_{\mu}(1-\cos(ap_\mu)) \ . \tag{1.30}$$

It is clear that when $p_\mu = 0$ the Wilson term disappears, but when $p_\mu = \pi/a$ it gives an extra contribution of $2/a$. This removes the unphysical poles in the $a \to 0$ limit since it acts like a mass term, resulting in a mass of $m + 2/a$ for the unphysical poles. As expected, this remedy explicitly breaks chiral symmetry even in the chiral limit $m \to 0$.

In this work we use the Wilson formulation of fermions with a so-called *clover* term, as explained in sections 1.2.3 and 2.1. However, there are also many other formulations of lattice fermions, each with their own strengths and weaknesses. For example, the Kogut-Susskind fermions (or *staggered fermions*) [30] keep a remnant of chiral symmetry but still describe four *tastes* of fermion. Another example is that of *twisted mass fermions* [31–33]. Here an extra term, $i\mu\gamma_5\tau^3$, is added to the Dirac operator, where μ is a real parameter known as the *twisted mass*, in order for the determinant of the Dirac operator to be real and positive. The formulation is also automatically $O(a)$ improved for a so-called *maximal twist*.

For further details on the Wilson and alternative formulations of lattice fermions, see such books as [27, 34, 35].

1.2.3 Improvement

The Wilson fermion action suffers from the most severe form of systematic error, $\mathcal{O}(a)$ discretisation effects. Ideally, one would like to use an action that has $\mathcal{O}(a^n)$

lattice artefacts for some high number n (at least larger than 1) and perform simulations close to the continuum limit. Since it is computationally very expensive to simulate near the continuum limit, it would be extremely useful to have a scheme of systematically reducing discretisation effects. Such a scheme exists and is known as the *Symanzik improvement programme* [36, 37], but before we discuss this improvement scheme, let us briefly review a method of reducing the large renormalisation of gauge fields coming from their lattice definition. This is known as *tadpole improvement* [38].

Tadpole Improvement

Lattice operators are usually designed by mapping them onto analogous operators in the continuum, and for gauge fields, the mapping is based upon the expansion of the link variables

$$U_\mu(n) = 1 + iagA_\mu(n) - \frac{a^2g^2}{2}A_\mu^2(n) + ... \tag{1.31}$$

This expansion is valid for small values of a, but can be misleading since terms with a^2 or higher do not vanish as powers of a in the quantum theory; Lapage and Mackenzie [38] realised that the contraction of A_μ's with each other led to UV divergences that explicitly cancel the powers of a. These terms, which are contributions from *tadpole diagrams*, are then only suppressed by powers of g and become large. We thus lose our simple intuition between lattice and continuum operators due to the large renormalisation of lattice gauge variables.

Since these tadpoles come from the high momentum part of the loop integrals, and hence the high momentum part of the gauge field, they can be removed from the theory. Integrating out the UV components of the gauge field and by allowing a

tadpole factor u_0 to parametrise them, we can write

$$U_\mu(n) \approx u_0 \left(1 + iaA_\mu^{IR}\right). \tag{1.32}$$

There are many choices for u_0; a common one being that of the expectation value of the plaquette

$$u_0 = \left[\frac{1}{N}\langle Tr\left(U_{\mu\nu}\right)\rangle\right]^{\frac{1}{4}}. \tag{1.33}$$

This procedure suggests that in order to recover our intuition on the behaviour of lattice operators, we should rescale the link variable as

$$U_\mu(n) \to \frac{U_\mu(n)}{u_0}. \tag{1.34}$$

This divides out the UV contribution of the gauge field resulting in an object that behaves in a similar fashion to its continuum analogue. Of course, this procedure is fully non-perturbative since the tadpole factor is measured from a non-perturbative lattice calculation and not in perturbation theory.

In this work, we use tadpole improved gauge links when constructing our lattice actions as described in section 2.1.

Symanzik Improvement

Actions can be built from three types of operator. If the coupling constant of an operator increases with the scale of the system, it is known as *relevant*. If it decreases, it is known as *irrelevant*. If it varies, then the operator is called *marginal*. On the lattice, different actions that produce the same results in the continuum limit are said to be within the same *universality class*, that is, they describe the same physical

theory. In principle, these actions are constructed from the same set of relevant and marginal operators, and only differ in their irrelevant operators. However, at finite lattice spacing, results attained from different discretisations within the same universality class may differ from each other and from their continuum counterpart. Of course, the reduction of this effect is highly desirable.

The Symanzik improvement programme can aid against scaling violations by the addition of irrelevant operators of higher dimension to a given lattice action. Symanzik's scheme is most easily explained via example, so we will discuss on-shell $O(a)$ improvement of Wilson fermions, but first, let us explore the Symanzik improvement of the plaquette action.

The standard plaquette action (1.16) consists of the only four dimensional operator that respects gauge invariance; $Tr(F_{\mu\nu}^2)$. Implementing the Symanzik improvement scheme amounts to adding all the higher dimensional operators, that respect the symmetries of the original action, in order to form a new effective action:

$$S_{eff} = \int d^4x \left(L_0 + aL_1 + a^2L_2 + ...\right) \ , \tag{1.35}$$

where L_0 is the original Lagrangian. The terms L_n for $n > 0$ are irrelevant operators built from the fundamental fields such that they have dimension $4 + n$. Since only closed loops of gauge links form gauge invariant quantities, one can not add a dimension five operator to the plaquette action. Thus $L_1 = 0$ for any pure gauge action, meaning that they are automatically $O(a)$ improved.

At dimension six there are three distinct irrelevant operators that can be added to the action. These consist of the perimeter six-link loops; the rectangle (left), parallelogram (centre) and chair (right) shown in Figure 1.1. The addition of these three

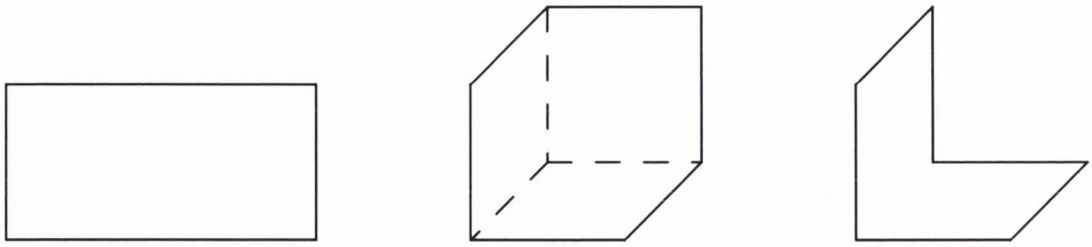

FIGURE 1.1: The perimeter six-link loops: (left) rectangle, (centre) parallelogram, (right) chair.

terms, multiplied with some *improvement coefficient*, to the action is the first step towards $O(a^2)$ improvement. The next step is to fix the improvement coefficients. An improvement condition is required to achieve this; for example, one can require that the static potential reproduce the continuum lowest order perturbative result up to terms of $O(a^4)$. At tree-level, Lüscher and Weisz [39] found that one can achieve $O(a^2)$ improvement by setting the coefficient of the rectangle $c_r = -1/12$ while setting the coefficient of the parallelogram and the chair to zero. In this work, we use this $O(a^2)$ improved formulation to describe the gauge sector as described in section 2.1.

The procedure for improving fermionic actions follows the same mandate as for gauge actions; one must write all of the irrelevant operators that have dimension greater than four obeying the symmetries of the original action, and add them to that action. Here we will discuss on-shell $O(a)$ improvement, so it is sufficient to

write all the operators of dimension five:

$$\mathcal{O}_1(x) = \bar{\psi}(x)\sigma_{\mu\nu}F_{\mu\nu}(x)\psi(x) \tag{1.36}$$

$$\mathcal{O}_2(x) = \bar{\psi}(x)\overrightarrow{D}_\mu(x)\overrightarrow{D}_\mu(x)\psi + \bar{\psi}(x)\overleftarrow{D}_\mu(x)\overleftarrow{D}_\mu(x)\psi(x) \tag{1.37}$$

$$\mathcal{O}_3(x) = m\ \mathrm{Tr}\left[F_{\mu\nu}(x)F_{\mu\nu}(x)\right] \tag{1.38}$$

$$\mathcal{O}_4(x) = m\left(\bar{\psi}(x)\gamma_\mu\overrightarrow{D}_\mu(x)\psi + \bar{\psi}(x)\gamma_\mu\overleftarrow{D}_\mu(x)\psi(x)\right) \tag{1.39}$$

$$\mathcal{O}_5(x) = m^2\bar{\psi}(x)\psi(x)\ . \tag{1.40}$$

where $\sigma_{\mu\nu} \equiv [\gamma_\mu, \gamma_\nu]/2$. Using the field equation, $(\gamma_\mu D_\mu + m)\,\psi = 0$, we get the following two relations:

$$\mathcal{O}_1(x) - \mathcal{O}_2(x) + 2\mathcal{O}_5(x) = 0 \tag{1.41}$$

$$\mathcal{O}_4(x) + 2\mathcal{O}_5(x) = 0\ , \tag{1.42}$$

Using these two equations, we can eliminate $\mathcal{O}_2(x)$ and $\mathcal{O}_4(x)$ from the set of correction operators. Noticing that $\mathcal{O}_3(x)$ and $\mathcal{O}_5(x)$ are already present within the original action allows us to eliminate them from the set by redefining the bare parameters m and g. This leaves only $\mathcal{O}_1(x)$ in the set of correction operators. Hence, to $O(a)$ improve the Wilson fermionic action on-shell, it is sufficient to add the so-called *clover term* along with its improvement coefficient c_{sw} [40]:

$$C = c_{sw}\frac{a^5}{2}\sum_n\sum_{\mu<\nu}\bar{\psi}(n)\sigma_{\mu\nu}F_{\mu\nu}(n)\psi(n)\ . \tag{1.43}$$

$F_{\mu\nu}(n)$ is a discretisation of the field strength tensor given by the non-unique expression:

$$F_{\mu\nu}(n) = \frac{-i}{8a^2}\left(Q_{\mu\nu}(n) - Q_{\nu\mu}(n)\right)\ . \tag{1.44}$$

$Q_{\mu\nu}$ is a sum of four plaquettes as shown in Figure 1.2. Physically, the lattice has

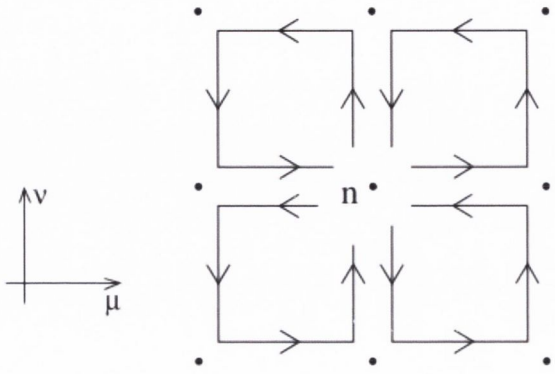

FIGURE 1.2: A pictorial representation of the *clover* sum of plaquettes $Q_{\mu\nu}$.

assigned an anomalous chromomagnetic moment of $O(a)$ to the quarks, and it is the addition of this Pauli like clover term that corrects for it [41].

The next step in the improvement scheme is to determine the appropriate value of the improvement coefficient c_{sw}; it needs to weight the correction term just enough to cancel the $O(a)$ artefacts. Perturbation theory can be used to calculate c_{sw} [42], but of course this requires one to work in a regime where the coupling is small which may not always be useful for calculations in QCD. However, a non-perturbative scheme for calculating c_{sw} (and c_A, the axial current improvement coefficient) using chiral symmetry, that is, the *partially conserved axial current* (PCAC) relation in the continuum limit has been suggested by the *Alpha collaboration* [43].

Adding the clover term and appropriately determining c_{sw} is sufficient for $O(a)$ improvement of on-shell quantities such as hadron masses, but full $O(a)$ improvement of a correlation function also requires the improvement of its interpolators. For details on improving interpolators see [27, 35, 43].

In this work, we add the on-shell $O(a)$ improvement term, $C_{\mu\nu}$, to our Wilson formulation of fermions as described in section 2.1.

This concludes our brief introduction to Lattice QCD, but before jumping directly into the details of our calculation, we take a brief moment to set the experimental scene that motivates our study of the charm sector.

1.3 Experimental Status of the Charm Sector

The charm quark was proposed by Glashow and Bjorken in the mid 1960's [44], but there was little or no evidence for its existence. It became a theoretical requirement in 1970 when the Glashow-Illopoulos-Maiani mechanism (GIM mechanism) required the existence of a heavy fourth quark in order to explain why flavour changing neutral currents are suppressed [45]. These predictions were vindicated in 1974 with the observation of the J/ψ meson [46, 47].

For the following thirty years, charm meson spectroscopy had been successfully described by a relatively simple picture; a bound state of a quark and anti-quark whose spins are coupled together to form a total spin S, which is then coupled to an orbital angular momentum L in order to create a state of total angular momentum J. In this phenomenological model, the states follow a $n^{2S+1}L_J$ pattern. If the meson is an eigenstate of charge conjugation, i.e. it is its own anti-particle, then some J^{PC} (where P and C are the parity and charge conjugation quantum numbers respectively) combinations are absent from this simplistic set up. Such states are termed *exotic*.

Currently, the spectra of open-charm mesons contains a number of well established states [48]. There are eight D mesons, which are *charm-light* combinations of isospin $I = 1/2$, and six D_s mesons, which are *charm-strange* combinations of non-zero strangeness and zero isospin. In both sectors there are a number of tentative states

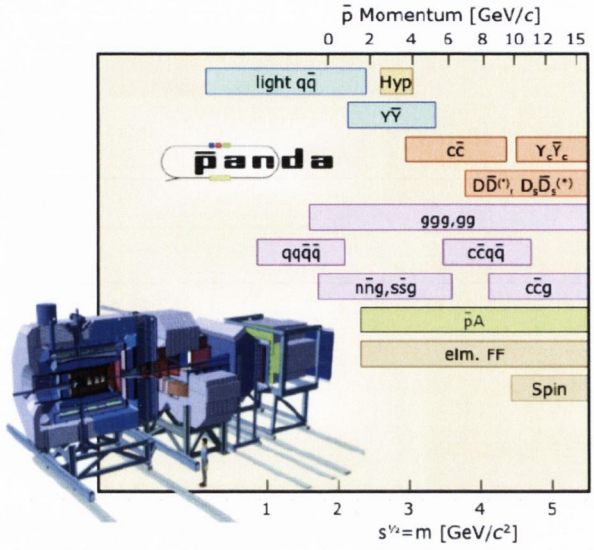

FIGURE 1.3: The energy range of the planned PANDA experiment and some of the physics it will explore.

omitted from the Particle Data Group summary tables, suggesting that their existence needs further confirmation. Many of the well established states can be described by the pattern expected from quark potential models [49, 50]. However, a subset of these states as well as additional states requiring experimental confirmation, do not fit the predictions and are thus unexplained. For example, the masses and widths of the enigmatic $D^*_{s0}(2317)^{\pm}$ and $D_{s1}(2460)^{\pm}$ particles are significantly lighter and narrower than in quark models [49, 50]. Since the discovery of these resonances at BABAR [51] and CLEO [52] respectively, there has been much debate about their nature. Suggestions such as tetra-quarks (two valence quarks and two valence anti-quarks), molecular mesons and hybrid mesons (in which the gluonic field is excited) have been put forward, but the situation is far from being resolved.

The spectrum of hidden charm mesons (charmonia) has received much experimental interest since the discovery of the J/ψ. There are eighteen well established states

along with a number requiring further experimental confirmation [48]. Below the open-charm threshold, the spectrum is well understood in terms of quark models, but the recent observation of many unexpected resonances close to, or above this threshold has caught the interest of both the theoretical and experimental community. For example, the $X(3872)$ resonance [53] is now well established but its interpretation is still unclear, although recent experiments at the LHCb strongly suggest that it has $J^{PC} = 1^{++}$. With this assignment, it could still be interpreted as the $c\bar{c}$ bound state $\chi_{c1}(2^3P_1)$, but this is unlikely due to its mass; the resonance appears far from where the $\chi_{c1}(2^3P_1)$ is expected and an exotic explanation such as a $D\bar{D}^*$ molecule or tetra-quark particle seems imminent. The $X(4430)^{\pm}$ observed in $B \to K\pi$ decays at BELLE is another exotic candidate [54]. Due to it being electrically charged, it can not be a standard $c\bar{c}$ meson. Instead, it is thought that this resonance is of a tetra-quark nature and, like many of the current mysteries surrounding the charm sector, will require further investigation.

Experimental searches continue at BESIII and at the LHC, while in Darmstadt the construction of a proton anti-proton collider at GSI/FAIR has begun. This experiment, known as PANDA, will conduct extensive searches in both the open and hidden charm sectors as well as looking for exotic states. A summary of the experiments energy range and some of the physics it hopes to explore is shown in Figure 1.3.

For a recent review of hadron spectroscopy see [55].

Chapter 2

Lattice Details

The main focus of this study is to determine the spectrum of hidden and open-charm states, including excitations and any states with an intrinsic gluonic component. Throughout this thesis, we will refer to eigenstates of the lattice Hamiltonian, E, as *spectroscopic states*, which are computed via two-point correlation functions which fall off in proportion to e^{-Et}. Since the open-charm spectra lie around and above 2 GeV, and the charmonium spectrum lies above 3 GeV, it is clear that the corresponding correlation functions will fall off rapidly, even at modest times. Furthermore, correlation functions built from interpolators that excite high-lying states will suffer from increasing statistical variance.

One way to ameliorate these problems is to use an anisotropic lattice where the temporal discretisation is finer than the spatial one. Of course it would be more beneficial to have both the temporal and spatial directions very fine, but the computational cost would rise dramatically. In order to keep the computational cost down, we use a relatively coarse spatial discretisation.

Previously, the mass of the charm quark was problematic; it was too light for non-relativistic actions to be valid, but large enough such that $am_c \ll 1$ was difficult to achieve. Recently, a number of successful approaches for simulating the charm quark were developed, such as the Fermi-lab [56] and HISQ [57] actions. In this work, we use a discretisation such that the anisotropy, $\xi = a_s/a_t \sim 3.5$. This fine temporal discretisation ensures that we carry out calculations with $a_t m_c \ll 1$, allowing us to use the standard relativistic formulation of fermion actions for the charm quark. It is also encouraging to note that on our ensembles $a_s m_c < 1$.

2.1 Dynamical $2+1$ Anisotropic Lattices

In this study we use dynamical $2+1$ anisotropic ensembles generated by the Hadron Spectrum Collaboration [58, 59]. On these lattices, the gauge sector is described by a Symanzik-improved (see section 1.2.3) anisotropic action with tree level tadpole-improved (see section 1.2.3) coefficients

$$S_G = \frac{\beta}{N_c \xi_0} \left\{ \sum_{\substack{x \\ s>s'}} \left[\frac{5}{3u_s^4} P_{ss'} - \frac{1}{12u_s^6} R_{ss'} \right] + \sum_{x,s} \left[\frac{4}{3u_s^2 u_t^2} P_{st} - \frac{1}{12u_s^4 u_t^2} R_{st} \right] \right\}, \tag{2.1}$$

where P is the plaquette and R is the 2×1 rectangular Wilson loop. N_c is the number of colours and $\beta = 2N_c/g^2$. The bare anisotropy is given by the parameter ξ_0, and u_s and u_t are the spatial and temporal tadpole factors dividing the spatial and temporal gauge links, respectively. The leading discretisation errors associated with this action are $O(a_s^4, a_t^2, g^2 a_s^2)$.

Volume	N_{cfgs}	N_{tsrcs}	N_{vecs}
$16^3 \times 128$	96	128	64
$24^3 \times 128$	552	32	162

TABLE 2.1: The gauge field ensembles used in the calculation of the charmonium spectrum. N_{cfgs} and N_{tsrcs} are respectively the number of gauge field configurations and time-sources per configuration used; N_{vecs} refers to the number of eigenvectors used in the distillation method

The fermionic sector is described via an anisotropic clover action, given by

$$S_F = a_s^3 a_t \sum_x \bar{\psi}(x) Q \psi(x) \ , \tag{2.2}$$

where

$$Q \ = \ \left[m_0 + \nu_t W_t + \nu_s W_s \ - \ \frac{a_s}{2} \left(c_t \sigma_{st} F^{st} \ + \ \sum_{s<s'} c_s \sigma_{ss'} F^{ss'} \right) \right] \ . \tag{2.3}$$

Here $\sigma_{\mu\nu} \ = \ \frac{1}{2} [\gamma_\mu, \gamma_\nu]$, and the Wilson term is given by

$$W_\mu \ = \ \nabla_\mu \ - \ \frac{a_\mu}{2} \gamma_\mu \Delta_\mu \ . \tag{2.4}$$

ν is the ratio of the bare fermion anisotropy to the bare gauge anisotropy. The spatial and temporal clover coefficients are given by

$$c_s \ = \ \frac{\nu}{u_s^3} \tag{2.5}$$

$$c_t \ = \ \frac{1}{2} \left(\nu + \frac{1}{\xi} \right) \frac{1}{u_t u_s^2} \ , \tag{2.6}$$

where the fraction $a_t/a_s = 1/\xi$ is set to the desired renormalised gauge anisotropy.

On these ensembles the gauge links in the fermion action are three-dimensionally stout smeared. The smearing parameters, as discussed in section 3.1 , are $\rho = 0.22$

Volume	N_{cfgs}	N_{tsrcs}	N_{vecs}
$16^3 \times 128$	96	128	64
$24^3 \times 128$	553	16	162

TABLE 2.2: The gauge field ensembles used in the calculation of the open-charm spectra. N_{cfgs} and N_{tsrcs} are respectively the number of gauge field configurations and time-sources per configuration used; N_{vecs} refers to the number of eigenvectors used in the distillation method

and $n_\rho = 2$. In [58], the authors determined the gauge anisotropy from the static quark potential using the ratio of Wilson loops

$$R_{ss}(x,y) = \frac{W_{ss}(x,y)}{W_{ss}(x+1,y)} \to e^{-a_2 V_s(y a_s)} , \tag{2.7}$$

$$R_{st}(x,y) = \frac{W_{st}(x,t)}{W_{st}(x+1,t)} \to e^{-a_s V_s(t a_t)} , \tag{2.8}$$

while the fermionic anisotropy was determined via the continuum relativistic dispersion relation

$$E^2(\vec{p}) = m^2 + \frac{\vec{p}^2}{\xi_f^2} . \tag{2.9}$$

On these ensembles $\beta = 1.5$, and the final tuned values for the bare gauge and fermion anisotropies are $\gamma_g = 4.3$ and $\gamma_f = 3.4$. The corresponding values for the spatial and temporal clover coefficients are $c_s = 1.589$ and $c_t = 0.903$.

In lattice calculations, all quantities are computed in terms of the lattice spacing and, in order to make contact with experiment, one must quote results in physical units. Therefore, a scale setting must be introduced. We set the scale by considering the ratio of the Ω-baryon mass measured on these ensembles, $a_t m_\Omega = 0.2951(22)$ to the experimental mass, $M_\Omega = 1672.45(29)$ MeV [48]. From this scale setting, we find a spatial lattice spacing of $a_s = 0.122(1)$ fm and a temporal lattice spacing approximately 3.5 times smaller, $a_t^{-1} = 5.67(4)$ GeV. On these ensembles, the pion

Volume	N_{cfgs}	N_{tsrcs}	N_{vecs}
$20^3 \times 128$	603	3	128

TABLE 2.3: The gauge field ensembles used in the calculation of $D\pi$ scattering. N_{cfgs} and N_{tsrcs} are respectively the number of gauge field configurations and time-sources per configuration used; N_{vecs} refers to the number of eigenvectors used in the distillation method

mass is $M_\pi \sim 391$ MeV. The spectroscopic calculations carried out in this study are on two-volumes $(L/a_s)^3 \times (T/a_t) = 16^3 \times 128$ and $24^3 \times 128$. The study of $D\pi$ scattering was performed on a third volume $20^3 \times 128$. The ensembles used in the calculation of the charmonium spectrum are summarised in Table 2.1, the open-charm spectra in Table 2.2 and for $D\pi$ scattering in Table 2.3. It is worth noting that the configurations sampled on our 16^3 ensembles are separated by twenty trajectories (after thermalisation) within the Monte Carlo Markov chain. Our 20^3 and 24^3 configurations are again separated by twenty trajectories from four different Markov chains. A separation of twenty trajectories was determined via a *binning* procedure in order to render two consecutively sampled configurations effectively uncorrelated. To calculate the statistical uncertainty in all of our results, we use the single elimination jackknife method.

2.2 The Charm Quark

We employ the same relativistic action for the charm quark as was used for the light and strange quarks. On anisotropic ensembles, the weights of spatial and temporal derivative terms must be determined so that observables take their experimental value when calculated in a simulation. As shown in [60], this is important in dynamical simulations to ensure a correct continuum limit. On our ensembles the target

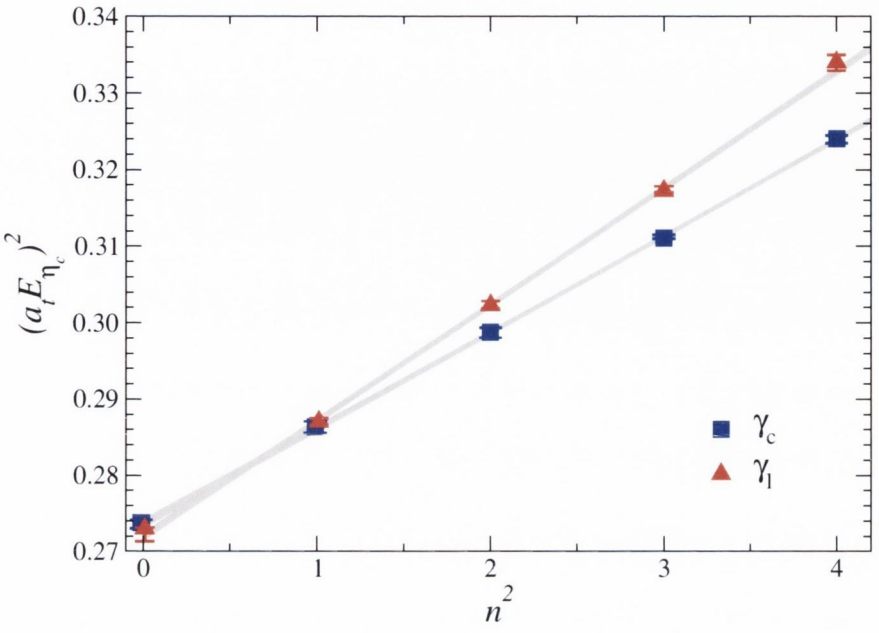

FIGURE 2.1: Squared energies of the η_c meson as a function of momentum, n^2, calculated on our $16^3 \times 128$ volume, for two choices of the bare fermionic anisotropy γ_f as described in Table 2.4. γ_l is the parameter used in the light quark action and γ_c is obtained by ensuring the correct relativistic dispersion relation for the η_c meson.

ratio of spatial to temporal scales is $\xi = 3.5$. In the light meson sector, this was determined via the pion dispersion relation, leading to a value of $\xi_\pi = 3.444(6)$ [61].

To determine the anisotropy, ξ, in the charm sector, we study the dispersion relation of the η_c meson. This will also allow us to set bare mass of the charm quark. The relativistic dispersion relation for a meson A, in the continuum, can be written

$$(a_t E_A)^2 = (a_t m_A)^2 + \left(\frac{1}{\xi_A}\right)^2 (a_s p)^2 \,, \tag{2.10}$$

where the momentum is quantised due to the periodic boundary conditions of the cubic volume

$$a_s \vec{p} \;=\; \frac{2\pi}{L}(n_x, n_y, n_z) \,, \tag{2.11}$$

Sector	β	u_s	u_t	γ_g	γ_f	ν	m_c	c_s	c_t
light	1.5	0.9267	1	4.3	3.4	1.265	0.087	1.589	0.902
charm	1.5	0.9267	1	4.3	3.98	1.078	0.092	1.345	0.793

TABLE 2.4: The bare parameters used in the determination of the η_c dispersion relation. The light parameters are those previously determined in the light sector [58], but with the bare mass scaled up to give an approximately correct η_c mass. The charm parameters are those determined by ensuring that the η_c meson has the correct dispersion relation with an anisotropy $\xi_{\eta_c} = 3.50(2)$.

with $n_i \in \{0, 1, \ldots, L/a_s - 1\}$.

Figure 2.1 shows squared energies as a function of the momentum, n^2, for the η_c meson, calculated using the two parameter sets described in Table 2.4. The red triangular symbols show the dispersion relation when the bare parameter γ_f is the same as used in the light quark action (see Table 2.4). In this case, the bare charm quark mass is chosen such that the η_c meson takes (approximately) its experimental value. For this set of bare parameters, the physical anisotropy, $\xi_{\eta_c} = 3.18(2)$. Clearly, since our target value is 3.5, we need to correct for this discrepancy.

The blue squares in Figure 2.1 show the dispersion relation for the η_c meson calculated using the bare parameter set 'charm' in Table 2.4. In order to correct for the previous discrepancy, the fermion anisotropy is increased to $\gamma_f = \gamma_c = 3.98$. These parameters result in a physical anisotropy $\xi_{\eta_c} = 3.50(2)$, and a mass of 2965(1) MeV for the η_c meson, which is within one percent of its experimental value, 2983(1) MeV [48]. It is encouraging to note that our data agrees with the relativistic dispersion relation up to momentum of at least $\vec{n} = (2, 0, 0)$, with both fits in Figure 2.1 having $\chi^2/N_{\text{dof}} \sim 1$. As a check of the consistency of the physical anisotropy in the charmonium sector, the dispersion relation of the J/ψ meson was calculated. The value obtained, via a fit to this dispersion relation, of the physical anisotropy, deviated by less than one percent from the value obtained from the η_c dispersion relation.

2.3 Open-Charm Dispersion Relations

To understand the nature of charmonium and charmed resonances above the open-charm threshold, we must have full control of heavy-light mesons since scattering calculations involving these states will be required. As discussed in section 8.1, to determine properties of resonances on the lattice requires the calculation of the full spectrum of energy eigenstates, including those composed of more than one meson. For these calculations to be reliable, all relevant mesons must have relativistic dispersion relations with consistent physical anisotropies.

When simulating heavy quarks on the lattice, extra complications can arise due to the large mass scale. However, for mesons moving with modest momenta, the heavy quark four-momentum will predominantly be aligned with the temporal direction, and on our anisotropic ensembles, the fine temporal discretisation may reduce the artefacts associated with heavy quarks. It is well known that when am_Q is of $O(1)$, the dispersion relation of the corresponding meson will appear non-relativistic forcing the kinetic and rest masses to differ [56].

One way to test if the anisotropic lattice has controlled the size of these artefacts for the charm quark is to determine the dispersion relation of a number of mesons in the charm-light and charm-strange spectra; if there is a problem with large artefacts coming from the heavy quark, some or all of the dispersion relations may appear non-relativistic, or the physical anisotropies measured from the dispersion relations may significantly differ from each other or those calculated for the η_c meson or pion.

We calculate dispersion relations for a range of charm-light and charm-strange mesons. We use two sets of interpolators to achieve this. For mesons at rest, we use the J_z-basis interpolators as described in section 3.3, while for mesons with non-zero momentum, we use the helicity-basis interpolators (up to two derivatives)

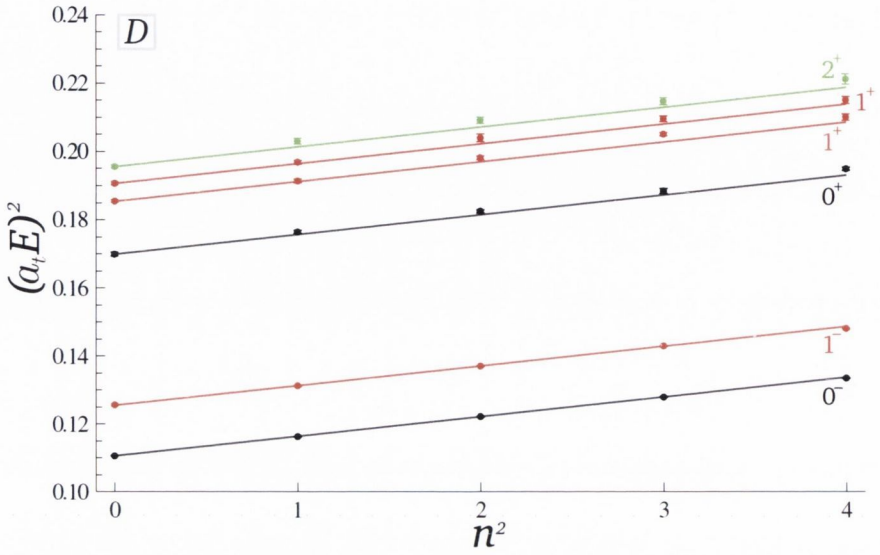

FIGURE 2.2: Squared energies as a function of n^2 for the lightest S and P-wave states in the charm-light spectrum. The points correspond to calculated squared energies and the error bars correspond to statistical uncertainties. Points with no visible error bar have statistical error smaller than the size of point. The lines are dispersion relations of the form (2.10), with m fixed to the rest mass of the D meson and the anisotropy fixed to $\xi_D = 3.454$ as described in the text.

as described in section 3.3.1. Shown in Figure 2.2 are squared energies as a function of n^2 for the six lowest lying states in the charm-light spectrum. Figure 2.3 also shows squared energies as a function of n^2, but this time for the six lowest lying states in the charm-strange spectrum. The points correspond to calculated squared energies with the statistical uncertainty shown by the error bars. If no error bar is visible for a given point, it means the statistical error is smaller in size than the corresponding point. In both the charm-light and charm-strange sectors, we calculate the anisotropy of the lowest lying states, ξ_D and ξ_{D_s}, by fitting the energies of the corresponding 0^- meson to equation (2.10). This gives good fits yielding $\xi_D = 3.454(6)$ and $\xi_{D_s} = 3.453(3)$. The lines in Figures 2.2 and 2.3 are dispersion relations of the form (2.10) with m fixed to the rest energy of the relevant meson, and ξ fixed to our measured values of $\xi_D = 3.454(6)$ and $\xi_{D_s} = 3.453(3)$ as appropriate.

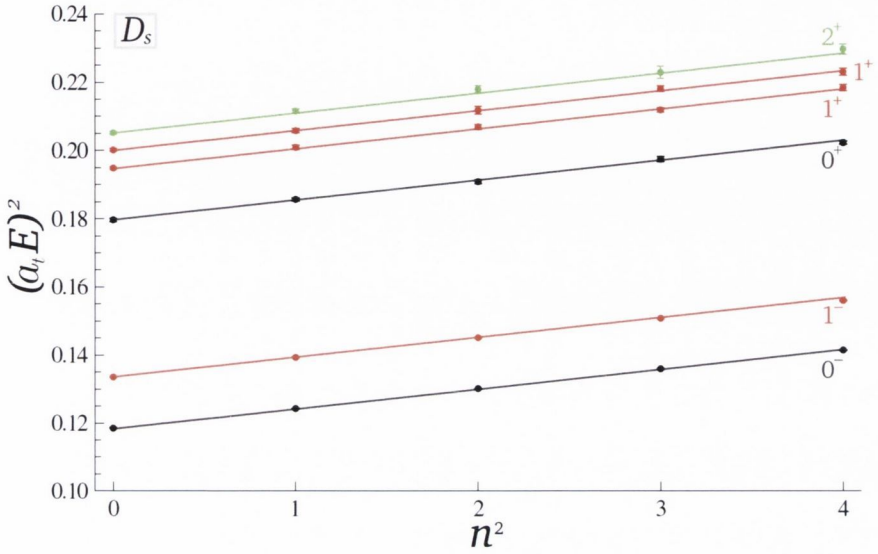

FIGURE 2.3: Squared energies as a function of n^2 for the lightest S and P-wave states in the charm-strange spectrum. The points correspond to calculated squared energies and the error bars correspond to statistical uncertainties. Points with no visible error bar have statistical error smaller than the size of point. The lines are dispersion relations of the form (2.10), with m fixed to the rest mass of the D_s meson and the anisotropy fixed to $\xi_{D_s} = 3.453$ as described in the text.

The first point of note is that all of the states in Figures 2.2 and 2.3 follow a relativistic dispersion relation, at least up to momentum $n^2 = 4$. The second point worth noting is that the physical anisotropies attained from the ground state in both the charm-light and charm-strange sectors agree with the the other low lying states in their corresponding spectra, as well as those obtained from the pion and η_c dispersion relations, suggesting that the charm quark mass artefacts are under control.

Chapter 3

Spectroscopy on the Lattice

In lattice field theory, spectroscopic information is obtained from the two-point correlation function

$$C_{ij}(t) \;=\; \frac{1}{Z}\,\mathrm{Tr}\,\left[\mathbf{T}\mathcal{O}_i(t)\mathcal{O}_j^{\dagger}(0)\;e^{-\beta H}\right]\,, \tag{3.1}$$

where $\mathbf{T}$ is the time-ordering operator and $Z = \mathrm{Tr}[e^{-\beta H}]$. $\mathcal{O}_i(t)$ are known as interpolating operators (interpolators), and may consist of gauge invariant quantities, such as the plaquette or colour-singlet combinations of quarks and anti-quarks. Applying the time translation operator e^{-tH} to the interpolators, and inserting a complete set of eigenstates of the Hamiltonian yields

$$C_{ij}(t) \;=\; \frac{1}{Z}\sum_{n,m}\,\langle m|\mathcal{O}_i|n\rangle\;\langle n|\mathcal{O}_j^{\dagger}|m\rangle\;e^{-E_n t}\;e^{-E_m(\beta-t)}\,, \tag{3.2}$$

where the discreteness of the spectrum is due to the finite volume, and the temperature $T = 1/\beta$. Taking the zero-temperature limit, that is, where t and $(\beta - t)$ are large, the correlation function will be dominated by the lowest energy states that

have the same quantum numbers as $\mathcal{O}_i$ (where we have set $i = j$ for convenience)

$$\begin{aligned} C_{ii}(t) &= |\langle 0|\mathcal{O}_i|0\rangle|^2 + |\langle 0|\mathcal{O}_i|1\rangle|^2 \left[e^{-E_1 t} + e^{-E_1(\beta - t)}\right] \\ &+ \mathcal{O}\left(e^{-(E_2 - E_1)t}\right) + \mathcal{O}\left(e^{-(E_2 - E_1)(\beta - t)}\right) . \end{aligned} \tag{3.3}$$

The term $|\langle 0|O_i|0\rangle|^2$ corresponds to the *vacuum-disconnected* part of the correlator. This term will vanish in a gauge average unless the interpolator, $\mathcal{O}_i$, has the quantum numbers of the vacuum ($J^{PC} = 0^{++}$). If the interpolator has a small overlap with the lightest state, E_1, then the correction terms in (3.3) will have relatively large coefficients, and a reliable value for the lightest state energy can only be extracted when t is very large. If $0 \ll t \ll \beta$, then the *vacuum-connected* part of the correlator has the asymptotic form

$$C_{ii}(t) \sim |\langle 0|\mathcal{O}_i|1\rangle|^2 \, e^{-E_1 t} . \tag{3.4}$$

One can then define the so-called *effective mass*

$$m_{eff}(t) = \ln\left[\frac{C_{ii}(t)}{C_{ii}(t+1)}\right] , \tag{3.5}$$

which will plateau at the energy of the lightest state E_1 created by the interpolator $\mathcal{O}_i$.

Since we are interested in calculating spectroscopic quantities of charmonium, charm-light and charm-strange combinations, we must *choose* interpolators that create mesonic states from the vacuum. The simplest of which is the set of local interpolators given by

$$\mathcal{O}^{\dagger}_{ff'}(n) = \bar{\psi}_f(n) \, \Gamma_i \, \psi_{f'}(n) , \tag{3.6}$$

where we have suppressed spin and colour indices for clarity. Here, $n \in \Lambda$ is the

State	$J^{P(C)}$	Γ	Naming Scheme
Scalar	$0^{+(+)}$	$\mathbf{1}$	a_0
Scalar	$0^{+(+)}$	γ_0	b_0
Pseudo-Scalar	$0^{-(+)}$	γ_5	π
Pseudo-Scalar	$0^{-(+)}$	$\gamma_0\gamma_5$	π_2
Vector	$1^{-(-)}$	γ_i	ρ
Vector	$1^{-(-)}$	$\gamma_0\gamma_i$	ρ_2
Axial-Vector	$1^{+(+)}$	$\gamma_5\gamma_i$	a_1
Tensor	$1^{+(-)}$	$\gamma_i\gamma_j$	b_1

TABLE 3.1: Gamma matrix naming scheme and their corresponding quantum numbers. The charge conjugation quantum number, C, is only defined for flavour singlet interpolators.

point of creation of the meson, and f, f' label the quark flavour. Γ_i is one of the combinations of gamma matrices shown in Table 3.1.

In general, a two-point function composed of interpolators $\mathcal{O}^\dagger_{ff'}(n)$ and $\mathcal{O}_{ff'}(m)$ can be written as

$$\begin{aligned}\langle \mathcal{O}_{ff'}(n)\, \mathcal{O}^\dagger_{ff'}(m) \rangle \;=\; &- \;\mathrm{Tr}\,\left[\,\Gamma\, M^{-1}_{ff}(n|m)\,\Gamma\, M^{-1}_{f'f'}(m|n)\,\right] \\ &+ \;\mathrm{Tr}\,\left[\,\Gamma\, M^{-1}_{ff'}(n|n)\,\right]\,\left[\,\Gamma\, M^{-1}_{ff'}(m|m)\,\right]\,, \end{aligned} \tag{3.7}$$

using *Wick contractions*. Both terms in this equation have a simple interpretation. In the first term, the propagator $M^{-1}_{ff}(n|m)$ propagates an f quark from space-time point m to n, while $M^{-1}_{f'f'}(m|n)$ propagates an f' quark in the opposite direction. This term is referred to as *connected*, and is shown on the left of Figure 3.1. In the second term, the propagators are of the form $M^{-1}_{ff'}(n|n)$ which is interpreted as propagation back to the same space-time point. This term is referred to as *disconnected*, and is shown on the right of Figure 3.1. Clearly this term is zero when $f \neq f'$, that is, it only contributes for the special case of flavour singlet mesons.

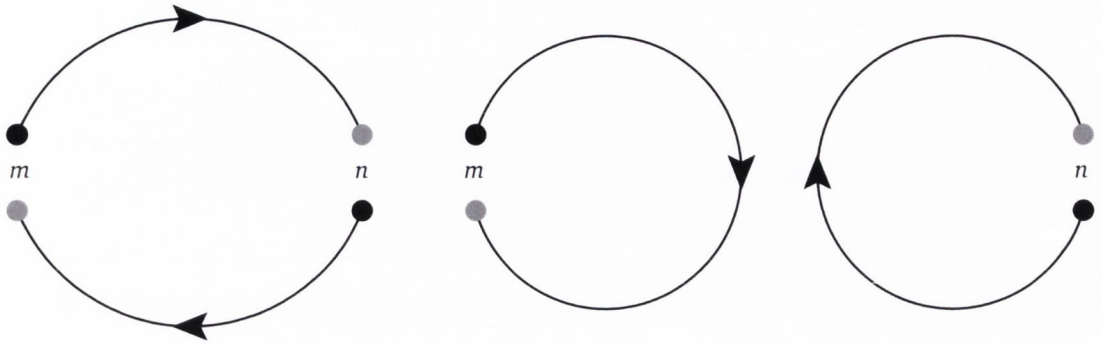

FIGURE 3.1: A graphical representation of a mesonic correlator, separated into its connected (left) and disconnected (right) parts. The propagation begins and ends at space-time points m and n as shown.

A useful constraint to place upon an interpolator is that it should create a state of definite momentum. This can be achieved via

$$\tilde{\mathcal{O}}_{ff'}(\vec{p},\ n_t) \ = \ \frac{1}{\sqrt{|\Lambda_3|}} \sum_{\vec{n}\in\Lambda_3} e^{-ia\vec{n}\vec{p}}\ \mathcal{O}(\vec{n},\ n_t)\ , \tag{3.8}$$

where the momenta, $\vec{p}$, are quantised via $\vec{p} = 2\pi\vec{k}/L$. Here L is the spatial extent of the lattice and $\vec{k} \in \mathbb{Z}^3$. This interpolator is projected onto a definite momentum and is located on a single time-slice n_t. It is thus sufficient to project only one of the two interpolators in a two-point function (usually the annihilation interpolator) to the desired momentum in order to achieve a hadronic state of definite momentum, but, it is important to note that this is only approximate for a finite number of configurations. A correlation function containing a momentum projected interpolator at the sink will fall off at large times $\sim e^{-atE(\vec{p})}$, where the energy of the lightest state $E(\vec{p})$ is related to the mass of the hadron, m, by

$$E(\vec{p}) \ = \ \sqrt{m^2 \ + \ \vec{p}^2} \ + \ O(a\vec{p})\ . \tag{3.9}$$

We have now seen how to extract spectroscopic quantities on the lattice. However, using only the techniques described in this section will lead to a limited spectrum of states, and for a given amount of configurations, results that are relatively noisy compared to more modern methods. In the remaining sections of this chapter, we discuss the recipe used by the Hadron Spectrum Collaboration for extracting extensive spectra [62], and apply it to the Hidden and open-charm sectors. We begin with discussions of what is known as *smearing*; in the following section we explain our smearing in the gauge sector, and then in section 3.2 we explain our smearing of the quark fields, and how it leads to a convenient way of constructing correlation functions.

3.1 Gauge Field Smearing

We know now that hadron masses are extracted from the large time behaviour of Euclidean correlation functions. However, one major problem is that the signal-to-noise ratio degrades rapidly at these large times. One can considerably improve the signal by smoothing or smearing the gauge fields; interpolators constructed on or from these smeared gauge fields have dramatically reduced mixing with the UV modes of the theory, and consequently, have greater overlap onto the low-lying states of interest, allowing the hadron masses to be extracted at smaller times. The use of such interpolators has been shown to benefit determinations of the glueball spectrum [63], the torelon spectrum [64] and the static potential [65]. Smearing has also played an important role in the construction of improved actions, for example, the use of *fat links* in a staggered quark action is shown to decrease flavour symmetry breaking [66], while smearing can be used to construct hyper-cubic fermion actions with improved rotational invariance [67].

Most smearing procedures consist of averaging products of links along some short path connecting the end points of a given link. The simplest such construction is known as *APE smearing* [68]. Here, every link is replaced by itself plus a weight ρ times a sum of its four neighbouring spatial staples, projected back into $SU(3)$. This projection is usually performed as follows: given a 3×3 matrix V, its projection U into $SU(3)$ is taken to be the matrix $U \in SU(3)$ that maximises the expression $\Re e\mathrm{Tr}(UV^\dagger)$. There are two weak points of this construction. Firstly, the projection step is a rather arbitrary way of remaining within $SU(3)$. Secondly, the lack of differentiability associated with the projection step inhibits its use in molecular dynamics updating schemes, such as the Hybrid Monte Carlo, that require information on the response of the action to a small change in one of the link variables.

A method of link smearing that alleviates these problems is known as *Stout smearing* [69]; it is analytic and naturally remains within $SU(3)$. It is defined via an iterative procedure

$$U_\mu^{(n+1)}(x) \;=\; e^{iQ_\mu^{(n)}(x)}\; U_\mu^{(n)}(x)\;, \tag{3.10}$$

where

$$Q_\mu(x) \;=\; \frac{i}{2}\,\left(\Omega_\mu^\dagger(x) \;-\; \Omega_\mu(x)\right) \;-\; \frac{i}{2N}\,Tr\,\left(\Omega_\mu^\dagger(x) \;-\; \Omega_\mu(x)\right)\;, \tag{3.11}$$

$$\Omega_\mu(x) \;=\; C_\mu(x)U_\mu^\dagger(x)\;, \tag{3.12}$$

and

$$\begin{aligned} C_\mu(x) \;=\; & \sum_{\nu\neq\mu} \rho_{\mu\nu}\,\left[U_\nu(x)\,U_\mu(x\;+\;\hat{\nu})\,U_\nu^\dagger(x\;+\;\hat{\mu})\right] \\ & +\;\left[U_\nu^\dagger(x\;-\;\hat{\nu})\,U_\mu(x\;-\;\hat{\nu})\,U_\nu(x\;-\;\hat{\nu}\;+\;\hat{\mu})\right]\;. \end{aligned} \tag{3.13}$$

$C_\mu(x)$ is a sum over perpendicular staples beginning at point x and ending at point $x + \hat{\mu}$, weighted by tunable real parameters $\rho_{\mu\nu}$. The matrix $Q_\mu(x) \in SU(N)$ is defined to be traceless and hermitian, implying that $e^{iQ_\mu(x)} \in SU(N)$, eliminating the need to arbitrarily project back into the gauge group. The fuzzing step (3.10) can be iterated n_ρ times to produce what are known as *stout links* $U_\mu^{(n_\rho)}$.

It is worth noting that an imaginary choice for the weights $\rho_{\mu\nu}$ does not reduce the UV fluctuations of the fuzzed links and that the choice of $C_\mu(x)$ is not unique. For further details on stout smearing and its usual implementation see [69].

On our ensembles, the spatially directed gauge links are stout smeared in order to reduce the contribution from the high energy UV modes of the gauge field. The use of this smearing scheme has also allowed the configurations to be generated using the *Rational Hybrid Monte Carlo algorithm* [70].

3.2 Correlator Construction and Distillation

We now continue our discussion of smearing, but in this section we focus on smearing the quark fields. As previously mentioned, in order to measure the energies of low-lying states, it is of particular importance to construct interpolators that overlap predominantly with light modes, with smearing being a well established method of doing so.

A simple way of smearing quark fields is via the application of a *smoothing function*, that should effectively remove the noisy short-range modes which do not make a significant contribution to low-energy physics of interest. One such construction is that of the *Jacobi method* [71]. This method is based upon the three dimensional

gauge-covariant lattice Laplacian

$$-\nabla^2_{xy}(t) \;=\; 6\delta_{xy} \;-\; \sum_{j=1}^{3}\Big[U_j(x,t)\delta_{x+\hat{j},y} \;+\; U_j^{\dagger}(x \;-\; \hat{j},t)\delta_{x-\hat{j},y}\Big] \;, \tag{3.14}$$

where the gauge fields, U_j, can be constructed from a suitable smearing scheme such as stout smearing (see section 3.1). The suppression of high energy modes comes from the exponentiation of this operator. Thus, defining the *Jacobi smearing operator* as

$$J(t) \;=\; \left(1 \;+\; \frac{\sigma\nabla^2(t)}{n_\sigma}\right)^{n_\sigma} \;, \tag{3.15}$$

where σ and n_σ are tunable parameters, will exponentially suppress the high energy modes since

$$\lim_{n_\sigma \,\to\, \infty} J(t) \;=\; e^{\sigma\nabla^2} \;. \tag{3.16}$$

The method of quark smearing used in this work is known as *distillation* [72], where the Jacobi smearing operator, $J(t)$, is approximated by the formation of an eigenvector representation of ∇^2, and is replaced by the *distillation operator*

$$P_{xy}(t) \;=\; \sum_{i=1}^{N} f(\lambda)\; v_x^{(i)}(t)\; v_y^{\dagger(i)}(t) \;, \tag{3.17}$$

where $v_x^{(i)}(t)$ is the i^{th} eigenvector of ∇^2 evaluated on the background of the spatial gauge fields of time-slice t, once the eigenvectors have been sorted by eigenvalue λ. $P_{xy}(t)$ is the projection operator into the N-dimensional subspace, V_N, spanned by these eigenvectors, and is therefore idempotent. When the dimension of $V_N = V_M$, where $M \;=\; N_c \times L_x \times L_y \times L_z$, the distillation operator becomes the identity and the quark fields are unsmeared. It is also important to note that correlation functions constructed with distilled fields have the same symmetry properties as those constructed using Laplacian smearing techniques [72].

Distillation is as follows. For simplicity, consider a momentum projected local mesonic interpolator $\mathcal{O}_i^\dagger = \bar{\psi}\Gamma^i\psi$, where Γ^i is one of the combinations of gamma matrices shown in Table 3.1. The application of the distillation operator gives

$$\mathcal{O}_i^\dagger(t) \;=\; \bar{\psi}_x(t)P_{xy}(t)e^{-i\vec{p}y}\;\Gamma^i_{yz}(t)\;P_{zw}(t)\psi_w(t)\;, \tag{3.18}$$

where one sums over repeated spatial indices. The 2-pt correlation function built from distilled interpolators is given via (suppressing indices)

$$C_{ij}(t) \;=\; \langle\; \bar{\psi}(t)P(t)\Gamma^i(t)P(t)\psi(t)\;\bar{\psi}(0)P(0)\Gamma^j(0)P(0)\psi(0)\;\rangle\;. \tag{3.19}$$

After performing Berezin integration of the quark fields, one then replaces the distillation operator by its outer product definition (3.17) to produce

$$C_{ij}(t) \;=\; \mathrm{Tr}\;\left[\;\phi^j(t)\tau(t,0)\;\phi^i(0)\tau(0,t)\;\right]\;, \tag{3.20}$$

where

$$\phi^i_{\alpha\beta} \;=\; V^\dagger(t)\left[\Gamma^i(t)\right]_{\alpha\beta}V(t)\;. \tag{3.21}$$

Here, the i^{th} column of $V^\dagger(t)$ contains the i^{th} eigenvector of ∇^2 evaluated on time-slice t. ϕ encodes the structure and momentum of the meson, while

$$\tau_{\alpha\beta}(t,0) \;=\; V^\dagger(t)M^{-1}_{\alpha\beta}(t,0)V(0) \tag{3.22}$$

encodes the propagation of the quarks and is known as a *perambulator*. ϕ and τ are square matrices of dimension $N \times N_\sigma$ where $N_\sigma = 4$ is the number of spin components in a lattice Dirac spinor. Therefore it requires just $N \times N_\sigma$ operations of the inverse of the fermion matrix on a vector in order to compute all elements of τ. Once the perambulators have been computed and stored, the correlation of any

source and sink interpolators can be computed *a posteriori*.

This method straightforwardly extends to non-local interpolators, interpolators composed of more than two quark fields, and interpolators with a multi-hadron structure.

In summary, we use the distillation method of quark smearing, which has proven in the past to increase the overlap of interpolators with low-lying states [72, 73]. Once the perambulators have been stored, this method also allows us to compute any source and sink combination *a posteriori*, without any further inversions.

3.3 Interpolator Construction

As previously mentioned, two-point correlation functions can be written as the spectral decomposition

$$C_{ij}(t) = \sum_n \frac{Z_i^{n*} Z_j^n}{2E_n} e^{-E_n t} , \tag{3.23}$$

where the vacuum-state matrix elements

$$Z_i^n = \langle n|\mathcal{O}_i^\dagger|0\rangle , \tag{3.24}$$

are known as *overlaps*. In this work, mesonic spectral information will follow from analysis of two-point correlation functions formed from a large basis of interpolators having mesonic quantum numbers.

As mentioned earlier, the simplest such interpolators are colour-singlet local fermion bilinears (3.6). These interpolators allow access to a limited set of quantum numbers, $J^{P(C)} = 0^{-+}, 0^{++}, 1^{++}, 1^{++}, 1^{+-}$, and hence a limited number of states. In order to maximise the spectral information that can be extracted from correlation functions, we employ a large basis of local and spatially extended distilled interpolators [62, 74];

three dimensional gauge covariant derivatives are placed inside a fermion bilinear to construct interpolators of the general form

$$\mathcal{O}^{A\dagger}_{ff'} = \sum_x \bar{\psi}_f(\vec{x},t)\Gamma^A \overleftrightarrow{D}_i \overleftrightarrow{D}_j \ldots \psi_{f'}(\vec{x},t) \,, \tag{3.25}$$

where the *backward-forward* derivative $\overleftrightarrow{D} \equiv \overleftarrow{D} - \overrightarrow{D}$ is *chosen* in order to have interpolators of definite charge conjugation symmetry when $f = f'$, even at non-zero momentum. A labels the different combinations of gamma matrices as shown in Table 3.1.

Using continuum $SO(3)$ rotational symmetry, one can construct interpolators of definite spin, parity and charge conjugation at zero momentum. The strategy is to form a circular basis of vector-like derivatives and gamma matrices so that they transform as $J = 1$. For creation interpolators, we use

$$\overleftrightarrow{D}_{m=\pm 1} = i \sum_i \epsilon_i^*(\vec{0},\pm 1)\overleftrightarrow{D}_i = \mp \frac{i}{\sqrt{2}}(\overleftrightarrow{D}_x \mp i \overleftrightarrow{D}_y), \tag{3.26}$$

$$\overleftrightarrow{D}_{m=0} = i \sum_i \epsilon_i^*(\vec{0},0)\overleftrightarrow{D}_i = i\overleftrightarrow{D}_z \,. \tag{3.27}$$

Then, using the standard $SO(3)$ *Clebsch-Gordan coefficients*, an interpolator of definite spin, J, and J_z-component, M, can be formed

$$(\Gamma \times D^{[1]}_{J=1})^{J,M} = \sum_{m_1,m_2} \langle 1,m_1;1,m_2|J,M\rangle \; \bar{\psi}_f \; \Gamma_{m_1} \overleftrightarrow{D}_{m_2} \psi_{f'} \,, \tag{3.28}$$

where the choice of $\Gamma_{m_1}\overleftrightarrow{D}_{m_2}$ sets the parity and charge conjugation. A note on our notation is required: an interpolator $(\Gamma \times D^{[n]}_{J_D})^{J,M}$ contains a combination of gamma matrices, Γ, with the naming scheme given in Table 3.1, and n derivatives coupled to spin J_D, with the overall combination coupled to spin-J and J_z-component M.

For a two-derivative interpolator, the convention is to first couple the two derivatives to a definite spin J_D, and then coupling to the vector-like gamma matrix,

$$(\Gamma \times D^{[2]}_{J_D})^{J,M} = \sum_{m_1,m_2,m_3,m_D} \langle 1, m_3; J_D, m_D | J, M \rangle \times \langle 1, m_1; 1, m_2 | J_D, m_D \rangle \; \bar{\psi}_f \; \Gamma_{m_3} \overleftrightarrow{D}_{m_1} \overleftrightarrow{D}_{m_2} \psi_{f'} \; . \tag{3.29}$$

It is instructive to note that, even though the Clebsch-Gordan for $1 \otimes 1 \to 1$ is anti-symmetric and $\overleftrightarrow{D}_{m_1} \overleftrightarrow{D}_{m_2}$ appears to be symmetric, there are still non-zero interpolators with $J_D = 1$ due to the non-abelian nature of QCD. These interpolators are proportional to the field strength tensor, which does not vanish on non-trivial configurations. It is interpolators of this type that will be used to probe excited gluonic degrees of freedom, and identify candidate hybrid mesons in chapter 7.

When considering interpolators containing three derivatives, a decision on how to couple the derivatives must be made. A natural choice comes from requiring that the interpolator will have a definite charge conjugation symmetry for $f = f'$. By exchanging the quark and anti-quark fields, the charge conjugation operation effectively acts as a transpose of the operators between the quark fields; for three derivatives then, one ensures definite charge conjugation by coupling the outermost derivatives together first since this gives them a definite exchange symmetry

$$(\Gamma \times D^{[3]}_{J_{13},J_D})^{J,M} = \sum_{m_1,m_2,m_3,m_4,m_{13}m_D} \langle 1, m_4; J_D, m_D | J, M \rangle \times \langle 1, m_2; J_{13}, m_{13} | J_D, m_D \rangle \; \langle 1, m_1; 1, m_3 | J_{13}, m_{13} \rangle \times \bar{\psi}_f \; \Gamma_{m_4} \overleftrightarrow{D}_{m_1} \overleftrightarrow{D}_{m_2} \overleftrightarrow{D}_{m_3} \psi_{f'} \; . \tag{3.30}$$

It is clear that this formulation can be extended to any number of derivatives. In this

J	$\Lambda(\dim)$
0	$A_1(1)$
1	$T_1(3)$
2	$T_2(3) \oplus E(2)$
3	$T_1(3) \oplus T_2(3) \oplus A_2(1)$
4	$A_1(1) \oplus T_1(3) \oplus T_2(3) \oplus E(2)$

TABLE 3.2: Continuum spins, $J \leq 4$, subduced into lattice irreps, $\Lambda(\dim)$, where dim is the dimension of the irrep.

work all combinations of gamma matrices and derivatives are used up to three derivatives. This provides access to all J^{PC} combinations for $J \leq 4$[1]. These interpolators are eigenstates of parity; when there are an even (odd) number of covariant derivatives, the parity is equal to (opposite to) that of the local interpolator containing the same gamma matrix. When $f = f'$, the interpolator is also an eigenstate of charge conjugation. In the case when the quark fields are not of the same flavour but are degenerate, C-parity is trivially generalised to a G-parity-like symmetry. In the case where the quark fields are not of the same flavour and are non-degenerate, charge conjugation, or any generalisation of it, is no longer a symmetry of the system, and states are labelled only by J^P. As a result, states created that would have different charge conjugation symmetry can mix to form eigenstates of the QCD Hamiltonian, an effect that will be discussed further in sections 3.5 and 6.5.

Due to the cubic nature of our finite volume, the full three-dimensional rotational symmetry of the continuum is reduced to that of the cubic group $\mathrm{O_h^D}$. As a consequence, the infinite number of irreducible representations (*irreps*) labelled by spin J, are contained within a finite number of lattice irreps. Mesonic states at rest will belong to one or more of the five single-cover irreps of $\mathrm{O_h^D}$; A_1, A_2, E, T_1 and T_2. In

[1]Except for the exotic combination 4^{+-}, which requires four derivative interpolators

Λ	Λ^{-+}	Λ^{--}	Λ^{++}	Λ^{+-}
A_1	12	6	13	5
A_2	4	6	5	5
T_1	18	26	22	22
T_2	18	18	22	14
E	14	12	17	9

TABLE 3.3: The number of interpolators used in each lattice irrep, Λ^{PC}, for the study of the charmonium spectrum. All combinations of gamma matrices and up to three derivatives are included.

order for the interpolators described above to be of any use in a lattice calculation, the various components, M, of a spin J interpolator must be *subduced* into lattice irreps [62, 74]; the result of which is shown in Table 3.2 for $J \leq 4$. Subduction proceeds via

$$\mathcal{O}^{[J]}_{\Lambda,\lambda} \equiv \sum_M S^{J,M}_{\Lambda,\lambda} \left(\Gamma \times D^{[n]}\right)^{J,M} = \sum_M S^{J,M}_{\Lambda,\lambda} \mathcal{O}^{J,M} , \tag{3.31}$$

where $\lambda = 1 \ldots \dim(\Lambda)$ is the *row* of the irrep Λ. $S^{J,M}_{\Lambda,\lambda}$ are the *subduction coefficients* and are constructed as follows. For a $J = 0$ interpolator, the subduction is trivial since spin zero only appears in the one-dimensional irrep A_1. Therefore $S^{0,0}_{A_1,1} = 1$. $J = 1$ interpolators can only be faithfully subduced into T_1, which is three-dimensional. Hence we use

$$S^{1,M}_{T_1,\lambda} = \delta_{\lambda,(2-M)} , \tag{3.32}$$

where $(2 - M)$ is used so that $1 \leq \lambda \leq \dim(T_1)$. Interpolators with $J \geq 2$ can be subduced across multiple irreps and are constructed by iteration starting from the

Λ	Λ^-	Λ^+
A_1	18	18
A_2	10	10
T_1	44	44
T_2	36	36
E	26	26

TABLE 3.4: The number of operators used in each lattice irrep, Λ^P, for the study of the charm-light and charm-strange spectra. All combinations of gamma matrices and up to three derivatives are included.

$J = 0$ and $J = 1$ coefficients via

$$S^{J,M}_{\Lambda,\lambda} = \sum_{\lambda_1,\lambda_2} \sum_{M_1,M_2} S^{J_1,M_1}_{\Lambda_1,\lambda_1} S^{J_2,M_2}_{\Lambda_2,\lambda_2} C(\Lambda_1 \otimes \Lambda_2 \to \Lambda) \langle J_1, M_1; J_2, M_2 | J, M \rangle \ , \quad (3.33)$$

where $C(\Lambda_1 \otimes \Lambda_2 \to \Lambda)$ is the octahedral group Clebsch-Gordan coefficient for $\Lambda_1 \otimes \Lambda_2 \to \Lambda$. The explicit values for the subduction coefficients up to $J \leq 4$ can be found in [62].

The number of operators used for each Λ^{PC} combination for the study of the charmonium spectrum is shown in Table 3.3. Table 3.4 shows the number of operators used in each Λ^P for the study of the charm-light and charm-strange spectra.

For irreps that are of a dimension two or higher, the same correlation functions are calculated for each row, λ, of the irrep. We average over these rows in order to obtain a final value of the correlation function for that irrep.

In summary, in all of our spectroscopic calculations we employ a large basis of interpolators ranging a variety of spatial structures. A key point in their construction is that, in the continuum, they have definite J^{PC} allowing a spin identification scheme to be set up. We use all combinations of gamma matrices and derivatives up to three derivatives, which allows us to access to all J^{PC} combinations up to

and including states of spin-4. From here on out, we will refer to the interpolators described in this section as the *J_z-basis* interpolators.

3.3.1 Mesonic Interpolators at Non-Zero Momentum

We now discuss our preferred construction of mesonic interpolators at non-zero momentum. We use these interpolators in the calculation of the dispersion relations in the open-charm sector, as described in section 2.3, and in the construction of multi-hadron interpolators in section 8.1.1.

The construction of interpolators at non-zero momentum is rather more involved than for interpolators at rest; simply Lorentz boosting interpolators at rest does not suffice, since one is required to take into account the reduced symmetry of the system, that is, the *little group* of allowed cubic rotations that leave the meson momentum invariant [75]. These so-called *in flight* interpolators must transform irreducibly under this reduced symmetry group.

The J_z-basis interpolators, $\mathcal{O}^{J,M}$, in the continuum with $\vec{p} = 0$, have a definite spin-J and spin z-component M. However, at non-zero-momentum, M is no longer a good quantum number unless the momentum is directed along the z-axis. In [76], the authors show that it is more convenient to work with interpolators of a definite helicity, that is, the projection of the spin component along the direction of $\vec{p}$. So-called *helicity interpolators* can be constructed via (in an infinite volume continuum)

$$\mathbb{O}^{J,\lambda}(\vec{p}) \;=\; \sum_{M} \mathcal{D}^{(J)*}_{M\lambda}(R)\; \mathcal{O}^{J,M}(\vec{p}) \;, \tag{3.34}$$

where $\mathbb{O}^{J,\lambda}(\vec{p})$ is a helicity interpolator with helicity λ. $\mathcal{D}^{(J)*}_{M\lambda}(R)$ is a Wigner-$\mathcal{D}$ matrix, and R is the active transformation that rotates $(0, 0, |\vec{p}|)$ to $\vec{p}$.

Lattice Momentum	Little Group	Irreps ($\Lambda^{(P)}$)
$(0,0,0)$	O_h^D	$A_1^{\pm}, A_2^{\pm}, E^{\pm}, T_1^{\pm}, T_2^{\pm}$
$(n,0,0)$	Dic_4	A_1, A_2, B_1, B_2, E_2
$(n,n,0)$	Dic_2	A_1, A_2, B_1, B_2
(n,n,n)	Dic_3	A_1, A_2, E_2
$(n,m,0)$	C_4	A_1, A_2
(n,n,m)	C_4	A_1, A_2
(n,m,p)	C_2	A

TABLE 3.5: The allowed lattice momenta on a finite cubic lattice along with their corresponding little groups. The A and B irreps are of dimension one, E two and T three. Dic_n is the dicyclic group of order $4n$. Parity is only a good quantum number for $\vec{P} = (0,0,0)$. Here $n \neq m \neq p$.

At non-zero momentum in an infinite volume continuum, the little group is the same regardless of the momentum direction. However, in a finite volume, the particular lattice little group depends on the *star* of $\vec{p}$ [75], that is, the set of all $\vec{p}$ related by allowed lattice rotations. Different stars of $\vec{p}$ are known as *momentum types* [76]. The momentum types, their corresponding little groups and their lattice irreps are shown in Table 3.5. Helicity interpolators are subduced into a given irrep in the same fashion as described in section 3.3, but of course with different subduction coefficients; these are given in [76].

R is a matrix required to rotate from $(0,0,|\vec{p}|)$, which is not necessarily an allowed lattice momentum, to $\vec{p}$, which is an allowed lattice momentum. In practise, we break R down into two stages, $R = R_{lat}R_{ref}$, where R_{ref} rotates from $(0,0,|\vec{p}|)$ to $\vec{p}_{ref}$ and R_{lat} is a lattice rotation from $\vec{p}_{ref}$ to $\vec{p}$. The choice of R_{lat} is not important as long as it is consistently used for a given momentum direction. It is useful to consider the following example. Consider the momentum directions that give $p^2 = 2$, and *choose* $\vec{p}_{ref} = (0,1,1)$. Requiring the final momentum to be $\vec{p} = (0,1,1)$, then $R = R_{ref}$ is just a rotation from $(0,0,p)$ to $\vec{p}$. On the other hand, requiring the final

momentum to be $\vec{p} = (1,1,0)$, then $R = R_{lat}R_{ref}$ where R_{ref} is as before and R_{lat} is a lattice rotation from $(0,1,1)$ to $(1,1,0)$.

For further details on helicity interpolators and their (alternate) constructions, see [61, 76], where they also list the relevant subduction coefficients for several momentum types.

3.4 Analysis of Two-Point Functions

In our study of the charmonium and open-charm spectra, we construct correlation functions built from the J_z-basis interpolators. We use all combinations of γ matrices and derivatives up to three derivatives. As discussed in section 3.3, this allows us to access all $J^{P(C)}$ combinations up to spin four, and also gives us a probe of gluonic degrees of freedom.

For each symmetry channel and flavour sector we compute an $N \times N$ matrix of correlation functions

$$C_{ij} = \langle 0|\mathcal{O}_i(t)\ \mathcal{O}_j^\dagger(0)|0\rangle\ , \tag{3.35}$$

where i and j label the interpolators in the basis of a given symmetry channel. N is the number of interpolators used in a symmetry channel, which is given in Table 3.3 for the study of the charmonium spectrum, and Table 3.4 for the study of the open-charm spectra. In each of these symmetry channels we then employ the *variational technique* [77, 78]. This method of spectral extraction, which is now in common usage throughout the lattice community, takes advantage of a redundancy of interpolators in a given symmetry channel. Practically, this amounts to solving

the generalised eigenvalue problem

$$C(t)v^n(t) = \lambda_n(t)C(t_0)v^n(t) \ , \tag{3.36}$$

where $\lambda_n(t_0) = 1$, and there is an orthogonality between the eigenvectors of different states

$$v^{n'\dagger}C(t_0)v^n = \delta_{n,n'} \ . \tag{3.37}$$

The eigenvalues are known as *principal correlators* and at large times behave like

$$\lambda_n(t) = e^{-E_n(t-t_0)}\left(1 + O(e^{-\Delta E_n(t-t_0)}\right) \ , \tag{3.38}$$

where E_n is the energy of the n^{th} state when the eigenvalues are placed in ascending order. Typically, we find that the energy gap ΔE_n lies outside of the first N states as suggested in [79]. We solve this generalised eigenvalue problem using singular value decomposition, but other methods such as Cholesky decomposition has been previously applied [80]. The spectral decomposition of a given correlation matrix has the form

$$C_{ij} = \sum_n \frac{Z_i^{n\dagger}Z_j^n}{2E_n}e^{-E_n t} \ , \tag{3.39}$$

where the amplitudes, Z_i^n, are known as *overlaps* and are given by

$$Z_i^n = \langle 0|\mathcal{O}_i|n\rangle = (V^{-1})_i^n\sqrt{2E_n}e^{E_n t_0/2} \ . \tag{3.40}$$

The choice of t_0 plays a crucial role in the correct extraction of spectroscopic states. The eigenvectors are forced by the solution procedure to be orthogonal on the metric $C(t_0)$, but since we use a finite number of interpolators in our basis, this orthogonality will only be a good approximation if the correlator at t_0 is dominated by the lightest $\dim(N)$ states. This suggests that we should choose t_0 large enough so that

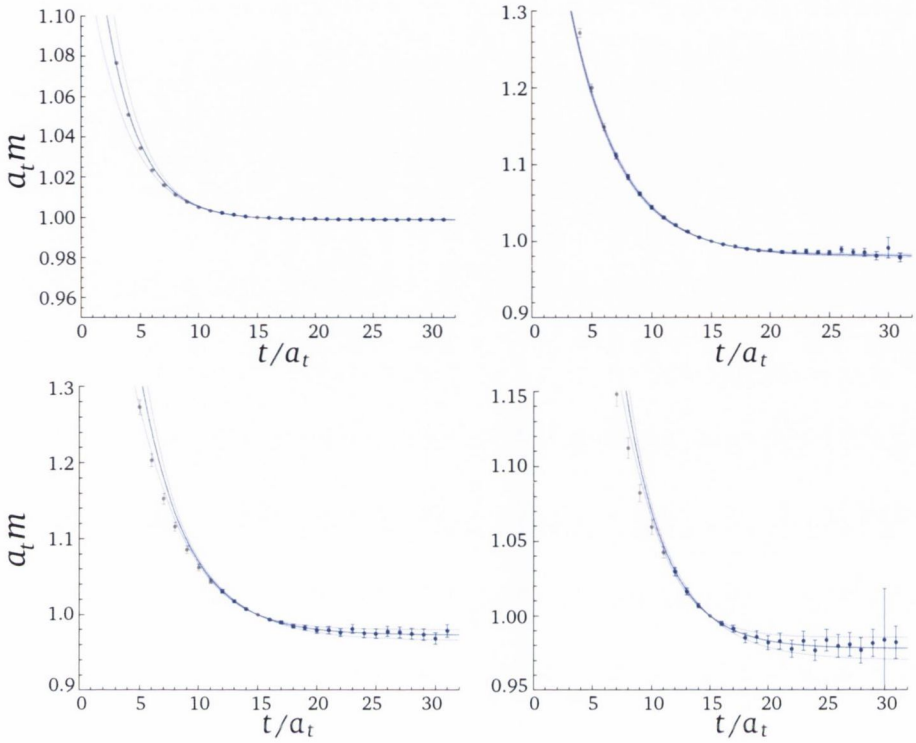

FIGURE 3.2: Principal correlator fits, according to equation (3.41), to the lightest four states in the T_1^{--} irrep of the charmonium spectrum on the $24^3 \times 128$ volume. The data points are given by $\lambda^n(t) \cdot e^{m_n(t-t_0)}$ and the fits are for $t_0 = 15$. The error bars show the one sigma statistical uncertainty, while the grey points are not included in the fits.

the correlator is dominated by the lightest N states, but we must be careful not to choose a t_0 too high, as the signal may begin to degrade. In chapter 4, we perform some systematic tests, one of which is the variation of the spectrum due to different choices of t_0.

We fit our principal correlators using either a single exponential or a sum of two exponentials with the constraint $\lambda(t = t_0) = 1$. The two exponential fit used is

$$\lambda_n = (1 - A_n)e^{-E_n(t-t_0)} + A_n e^{-E_{n'}(t-t_0)} , \tag{3.41}$$

where the fit parameters are $E_n, E_{n'}$ and A_n. The second exponential is added in order to *mop up* the excited state contamination. Empirically, we find that the contribution of the second exponential decreases rapidly as t_0 is increased. On this premise, we do not consider further the parameters $E_{n'}$ and A_n. Figure 3.2 shows a selection of fits to principal correlators of the form (3.41), in the T_1^{--} symmetry channel from our calculation of the charmonium spectrum. These are plotted with the dominant time-dependence due to state n divided out, so we would see a horizontal line at 1 in the case where a single exponential dominates the fit.

For each principal correlator fit, 3.41, the choice of fit range is chosen to include as many points as possible such that the fit has $\chi^2/(d.o.f) \sim 1$. Typically, we find that the ranges $t_0 = 3 - 8$ and $t = 20 - 30$ satisy this constraint. Variation within these given ranges for t_0 and t usually amounts to a less than one percent difference in the extracted energy, E, and usually lies within our statistical error.

Using the variational technique combined with our large basis of distilled interpolators has proven to be very successful in past studies of the light meson [62, 73, 74] and baryonic sectors [81, 82].

Now that we have extracted the spectroscopic states, all that remains is the difficult task of identifying the spin of these states in a reliable manner. This will be the subject of the following section.

3.5 Spin Identification

The spin identification, for all but the lightest spectroscopic states in a given sector, has been a long standing problem on the lattice. In principle, the spin of single-hadron states can be identified by computing the spectrum at finer and finer

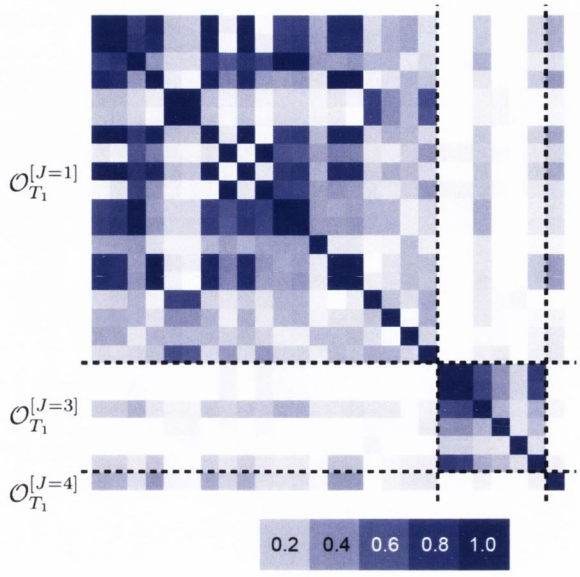

FIGURE 3.3: The normalised correlation matrix, $(C_{ij}/\sqrt{C_{ii}C_{jj}})$, on time-slice five in the T_1^{--} irrep of the charmonium spectrum on the $24^3 \times 128$ volume. The interpolators are ordered such that those subduced from spin-1 appear first, followed by spin-3 and spin-4. It is clear that the correlation matrix is observed to be approximately block diagonal in spin.

lattice spacings and then extrapolating to the continuum limit; when full rotational symmetry is restored, degeneracies will emerge between different irreps of $\mathrm{O}_{\mathrm{h}}^{\mathrm{D}}$. For example, due to the pattern of subductions, a state of spin-two will appear as degenerate states in the E and T_2 irreps. Two major difficulties arise with this method. Firstly, in order keep statistical precision under control at successively finer lattice spacings requires the sort of computational power that is currently impractical. Secondly, and perhaps more fundamentally, the continuum spectrum can exhibit natural degenerate or near degenerate states, which is especially relevant for mesons containing heavy quarks since hyperfine splittings are known to be small. For example, a state with $J^{PC} = 4^{++}$ will have its components distributed across the lattice irreps, A_1, T_1, E and T_2. Using this method of spin identification, we would expect to see degenerate states in each of these irreps as we go to smaller lattice spacings.

However, this will also be the pattern of energy levels for separate $0^{++}, 1^{++}$ and 2^{++} states. Since states with these quantum numbers are expected to appear within the same quark model supermultiplet (P-wave), the splitting between these states is expected to be small. Hence, a 4^{++} state could be misinterpreted as separate $0^{++}, 1^{++}$ and 2^{++} states and vice versa.

As we will see in chapters 5 and 6, the dense spectrum of excited states would be impossible to disentangle by only having information on their energies. This is particularly important for the charm-light and charm-strange spectra; the lack of charge conjugation symmetry will reduce the number of symmetry channels which can be used to separate the states. Hence, the spectrum in each symmetry channel becomes more dense than, for example, in charmonium.

It would be useful to have a method that alleviates these difficulties, and is effective when using data from only one lattice spacing. Of course, the single lattice spacing should be fine enough so that rotational symmetry is restored to such a point that one still describes QCD. Such a method was proposed by the Hadron Spectrum Collaboration in [62, 74]. The idea is to consider vacuum-state matrix elements (overlaps) of carefully constructed interpolators as a source of additional information. Our interpolators are constructed are constructed such that they have a definite $J^{P(C)}$ in the continuum. They are then subduced into the relevant symmetry channels of the lattice. However, it is clear from their construction, that each interpolator carries a *memory* of the continuum spin from which it was subduced. If our lattice is reasonably close to restoring rotational symmetry, then we would expect an interpolator subduced from spin-J to predominantly overlap onto states that have spin-J in the continuum limit [83].

We find this statement to be true, even at the level of the correlation matrix. Figure 3.3 shows the normalised correlation matrix, $(C_{ij}/\sqrt{C_{ii}C_{jj}})$, on time-slice five in the

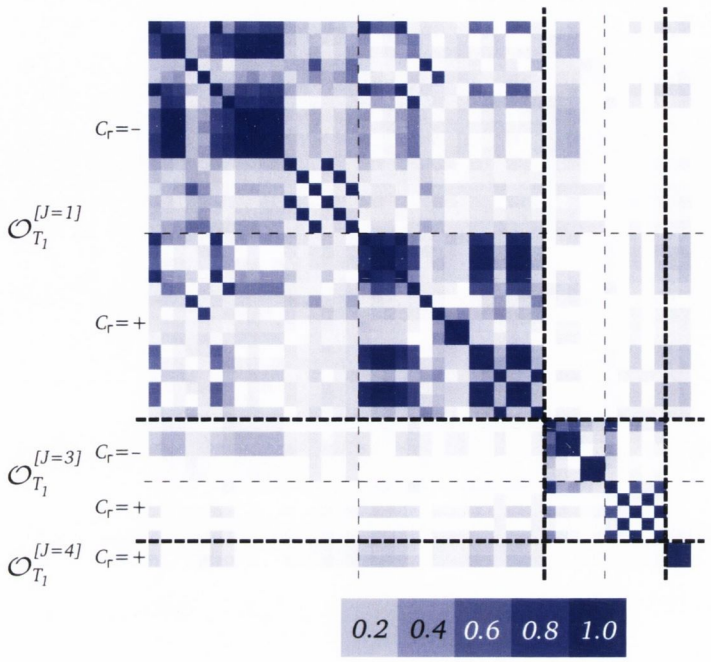

FIGURE 3.4: The normalised correlation matrix, $(C_{ij}/\sqrt{C_{ii}C_{jj}})$, on time-slice five in the T_1^+ irrep of the charm-light spectrum on the $24^3 \times 128$ volume. The interpolators are by continuum spin, J, as shown by the labelling; spin-1 followed by spin-3 and spin-4. For each value of spin-J, they are then ordered according to their symmetry $C_\Gamma = \pm$, as described in the text. It is clear that the correlation matrix is observed to be approximately block diagonal in spin.

T_1^{--} irrep of the charmonium spectrum on our $24^3 \times 128$ volume. It is clear that when the interpolators are ordered according to the spin from which they were subduced, that the correlation matrix has a block diagonal structure. Figure 3.4 shows a similar plot, but this time in the T_1^+ irrep of the charm-light spectrum. Flavoured mesons are not eigenstates of charge conjugation and hence states that would be distinguished by charge conjugation symmetry can mix. Our interpolator construction (see section 3.3) is designed to have well defined transformation properties under transposition of the operator, Γ, in the bilinear, $\Gamma^T = \pm\Gamma$. We denote the eigenvalue under this transformation as $C_\Gamma = \pm 1$. It is clear from Figure 3.4 that interpolators

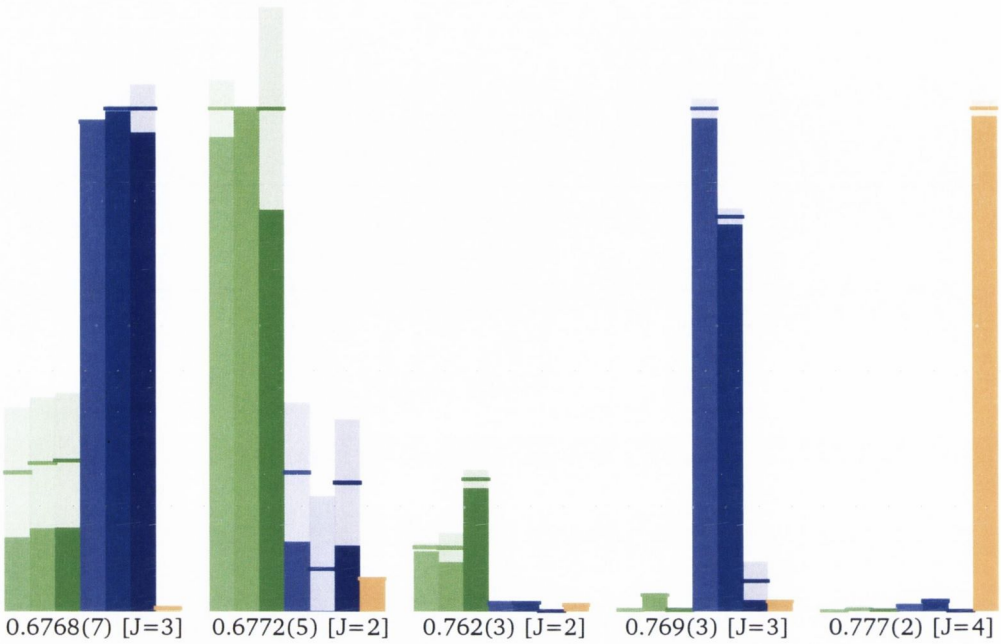

FIGURE 3.5: The overlaps, Z, of a selection of interpolators onto a selection of states in the T_2^{--} irrep of the charmonium spectrum on our $24^3 \times 128$ volume. The states are labelled by their mass in lattice units $a_t m$, and by the continuum spin of the dominant interpolators. In this plot, the overlaps have been normalised so that the largest value of an interpolators across all states is equal to unity. The shaded region near the top of each state shows the one sigma statistical uncertainty. For each state, the interpolators are coloured according to the continuum spin of an interpolator: spin-2 is green, spin-3 is blue and spin-4 is orange. A darker shade of a given colour signifies that the interpolator is proportional to the field strength tensor. For each state the interpolators are, from left to right: $(a_1 \times D^{[1]]}_{J=1})^{[J=2]}$, $(a_1 \times D^{[3]}_{J_{13}=2,J=3})^{[J=2]}$, $(\rho \times D^{[2]}_{J=2})^{[J=2]}$, $(a_0 \times D^{[3]}_{J_{13}=2,J=3})^{[J=3]}$, $(a_1 \times D^{[3]}_{J_{13}=2,J=3})^{[J=3]}$, $(\rho \times D^{[2]}_{J=2})^{[J=3]}$, $(a_1 \times D^{[3]}_{J_{13}=2,J=3})^{[J=4]}$.

with $C_\Gamma = +$ and $C_\Gamma = -$ have significant overlap with each other. Also evident from this figure is the block diagonal structure in spin, which suggests, just as in the charmonium case, that interpolators subduced from, say, spin-1 have little contribution to the spin-3 and spin-4 states.

This effect is even more evident at the level of individual states. Our overlaps,

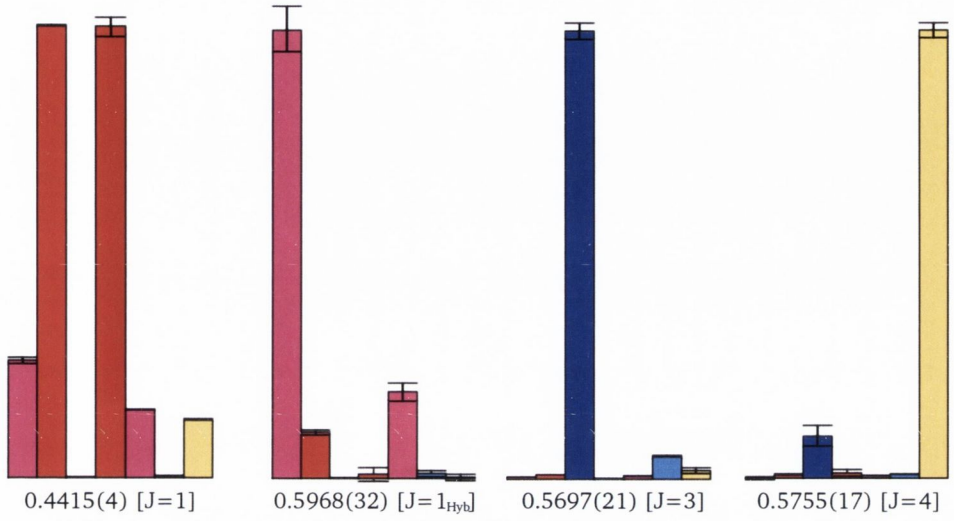

FIGURE 3.6: The overlaps, Z, of a selection of operators onto a selection of states in the charm-strange (D_s) T_1^+ irrep on the 24^3 volume. In this plot the overlaps have been normalised so that the largest value for an operator across all states is equal to unity. The error bars indicate the one sigma statistical uncertainty. For each state, the operators are coloured from left to right as: pink $(a_0 \times D^{[2]}_{J=1})^{[J=1]}$, red $(b_1 \times D^{[2]}_{J=0})^{[J=1]}$, blue $(b_1 \times D^{[2]}_{J=2})^{[J=3]}$, red $(\rho \times D^{[1]}_{J=1})^{[J=1]}$, pink $(\rho \times D^{[3]}_{J_{13}=2,J=2})^{[J=1]}$, light blue $(\rho \times D^{[3]}_{J_{13}=2,J=2})^{[J=3]}$, and gold $(\rho \times D^{[3]}_{J_{13}=2,J=3})^{[J=4]}$. The first three operator insertions have negative symmetry ($C_\Gamma = -$) and the last four have positive symmetry ($C_\Gamma = +$) as explained in the text. States are labelled by their mass in temporal lattice units and the continuum spin of the dominant operators. 'Hyb' refers to a state which has relatively strong overlap with operators that are proportional to the field strength tensor, the commutator of two gauge-covariant derivatives.

$Z_i^n = \langle 0|\mathcal{O}_i|n\rangle$, for a given state show a clear preference for overlap onto interpolators of a single spin. This is evident in Figures 3.5 and 3.6, where we show a selection of overlaps, Z_i^n, for a selection of states in the T_2^{--} irrep of the charmonium spectrum, and the T_1^+ irrep of the charm-strange spectrum, both on the $24^3 \times 128$ volume. The colour scheme in these figures is as follows: $J = 0$ is black, $J = 1$ is red, $J = 2$ is green, $J = 3$ is blue and $J = 4$ is orange. Interpolators that are proportional to the field strength tensor are coloured in a darker shade in Figure 3.5 and in a lighter

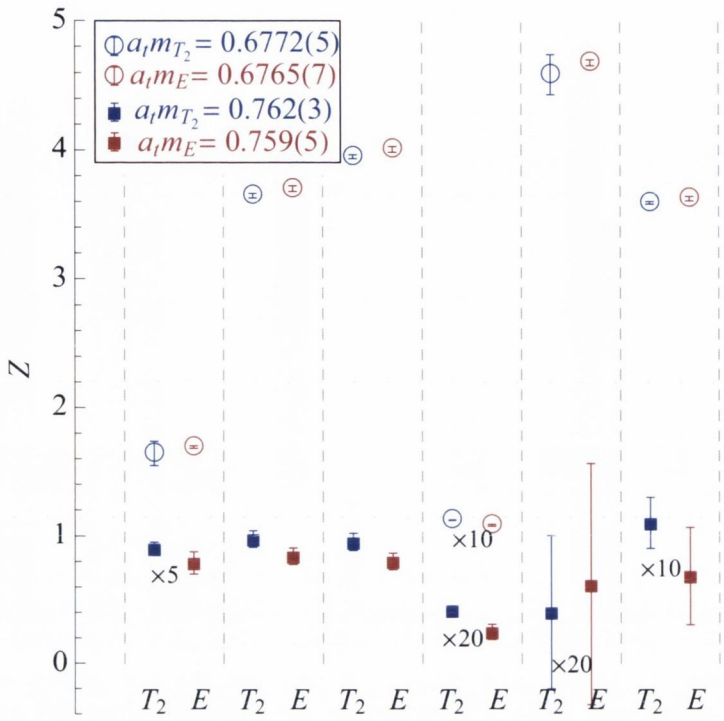

FIGURE 3.7: A selection of Z-values for states conjectured to have $J = 2$ in irreps Λ^{--} of the charmonium spectrum on our 128×24^3 volume. From left to right, the interpolators are $(a_1 \times D^{[1]}_{J=1})^{J=2}$, $(\rho_2 \times D^{[2]}_{J=2})^{J=2}$, $(\rho \times D^{[2]}_{J=2})^{J=2}$, $(a_0 \times D^{[3]}_{J_{13}=2,J=2})^{J=2}$, $(a_1 \times D^{[3]}_{J_{13}=0,J=1})^{J=2}$ and $(a_1 \times D^{[3]}_{J_{13}=2,J=1})^{J=2}$.

shade in Figure 3.6. We show only a subset of interpolators and states here, but similar patterns occur throughout all of the spectra.

To be more quantitative, we can compare overlap values between different irreps. Our interpolators are constructed to have definite continuum spin, so

$$\langle J', M' | \mathcal{O}^{J,M\dagger} | 0 \rangle = Z^{[J]} \delta_{J,J'} \delta_{M,M'} \ , \tag{3.42}$$

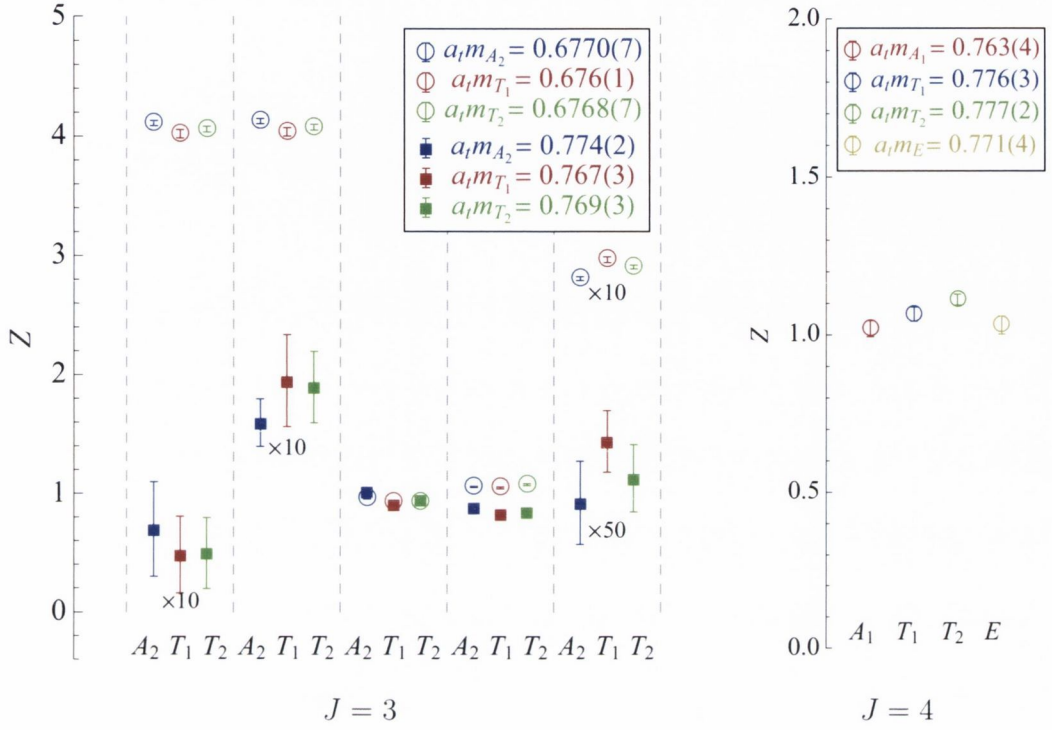

FIGURE 3.8: A selection of Z-values for states conjectured to have spin-3 (left) and spin-4 (right) in irreps Λ^{--} of the charmonium spectrum on our 128×24^3 volume. From left to right, the interpolators in the left panel are $(\rho_2 \times D^{[2]}_{J=2})^{J=3}$, $(\rho \times D^{[2]}_{J=2})^{J=3}$, $(a_0 \times D^{[3]}_{J_{13}=2,J=3})^{J=3}$, $(a_1 \times D^{[3]}_{J_{13}=2,J=3})^{J=3}$, $(b_1 \times D^{[3]}_{J_{13}=1,J=2})^{J=3}$; the interpolator in the right panel is $(a_1 \times D^{[3]}_{J_{13}=2,J=3})^{J=4}$.

and therefore when subduced to the lattice

$$\langle J', M' | \mathcal{O}^{[J]\dagger}_{\Lambda,\lambda} | 0 \rangle = S^{J,M'}_{\Lambda,\lambda} Z^{[J]} \delta_{J,J'} \ . \tag{3.43}$$

This implies that the value of $Z^{[J]}$ is common to different lattice irreps up to discretisation effects and a choice of normalisation of the subduction coefficients. This gives us further information that we can use to identify the spin of a state: we can compare the Z values obtained independently in different irreps. For example, a $J = 2$ state created by a $\mathcal{O}^{[J=2]}_{\Lambda}$ interpolator will have the same Z value in both the

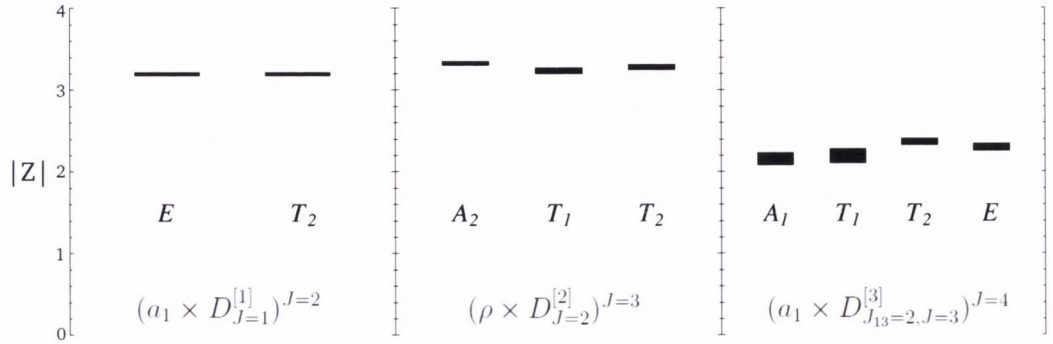

FIGURE 3.9: A selection of absolute Z-values for the lightest states conjectured to have $J = 2$ (left pane), $J = 3$ (middle pane), $J = 4$ (right pane) in charm-strange irreps, Λ^-, on the 24^3 volume. For each J we show the values of Z for the same interpolator subduced into different irreps. The vertical size of a box corresponds to the one-sigma statistical uncertainty on either side of the mean.

E and T_2 irreps, once we suitably normalise the subduction coefficients. If this is the case, it is also another hint that the discretisation effects are relatively small, since they have not distorted the Z values significantly.

Figure 3.7 shows a selection of Z values for states conjectured to have continuum spin-2 in the charmonuim spectrum. In Figure 3.8 we show a selection of Z values for states conjectured to have continuum spin-3 and 4 in the charmonium spectrum, while in Figure 3.9 we show a selection of Z values for the lightest states conjectured to have continuum spin-2, 3 and 4 in the relevant irreps of the charm-strange spectrum on the $24^3 \times 128$ volume. In all of these figures there is an excellent agreement between overlaps extracted in different irreps. This observation is apparent across all of our calculated spectra though, as we expect, there are slight deviations from exact equality due to discretisation effects.

We do not expect rotational symmetry breaking terms to appear until $O(a^2)$ since there are no dimension five operators composed of quark bilinears that respect the symmetry of the lattice that do not also transform trivially under the continuum

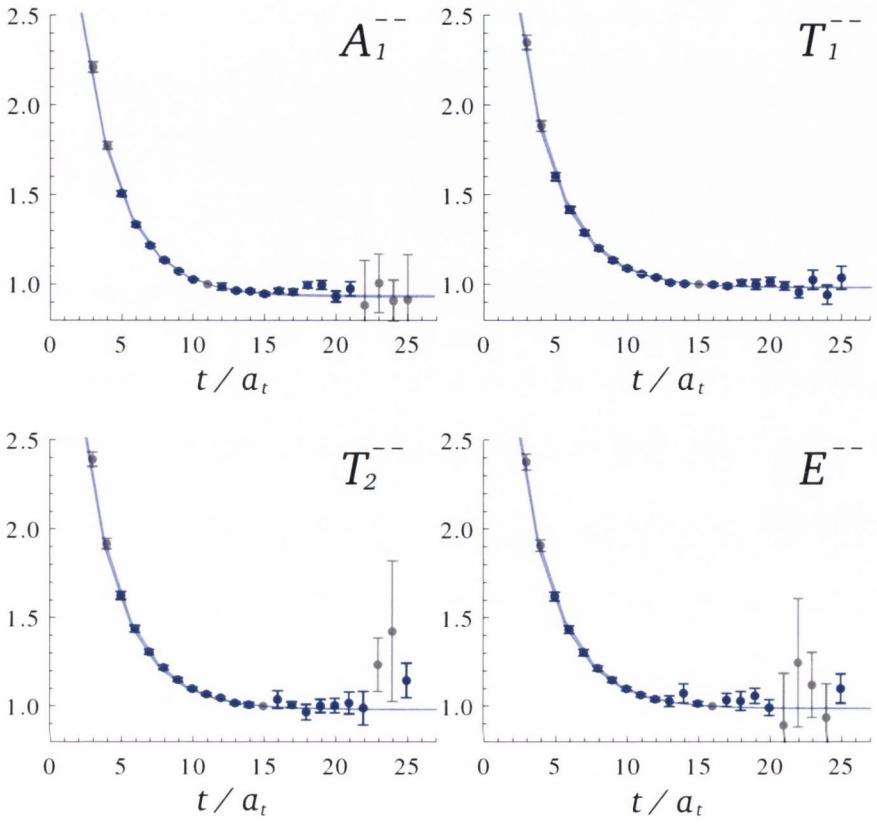

FIGURE 3.10: A simultaneous fit to the four principal correlators of the lightest 4^{--} state of the charmonium spectrum, on the 24^3 volume using a common mass, m_n. Plotted are $\lambda^n(t) \cdot e^{m_n(t-t_0)}$ data and the fit; the grey points are not included in the fit.

group of spatial rotations. Hence, we expect the rotational breaking between lattice irreps to be suppressed in both the spectrum and the overlaps [62, 83]. However, renormalisation mixing of high mass dimension interpolators (i.e. two and three derivative interpolators) with lower mass dimension interpolators can give rise to effects scaling with negative powers of the lattice spacing; we expect these to be more troublesome for using Z values to determine spin. But, in practise, the effects are not seen to be large enough to prevent the use of the method. In accordance with

[62], we suggest that it is our use of stout smeared gauge fields and distilled quark fields that renders these mixings relatively small, since the high-energy physics has been filtered out.

Given that this method of spin identification is feasible, we can confidently identify the different components of a spin-J meson subduced across different irreps. Then the question of which value to use as the final mass arises, since fits to principal correlators in different irreps may differ slightly due to lattice artefacts. Rather than taking the simplest approach, which would be to average the masses across the relevant irreps, we perform a *joint fit* to the principal correlators with a common mass. To achieve this we allow a different second exponential for each principal correlator so that the fit parameters are, the common mass m_n, and the sets of parameters $\{m_n'^{\Lambda}\}$ and $\{A_n^{\Lambda}\}$. This method has proven to be very successful in the past [62, 73, 81]. Figure 3.10 shows an example of a joint fit to the principal correlators of the lightest 4^{--} state in the four irreps $A_1^{--}, T_1^{--}, T_2^{--}$ and E^{--}. In general the fits have $\chi^2/N^{\text{dof}} \sim 1$.

In this chapter we have presented the recipe used by the Hadron Spectrum Collaboration in order to extract excited spectra. We use a large basis of local and spatially extended distilled fermionic bilinears along with the variational method in order to extract spectra up to and including spin-4. As demonstrated in this section, we can reliably identify the $J^{P(C)}$ of our extracted states using the vacuum-state overlaps, Z, and for states of $J \geq 2$, we perform joint fits across the relevant irreps to quote final values for their masses.

Chapter 4

Stability of Spectra

In this chapter we discuss to what extent the extracted spectra changes as the details of the calculation are varied, while keeping the physics constant. These systematic tests consist of variations of various parameters, such as the choice of t_0 in the variational method, the number of distillation vectors used, and the variation of hyperfine splittings due to the spatial clover coefficient. As a test case, we use charmonium, but expect the open-charm sector to behave in a very similar fashion.

4.1 Variational Analysis and the Choice of t_0

Our choice of t_0 in the variational technique is guided by the *reconstruction* method as described in [62, 80]. Here, the correlation matrix is reconstructed from the extracted masses and eigenvectors on a given time-slice from equation (3.39). This reconstructed matrix is then compared to the original data for all $t > t_0$, with the degree of agreement indicating the acceptability of the spectral decomposition. The description generally improves as one increases t_0 until at some point the increase

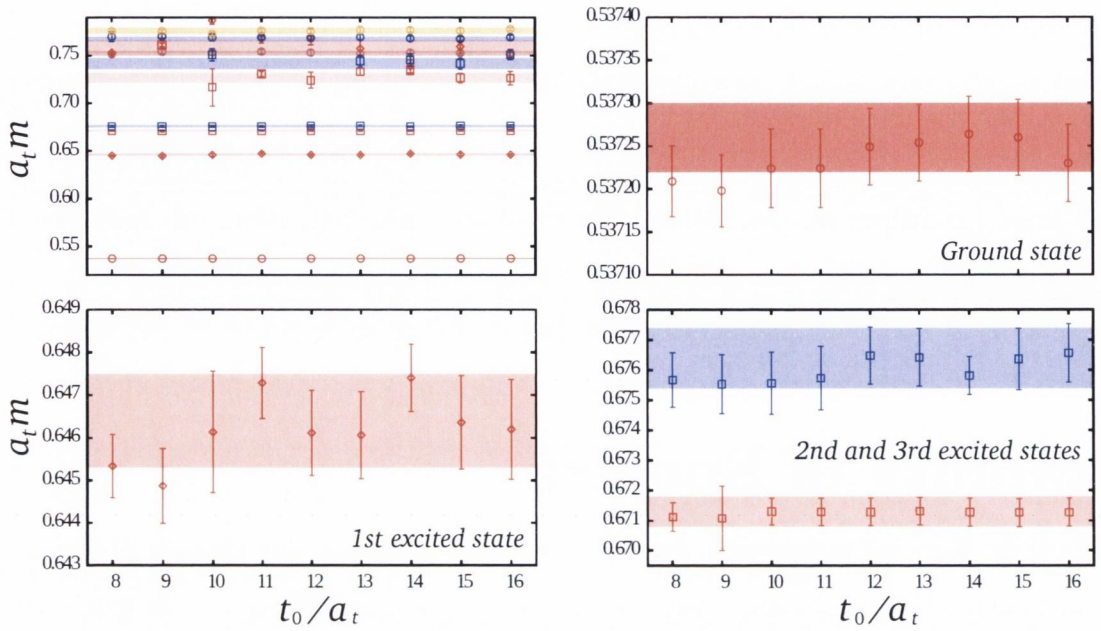

FIGURE 4.1: Extracted mass spectrum as a function of t_0 for the lower-lying states in the T_1^{--} irrep of the charmonium spectrum on the $24^3 \times 128$ volume. The top left panel shows the lightest ten states and the other panels show the lightest four states in more detail. Horizontal bands show the masses extracted at $t_0 = 15$ with the width $\pm 1\sigma$ from the mean. For large enough but not too large t_0 the spectrum is seen to be stable under changes in t_0.

in statistical noise halts the improvement. This procedure gives an insight as to the minimal t_0 for which the correlation matrix is well described by the variational solution.

Figure 4.1 shows how the lightest ten states in the T_1^{--} irrep of the charmonium spectrum on our $24^3 \times 128$ volume vary according to the chosen t_0. The horizontal bands in this figure show the extracted mass value for each state when $t_0 = 15$, while the width of each band shows the one-sigma statistical uncertainty. It is clear that, for large enough t_0, the spectrum appears stable under variations of t_0. A major factor in this stability is due to the second exponential in our fitting form; as

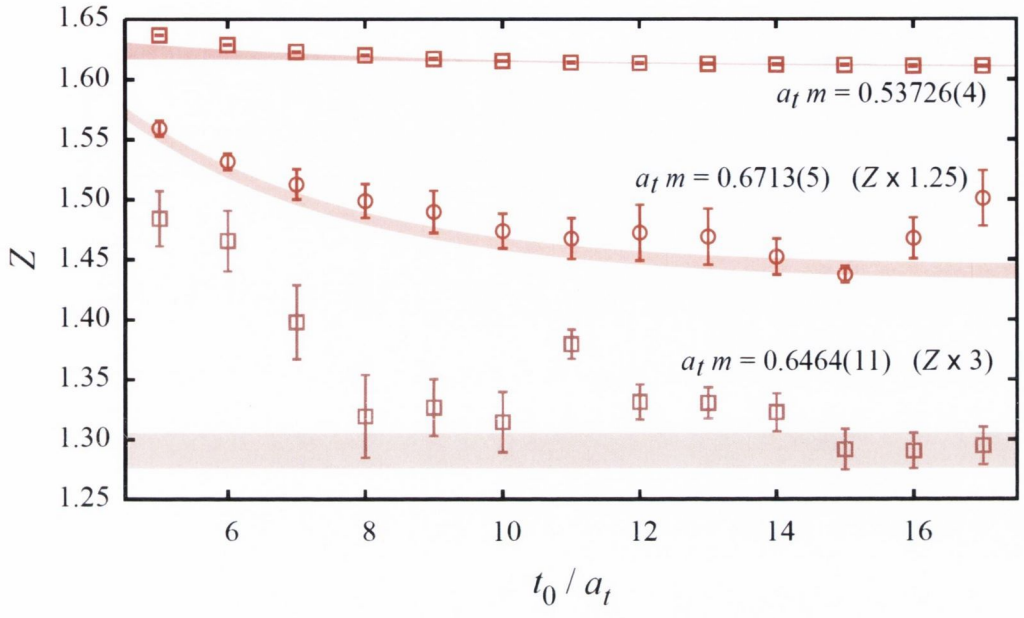

FIGURE 4.2: Extracted overlaps, Z, for interpolator $(a_1 \times D^{[1]}_{J=1})^{J=1}_{T_1}$ as a function of t_0 for the lightest three $J = 1$ states in the T_1^{--} irrep of the charmonium spectrum on the $24^3 \times 128$ volume. The Z values for the 1^{st} and 2^{nd} excited states have been arbitrarily scaled by factors of 3 and 1.25 respectively to fit on the plot. Coloured bands show fits to an exponential plus a constant or a constant over an appropriate range of t_0. The Z values are seen to plateau for sufficiently large t_0 but can show significant curvature at small t_0.

previously explained, the second exponential *mops-up* the contamination from other states leaking into the principal correlator due to finite basis. We also find that the contribution of the second exponential falls rapidly with increasing t_0.

We expect the overlaps, Z, since they are related to the eigenvectors obtained from the variational method, to be more sensitive to the variation of t_0. Figure 4.2 shows the extracted overlaps as a function of t_0 for the lightest three $J = 1$ states in the T_1^{--} irrep of the charmonium spectrum on the $24^3 \times 128$ volume. In Figure 4.3 we show extracted overlaps as a function of t_0 for the lightest $J = 4$ states in the T_1^{--}

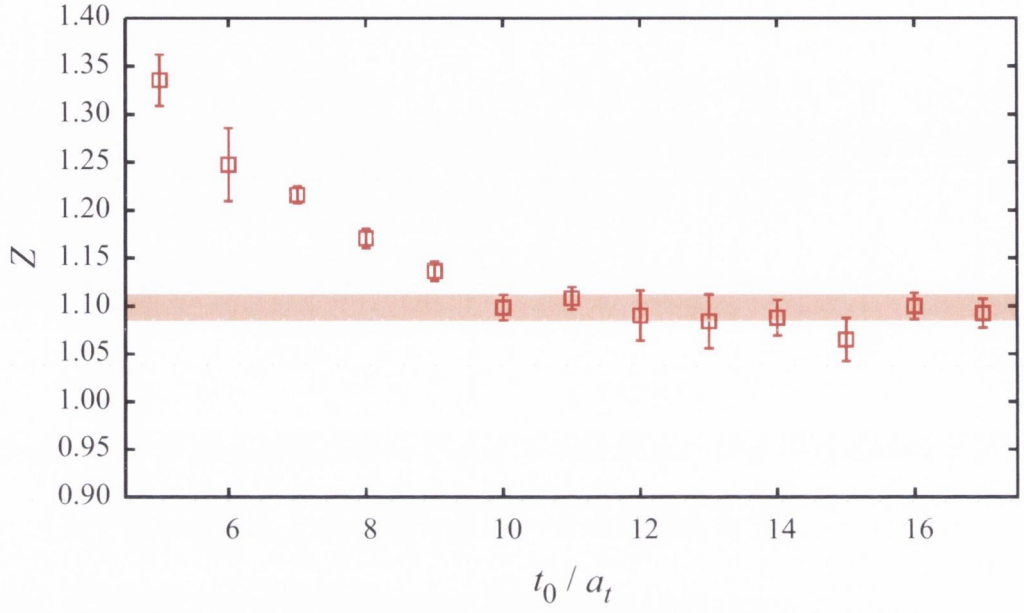

FIGURE 4.3: Extracted overlaps, Z, for interpolator $(a_1 \times D^{[3]}_{J_{13}=2,J=3})^{J=4}_{T_1}$ as a function of t_0 for the lightest $J = 4$ state in the T_1^{--} irrep of the charmonium spectrum on the $24^3 \times 128$ volume. The horizontal band shows a fit to a constant over an appropriate range of t_0. The Z value is seen to plateau for large t_0 but shows significant curvature at small t_0.

irrep of the charmonium spectrum on the $24^3 \times 128$ volume. As expected, both of these figures show that the overlaps appear to be more sensitive to the variation of t_0 than the masses; we have to go to larger t_0 values for the Z values to stabilise. For this reason we generally choose t_0 values between ten and fifteen throughout all of our spectra. Here, we have shown only masses and Z values as a function of t_0 for charmonium, so it should be noted that we observe very similar results in the open-charm spectra.

In summary, it appears that the variational technique is reliable as long as t_0 is chosen such that the Z values have stabilised; in general, the masses stabilise at

earlier t_0 values compared to the overlaps. This observation was also apparent in the calculation of the light isovector meson spectrum [73].

4.2 Number of Distillation Eigenvectors

The distillation method, as described in section 3.2, hinges on the choice of the number of eigenvectors of the Laplacian to include. Using too few eigenvectors reduces the computational cost but results in over-smearing and reduces the ability to extract higher lying states. The unsmeared limit corresponds to $N_{vecs} = 3(L/a_s)^3$, where the 3 refers to the number of colours. To achieve the same level of smearing on larger volumes requires the number of eigenvectors to be scaled by a factor equal to the ratio of spatial volumes [72]. Hence, an optimum use of the distillation method requires the use of the smallest number of eigenvectors for which the states of interest can be extracted reliably. Figure 4.4 shows the lowest-lying states in the T_1^{--} irrep of the charmonium spectrum on our $16^3 \times 128$ volume for a subset of 90 configurations with 6 time-sources per configuration. It is clear from the figure that the spectrum becomes stable for $N_{vecs} \geq 48$. The spectrum degrades in quality for fewer vectors, which becomes quite apparent for excited states.

In summary, we find that using 64 eigenvectors on the $16^3 \times 128$ volume is sufficient for the spectrum to be stable with respect to the number of eigenvectors. Since, when the number of eigenvectors is 48, the spectrum appears to become stable, we scale up to the $24^3 \times 128$ volume via $48(24/16)^3$, which suggests that 162 eigenvectors are sufficient.

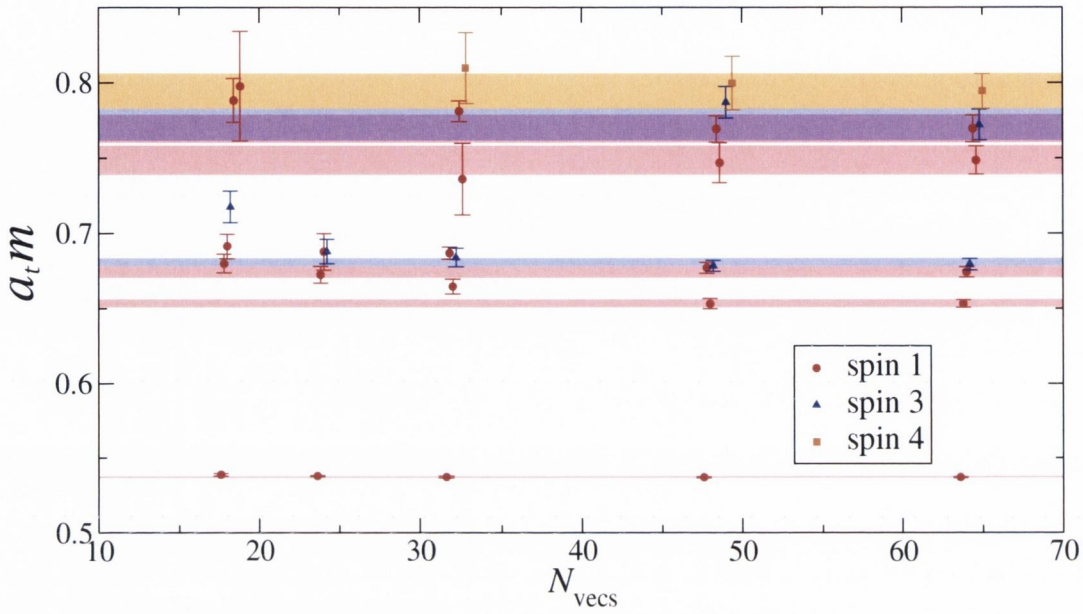

FIGURE 4.4: Extracted spectrum for the T_1^{--} irrep of the charmonium spectrum on the $16^3 \times 128$ volume as a function of the number of distillation vectors, N_{vecs}, using lower statistics than the main 16^3 results. Horizontal bands correspond to the masses extracted with $N_{\text{vecs}} = 64$ and give the one-sigma statistical uncertainty on either side of the mean. The spectrum is observed to be stable for $N_{vecs} \gtrsim 48$.

4.3 Hyperfine Splittings and $O(a_s)$ Effects

An accurate determination of hyperfine splittings for heavy flavour-singlet mesons has been a long standing problem in lattice QCD [84]. The problem is that this quantity is known to be extremely sensitive to discretisation effects arising from the Dirac operator.

On our $16^3 \times 128$ ensemble, we determine the hyperfine splitting between the lightest pseudo-scalar (η_c) and vector (J/ψ) charmonium states to be 80(2) MeV. This is consistent with our determination on the larger $24^3 \times 128$ volume, suggesting that it is not a finite volume effect. The accepted experimental value is $\approx$ 116 MeV

[48]. Our determination neglects the contribution of disconnected Wick diagrams. However, these diagrams are OZI suppressed and are not expected to contribute to the hyperfine splitting in a significant fashion [84]. We have made some first tests of their contribution and find a similar result. Another source of systematic error is due to our unphysically heavy light quarks, but again this is not expected to impact the hyperfine splitting significantly [85].

The action used for the charm quark in this study, as explained in chapter 2, is $O(a)$-improved at tree-level in tadpole-improved perturbation theory. It is expected that a non-perturbative determination of action parameters would yield a larger value of the spatial clover coefficient c_s [86]. We use a value of $c_s = 1.35$ in our simulations, but we increase this to $c_s = 2.0$ in order to investigate the effect of a larger value on the low-lying charmonium spectrum on our $16^3 \times 128$ volume. This choice was not motivated by any calculation, and is chosen only because a non-perturbative value is expected to be larger than the tadpole-improved tree-level value.

Figure 4.5 shows the lowest-lying S and P-wave states, $0^{-+}, 1^{--}, (0,1,2)^{++}$ and the exotic 1^{-+}, calculated for the original value of $c_s = 1.35$ and the increased value of $c_s = 2.0$. The calculated (experimental) mass values in this figure have the calculated (experimental) η_c mass subtracted from them, in order to reduce the small systematic error picked up in setting the bare charm quark mass.

Choosing $c_s = 2.0$, which gives a value for the $J/\psi - \eta_c$ splitting of 114(2) MeV, brings us to within statistical uncertainty of the accepted experimental value of ≈ 116 MeV. We also observe significantly better agreement with experiment for the P-wave states. The spin-2 χ_{c2} state is subduced across two irreps, T_2^{++} and E^{++}. For the increased value of c_s, the two determinations are still degenerate within statistical uncertainty. This is consistent with the explanation that the hyperfine splitting is underestimated due to $O(a)$ effects; as previously mentioned, since all

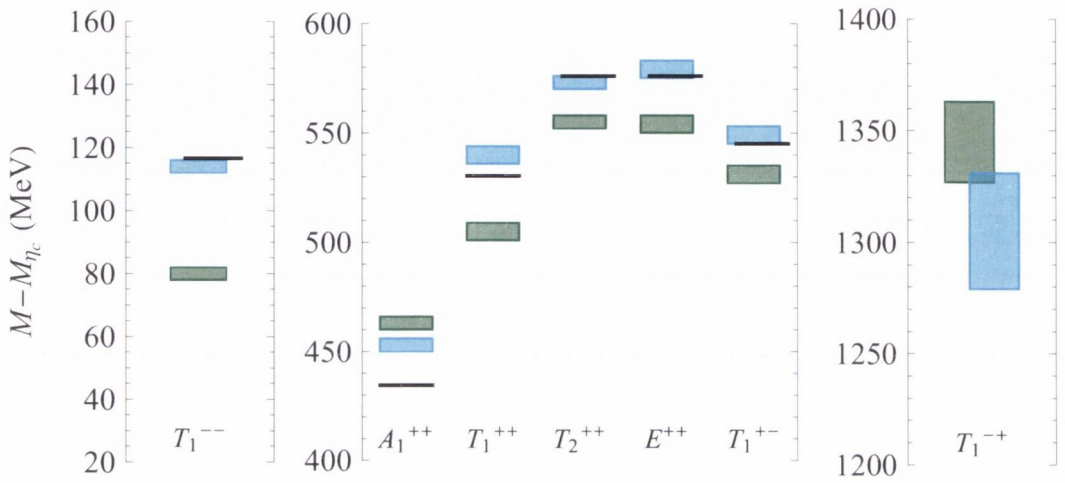

FIGURE 4.5: The mass shifts, measured on our $16^3 \times 128$ volume, for the lowest-lying states in a selected set of charmonium lattice irreps as c_s, the size of the chromomagnetic clover term, is varied from tadpole-improved tree-level value of $c_s = 1.35$ (green) to $c_s = 2$ (cyan). Masses presented here are measured relative to M_{η_c}. Experimental data is shown as solid lines; note that experimentally the χ_{c0} has a significant hadronic width.

dimension-five interpolators consistent with lattice symmetries do not break the continuum rotation group, any differences between these lattice states should only arise at $O(a^2)$ in a Symanzik-like expansion, and so are expected to be small. The lightest charmonium state with exotic quantum numbers, 1^{-+}, is observed only to have a mild dependence on c_s, suggesting that such states high up in the spectrum will be relatively close to their experimental values.

To be clear, the final results presented in chapters 5 - 8 are calculated with $c_s = 1.35$ and not with the increased value of $c_s = 2.0$. However, this test allows us to place an approximate scale of ~ 40 MeV to the size of the systematic uncertainty arising from the leading order $O(a_s)$ lattice artefacts. Of course, for full control of systematic error further investigation would be required.

We also performed the same test for the hyperfine splittings in the open-charm spectra. Using the original value of c_s, we calculate the splitting between the S-wave pseudo-scalar and vector states to be 124(1) in the charm-light sector, which is significantly lower than the experimental value of ≈ 142 MeV. In the charm-strange sector, we calculated the hyperfine splitting to be 120(1) MeV using the original c_s value. The experimental value in this case is ≈ 143 MeV. When we increased the value of the spatial clover coefficient to $c_s = 2.0$ we again achieve hyperfine splittings that are comparable with experiment; we get 144(1) in the charm-light case, and 139(1) in the charm-strange case. Following the same argument as in the charmonium case, we assign a scale of ~ 20 MeV for our leading $O(a_s)$ lattice artefacts in the open-charm sector.

Chapter 5

Hidden Charm Sector

In this chapter we present the results from our calculation of the charmonuim spectrum. Firstly we discuss the results by lattice irrep and compare the spectrum calculated on the $16^3 \times 128$ volume with that calculated on the $24^3 \times 128$ volume. We then show our final spin identified spectrum before proceeding to discuss our interpretation of the results. We delay our discussion of hybrid mesons until chapter 7.

5.1 Results by Irrep and Volume Comparison

The results of the variational analysis applied to the correlation matrix representing each lattice irrep, Λ^{PC}, is shown in Figure 5.1. The lighter shaded boxes are from the $16^3 \times 128$ volume, while the darker shaded ones are from the $24^3 \times 128$ volume. The size of the boxes indicate the one-sigma statistical uncertainty while the colour coding indicates the continuum spin as determined via the spin identification scheme discussed in section 3.5; states identified as spin-0 are coloured black, spin-1 are

coloured red, spin-2 are coloured green, spin-3 are coloured blue and spin-4 are coloured orange.

On the lattice, states that have continuum spin ≥ 2 have their components split across several irreps. As described in section 3.5, we can use, not only the masses, but the corresponding overlap values identify the continuum spin of these states. As can be seen in Figure 5.1, we generally see no significant mass differences between components of a continuum spin ≥ 2 state in different lattice irreps. This is an indication that the extracted spectrum is indeed composed of single-hadron states as one signature of multi-hadron states would be to disrupt these degeneracies. From the same figure, it is also evident that the dense spectrum of states above $a_t m \sim 0.65$ would be impossible to disentangle using only the masses. The fact that a successful spin identification is possible is an indication that the lattice size is large enough and that the lattice spacing is fine enough for an effective restoration of rotational symmetry at the hadronic scale.

Figure 5.2 shows the spin identified volume comparison labelled by continuum J^{PC}. The states coloured red in the rightmost panel are those that have exotic quantum numbers. These will be discussed further in chapter 7. This figure includes only the states that were well determined by the variational procedure. The dashed lines indicate the lowest thresholds for open-charm decay; the calculated $D\bar{D}$ and $D_s\bar{D}_s$ non-interacting levels measured on the $16^3 \times 128$ volume.

At the level of statistical precision, we observe no significant difference between the two volumes, even above the open-charm thresholds, which is more evidence that we are not seeing multi-hadron states. Furthermore, we do not see any states appearing in energy regions where we would expect non-interacting two-meson states to appear. This apparent lack of multi-hadron states has also been observed in [62], where they use the same technology in the computation of the light isovector spectrum.

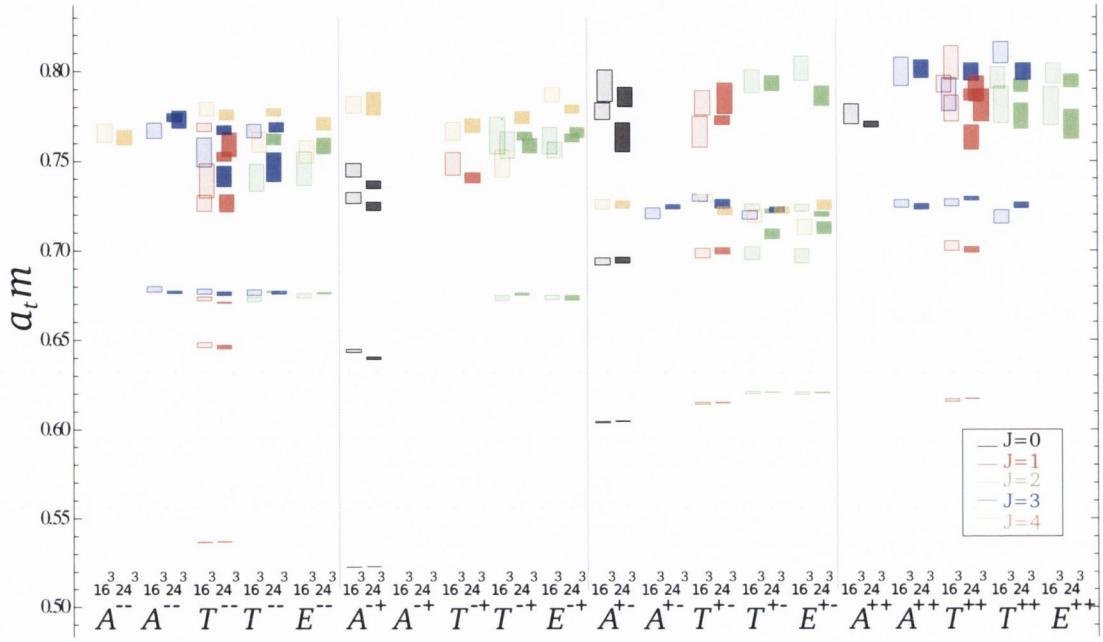

FIGURE 5.1: Extracted charmonium spectra by lattice irrep, Λ^{PC}, on the $16^3 \times 128$ (lighter shading) and $24^3 \times 128$ (darker shading) volumes. The vertical size of each box gives the one sigma statistical uncertainty on either side of the mean and the colour coding indicates the continuum spin.

5.2 Final Spin Identified Charmonium Spectrum

Figure 5.3 shows our final spin identified charmonium spectrum. We take the values calculated on our $24^3 \times 128$ volume as our final results since these were calculated with higher statistics and on a larger volume. The green boxes represent states that were well determined by the variational procedure and the black boxes represent experimentally determined states. In this figure, the calculated (experimental) value of the η_c mass has been subtracted from the calculated (experimental) masses in order to reduce the systematic error from setting the charm quark mass. The green dashing represents the non-interacting open-charm thresholds, $D\bar{D}$ and $D_s\bar{D}_s$, as

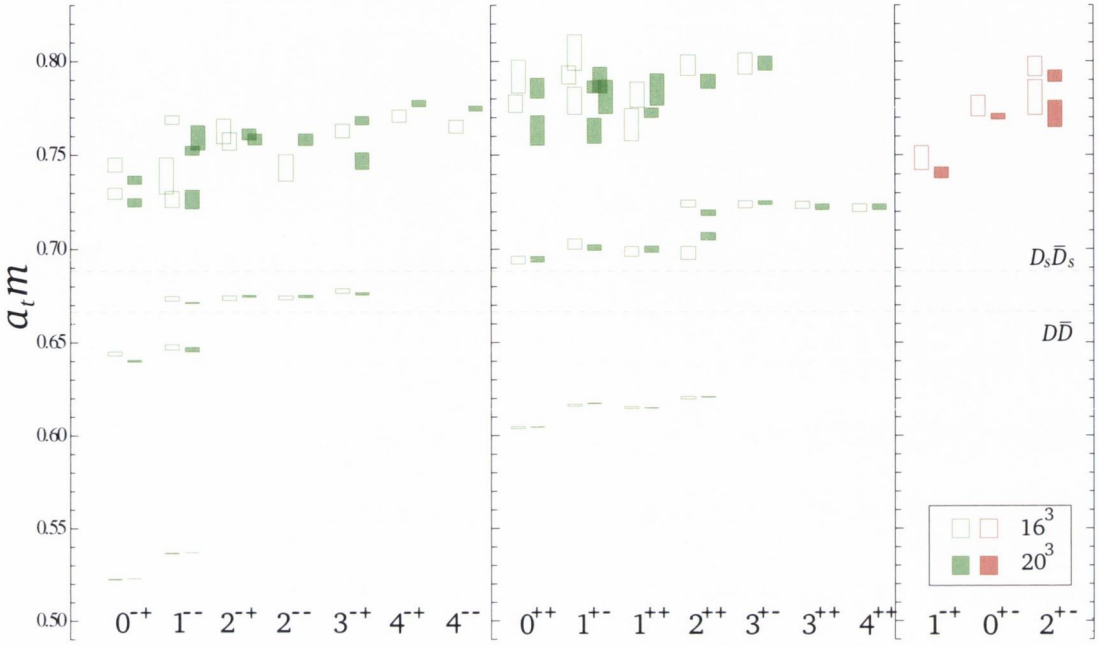

FIGURE 5.2: The extracted spin-identified charmonium spectrum labelled by J^{PC}; the $16^3 \times 128$ (open boxes) and $24^3 \times 128$ (filled boxes) volumes agree well. The vertical size of the boxes represents the one-sigma statistical uncertainty on either side of the mean. The dashed lines indicate the lowest non-interacting $D\bar{D}$ and $D_s\bar{D}_s$ levels using the D and D_s masses, as measured on our ensembles.

calculated on our $16^3 \times 128$ volume. The grey dashing indicates the same thresholds but for experimental values. The masses are tabulated in Table A.1.

It is clear from Figure 5.3 that the states become less well determined high up in the spectrum. This is expected because, even though we use a large basis of interpolators, it is still finite. To better determine these states, we would need to include interpolators of different radial structures. It is also worth noting that in order to determine states with $J \geq 5$ we would need to include interpolators with at least four derivatives.

In the next section we give our interpretation of the results, but first we discuss some

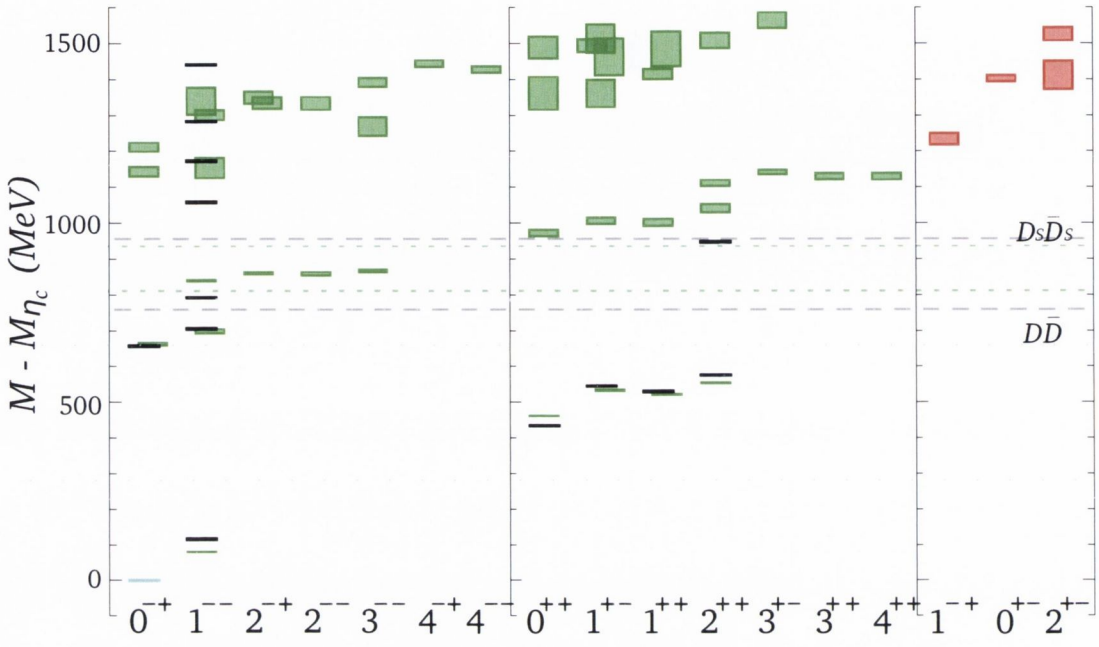

FIGURE 5.3: Summary of the charmonium spectrum up to around 4.5 GeV labelled by J^{PC}. The red and green boxes are the masses calculated on the $24^3 \times 128$ volume; black lines are experimental values from the PDG [48]. We show the calculated (experimental) masses with the calculated (experimental) η_c mass subtracted. The vertical size of the boxes represents the one-sigma statistical uncertainty. The dashed lines indicate the lowest non-interacting $D\bar{D}$ and $D_s\bar{D}_s$ levels using the D and D_s masses calculated on the $16^3 \times 128$ volume (fine green dashing) and using the experimental masses (coarse grey dashing).

other recent calculations of the charmonium spectrum. In [80], the authors present a calculation of an excited charmonium spectrum in the quenched approximation. Apart from our calculation having dynamical light and strange quarks, we also utilise a larger basis of interpolators. Due to this, we extract a much larger number of excited states and reliably identify their J^{PC}.

[87] presents an $N_f = 2$ calculation of the charmonium spectrum. They also consider mixing with some light meson and multi-hadron states. The same authors have also

presented preliminary $N_f = 2$ results in [85]. They use a range of pion masses and lattice spacings, but the main drawback is their small interpolator basis, which makes a robust spin identification of excited states difficult.

In [88], the Fermilab and MILC collaborations investigate quarkonium mass splittings using asqtad improved staggered fermions on ensembles with three flavours of sea quarks. For heavy quarks they employ the Fermilab interpretation of the clover action for Wilson fermions. Most of their calculated splittings agree well with experiment; For example, they find a value of 116.0 ± 7.4 MeV for the charmonium $1S$ hyperfine splitting, which is remarkably close to the experimental value of 116.4 ± 1.2 MeV.

5.3 Interpretation of Charmonium Spectrum

Most of the states with non-exotic J^{PC} appear to follow the quark model pattern of states, $n^{2S+1}L_J$, obtained by coupling the spin of the quarks, S, to the angular momentum of the system, L, in order to produce a total angular momentum (Spin), J. Here, n is the radial quantum number. This pattern of states forms so-called *supermultiplets* of states, which are shown in Table 5.1. The $^{2S+1}L_J$ assignment of our states is determined by considering operator-state overlaps which was first described in [89].

In the left panel of Figure 5.3, we present the negative parity sector of our calculated charmonium spectrum. We calculate the ground state S-wave pair $[0^{-+}, 1^{--}]$ and their first excitation at $M - M_{\eta_c} \sim 700$ MeV. We observe a second excitation at $M - M_{\eta_c} \sim 1150$ MeV. There is a complete D-wave supermultiplet at $M - M_{\eta_c} \sim 850$ MeV, just above the $D\bar{D}$ threshold. Just above $M - M_{\eta_c} \sim 1200$ MeV, there is an

$J_g^{P_gC_g}$	L	S	J^{PC}
–	$0(S)$	0	0^{-+}
		1	1^{--}
–	$1(P)$	0	1^{+-}
		1	$(0,1,2)^{++}$
–	$2(D)$	0	2^{-+}
		1	$(1,2,3)^{--}$
–	$3(F)$	0	3^{+-}
		1	$(2,3,4)^{++}$
–	$4(G)$	0	4^{-+}
		1	$(3,4,5)^{--}$
1^{+-}	$0(S)$	0	1^{--}
		1	$(0,\mathbf{1},2)^{-+}$
1^{+-}	$1(P)$	0	$(0,1,2)^{++}$
		1	$(\mathbf{0},1,1,1,\mathbf{2},\mathbf{2},3)^{+-}$

TABLE 5.1: Supermultiplets for quark-antiquark pairs with spin S and relative orbital angular momentum L. Also shown are some hybrid supermultiplets, discussed in chapter 7, where $J_g^{P_gC_g}$ are the quantum numbers of the gluonic excitation; exotic J^{PC} are shown in bold.

excited D wave set. In the same energy region there is also parts of what appears to be a G-wave set, which is indicated by the presence of spin-4 states. We do not observe the full G wave set as this would require us to observe a spin-5 state. This is difficult with the current interpolator basis since it would require the use of four derivative interpolators. Around $M - M_{\eta_c} \sim 1300$ MeV, there are three states, $[(0,2)^{-+}, 1^{--}]$, that do not appear to fit into the $^{2S+1}L_J$ pattern suggested by the quark model. These states have relatively large overlap with interpolators that are proportional to the field strength tensor, which is something not observed for states that fit into quark model supermultiplets. Following the suggestions of [62], we interpret these states as non-exotic hybrid mesons and discuss them further in chapter 7.

The middle panel of Figure 5.3 shows the positive parity sector of our charmonium

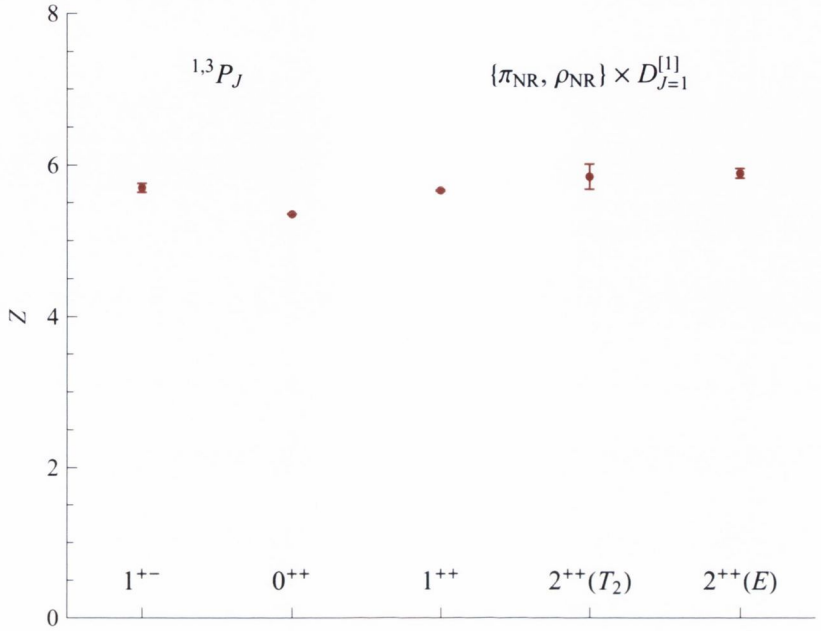

FIGURE 5.4: Overlaps, Z, for the lightest P-wave supermultiplet with interpolators $\{\pi, \rho\}_{\rm NR} \times D^{[1]}_{J=1}$ and $\{\pi, \rho\}_{\rm NR} \times D^{[2]}_{J=2}$ respectively.

spectrum. Well below the $D\bar{D}$ threshold at $M - M_{\eta_c} \sim 500$ MeV, we observe a P-wave set, $[(0,1,2)^{++}, 1^{+-}]$. Around $M - M_{\eta_c} \sim 1000$ MeV, there is an excited P-wave set, and just above this, a full F-wave set $[(2,3,4)^{++}, 3^{+-}]$. The band of states around $M - M_{\eta_c} \sim 1400$ MeV probably contains part of the second excitation of the P-wave and several non-exotic hybrids which lies significantly above the first set of negative parity hybrids.

The right panel of Figure 5.3 shows states with exotic J^{PC}, $1^{-+}, 0^{+-}$ and 2^{+-}; therefore they can't consist of solely a quark-anti-quark pair as other degrees of freedom are needed to produce these J^{PC}. We delay their discussion until chapter 7.

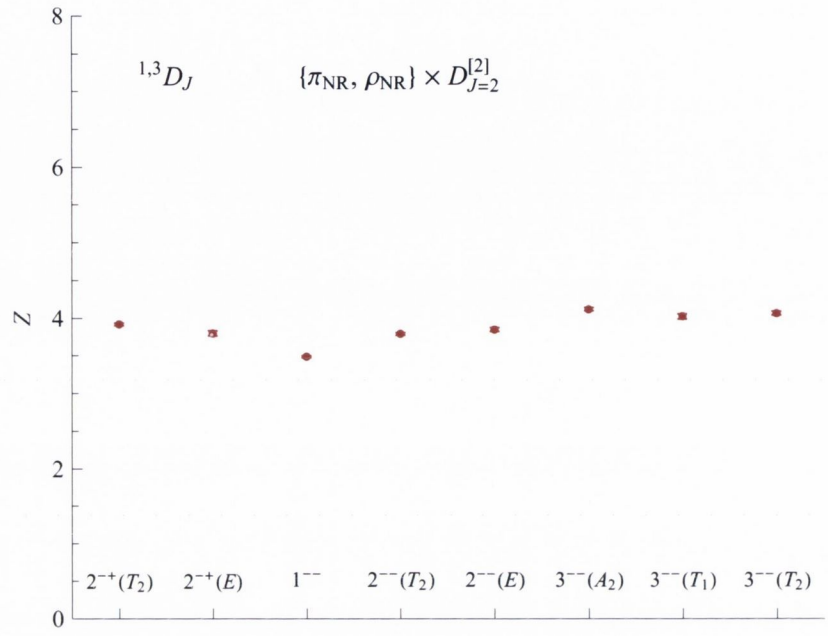

FIGURE 5.5: Overlaps, Z, for the lightest D-wave supermultiplet with interpolators $\{\pi, \rho\}_{\rm NR} \times D^{[1]}_{J=1}$ and $\{\pi, \rho\}_{\rm NR} \times D^{[2]}_{J=2}$ respectively.

As mentioned above, we use operator-state overlaps to assign states into a given supermultiplet. As a demonstration of this, consider the following interpolators: $(\pi_{NR} \times D^{[1]}_{J=1})^{J=1}$ with $J^{PC} = 1^{+-}$, and $(\rho_{NR} \times D^{[1]}_{J=1})^{[J=0,1,2]}$ with $J^{PC} = (0,1,2)^{++}$, where $\rho_{NR} = \frac{1}{2}\gamma_i(1-\gamma_0)$ and $\rho_{NR} = \frac{1}{2}\gamma_5(1-\gamma_0)$. These interpolators have the structure of quark-antiquark pair in a gauge covariant version of a P-wave with $S = 0$ (π_{NR}) or $S = 1$ (ρ_{NR}). The interpolators $(\pi_{NR} \times D^{[2]}_{J=2})^{J=2}$ with $J^{PC} = 2^{-+}$ and $(\rho_{NR} \times D^{[2]}_{J=2})^{J=1,2,3}$ with $J^{PC} = (1,2,3)^{--}$ have the structure of a quark-antiquark pair in D-wave with $S = 0$ or $S = 1$.

Figures 5.4 and 5.5 show the overlaps of these interpolators with states suggested to be members of the P-wave and D-wave supermultiplets. We observe that these overlaps are significant, and in general we find that overlaps onto non-relativistic

interpolators are large. This is not very surprising since the charmonium system is reasonably non-relativistic. Our interpretation of these states as being in the same supermultiplet is further supported by the fact that they have very similar Z values, as shown in Figures 5.4 and 5.5. We expect the Z values of states in the same supermultiplet to be similar because they correspond to the same underlying spatial wavefunction with differing internal spin and angular momentum couplings.

It is important to note that we only draw qualitative conclusions from Z values; lattice regularised matrix elements require renormalisation to be compared with continuum matrix elements, and this renormalisation can mix interpolators.

5.4 Comparison with Experiment

In Figure 5.3 the green boxes are our calculated states and the black boxes are experimental states. It can be seen that there is generally good agreement between our calculated states and the experimental states below the open-charm thresholds. States above threshold can have relatively large hadronic widths, and our mass values are only accurate up to this width. There are some discrepancies, but these could be due to discretisation effects and the use of unphysically heavy quarks. However, we do not expect the heavy light quark masses to introduce a large error for states below threshold, but we note that this could be important at and above threshold. As discussed in section 4.3, we significantly underestimate the S-wave hyperfine splitting, but we have demonstrated in section 4.3 that this is due to the use of a tree-level tadpole-improved value of the spatial clover coefficient.

We identify our first excited states in the 0^{-+} and 1^{--} channels with the experimentally verified $\eta_c(2S)$ and $\psi(2S)$ states. Slightly further up in the 1^{--} channel,

we identify our lowest D-wave state with the experimental $\psi(3770)$ determination. Even further up in the 1^{--} channel we show two experimental states $\psi(4040)$ and $\psi(4160)$. We have some candidates in this mass region but a definite assignment can not be made. As noted before, we need to add interpolators with different spatial structure in order to better determine the high-lying states. Additionally, increasing the number of distillation vectors may improve high-lying determinations.

The experimentally interesting $Y(4260)$ which lies at $M - M_{\eta_c} \sim 1300$ MeV with $J^{PC} = 1^{--}$, is one of the states supernumerary to the quark model pattern. One possible interpretation of this state is a non-exotic hybrid meson. The mass of the 1^{--} hybrid in our calculation agrees well with the mass of the $Y(4260)$, which supports the hybrid interpretation. However, we also find conventional charmonia with $J^{PC} = 1^{--}$ in the same energy region, and hence can not rule out the possibility of a standard charmonium interpretation, or the possibility of a multi-hadron or tetra-quark interpretation. An interesting observation is that, our 1^{--} hybrid candidate has a significant overlap onto an operator which has the structure of a colour-octet quark-antiquark pair with $S = 0$ in S-wave coupled to the gluonic field, $(\pi \times D^{[2]}_{J=1})^{J=1}$, which is in contrast to conventional 1^{--} mesons which have $S = 1$. The interesting point is that the $Y(4260)$ decays to $\pi^+\pi^- J/\psi$ [48]. The common consensus is that such decays should conserve the spin of the heavy quarks. Hence, one would expect that the $Y(4260)$ has $S = 1$, at odds with our $S = 0$ hybrid. However, the observation by CLEO [90] of a cross-section for $e^+e^- \to \pi^+\pi^- h_c$ at a center of mass energy of 4170 MeV suggests that the common consensus could be mistaken, since the h_c has $S = 0$.

Another of the enigmatic experimental observations is that of the $X(3872)$. It has been suggested that this is a $D\bar{D}^*$ molecular state, since it sits only a few MeV above this threshold. Recently, the LHCb experiment [91] has confirmed that this state

has $J^{PC} = 1^{++}$. This rules out the earlier possibility of the state having $J^{PC} = 2^{-+}$. This assignment favours non-standard explanations such as the $D\bar{D}^*$ molecule. In this work we do not appear to see multi-hadron states and hence would not expect to observe such a molecular state. To determine such a state would require the addition of interpolators that overlap strongly with multi-hadron states.

Chapter 6

Open-Charm Sector

In this chapter, the charm-light and charm-strange spectra are presented. Firstly, we discuss the volume dependence, before moving on to show our final spin identified spectra. We then proceed to interpret our results and compare to experiment, before discussing the mixing between spin-singlet and spin-triplet states. The discussion of hybrid mesons is delayed until chapter 7.

6.1 Volume Comparison in the Charm-Light and Charm-Strange Sectors

The results of the variational procedure for all lattice irreps in the charm-light and charm-strange sectors are shown in Figures 6.1 and 6.2 respectively. The states are labelled by irrep, Λ^P (recall that for flavoured mesons, charge conjugation is not a good quantum number), and by the colour coding shown in the plot. The left column of each irrep column represents the $24^3 \times 128$ volume results, while the right

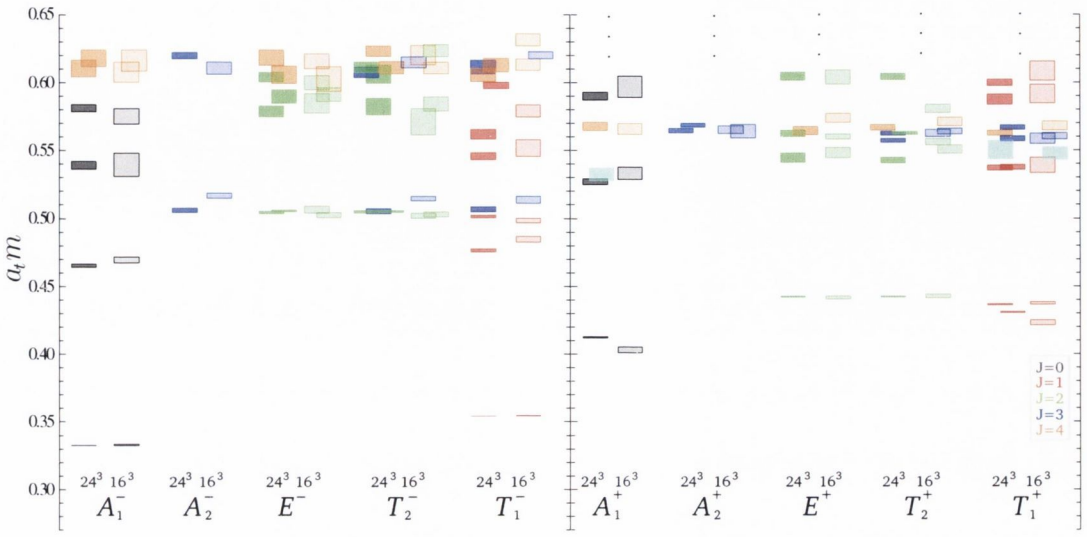

FIGURE 6.1: The extracted spectrum of states in the charm-light sector labelled by irrep Λ^P. For each irrep results from both the $24^3 \times 128$ and $16^3 \times 128$ volumes are shown side by side. The vertical size of each box gives the one sigma statistical uncertainty on either side of the mean and the box colour refers to the continuum spin assignment as described in the text. The light cyan boxes represent states that were not very well determined in the variational analysis; ellipses indicate that additional states may be present in these energy regions but were not robustly determined.

column represents the $16^3 \times 128$ volume. The size of the boxes represents the one-sigma statistical uncertainty. The colour scheme is as follows: states with $J = 0$ are coloured black, $J = 1$ are red, $J = 2$ are green, $J = 3$ are blue and $J = 4$ are orange. The light cyan boxes represent states that were not very well determined in the variational procedure but robust enough that a mass could be extracted. The ellipses in the positive parity sector of each figure represent regions where states may be present but were not robustly determined.

Components of $J \geq 2$ states are distributed across multiple irreps, and appear at masses that are degenerate up to discretisation effects. As in the charmonium sector, we generally see no significant discrepancies between these components in different

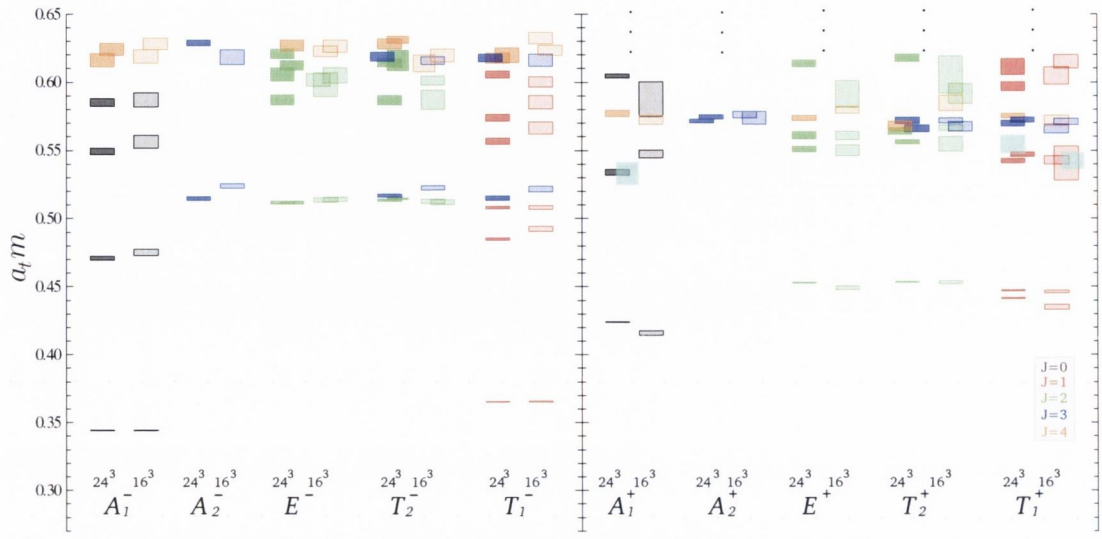

FIGURE 6.2: The extracted spectrum of states in the charm-strange sector labelled by irrep Λ^P. For each irrep results from both the $24^3 \times 128$ and $16^3 \times 128$ volumes are shown side by side. The vertical size of each box gives the one sigma statistical uncertainty on either side of the mean and the box colour refers to the continuum spin assignment as described in the text. The light cyan boxes represent states that were not very well determined in the variational analysis; ellipses indicate that additional states may be present in these energy regions but were not robustly determined.

irreps. As discussed in section 3.5, we match up states across irreps by comparing overlaps. It is clear that the dense spectra of states above $a_t m \sim 0.5$ would be impossible to disentangle without information other than just the masses, which again emphasises the importance of the spin identification scheme.

In general, throughout both spectra, we do not observe a significant volume dependence. However, there are some significant exceptions. For the lightest 0^+ and 1^+ states (in the A_1^+ and T_1^+ irreps respectively), which are determined with very high statistical precision, we observe a two-sigma difference between the two volumes. One explanation could be that because these states lie precariously close to thresholds, mixing with multi-hadron states may be important, and could cause the

observed volume dependence. As previously mentioned, our interpolator basis does not include any interpolators that *look-like* two-mesons, and so we do not expect to be able to reliably determine any multi-hadron energy levels; this suggests that a mass value is only accurate up to the hadronic width of the given state. In the charm-strange sector, these two states correspond to where we expect to see the enigmatic $D^*_{s0}(2317)^{\pm}$ and $D_{s1}(2460)^{\pm}$ levels, and interestingly, the experimental bound on their widths is quite small, $\Gamma \leq 4$ MeV [48]. With these possible exceptions, we see no clear evidence for the presence of multi-hadronic effects.

6.2 Final Spin Identified Charm-Light and Charm-Strange Spectra

In Figures 6.3 and 6.4, we show our final charm-light and charm-strange spectra; in each case we show the well determined spin identified spectra on our $24^3 \times 128$ volume, since calculations on this volume were computed with higher statistics, and on top of that, it is our largest volume, meaning that any finite volume effects will be less important. In these figures we show the calculated (experimental) masses with half of the calculated (experimental) η_c mass subtracted in order to reduce the systematic error from the setting of the bare charm quark mass. In Figure 6.3, the dashing corresponds to the lowest non-interacting $D\pi$ and $D_s\bar{K}$ threshold using our calculated values (coarse green dashing) and experimental values (fine black dashing). In Figure 6.3, the dashing corresponds to the lowest non-interacting DK threshold using our calculated values (coarse green dashing) and experimental values (fine black dashing). The mass values presented in these figures are shown in Tables A.2 and A.3.

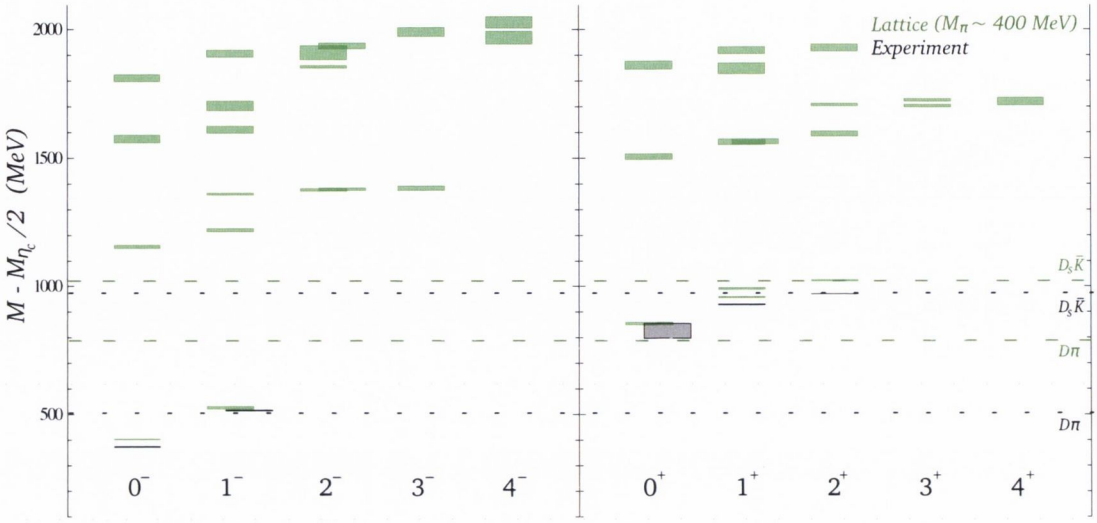

FIGURE 6.3: The charm-light spectrum up to around 3.8 GeV labelled by J^P. The green boxes are our well determined calculated masses on these ensembles with $M_\pi \sim 400$ MeV, while the black boxes correspond to experimental masses of neutral charm-light mesons from the PDG summary tables [48]. We present the calculated (experimental) masses with half the calculated (experimental) η_c mass subtracted to reduce the uncertainty from tuning the bare charm-quark mass. The vertical size of each box indicates the one sigma statistical uncertainty on either side of the mean. The dashed lines show the lowest non-interacting $D\pi$ and $D_s\bar{K}$ thresholds using our measured masses (coarse green dashing) and experimental masses (fine black dashing).

Many other studies of open-charm spectra have taken place in the lattice community. Most of these have focused on only the lowest lying S and P-wave states. Examples of these studies can be found in [92–94]. Only recently have calculations begun to explore states higher up in the spectrum. In [85, 87], the authors present preliminary results on $N_f = 2+1$ dynamical ensembles at the $SU(3)$ point. They calculate states with $J^P \leq 3$. However, the treatment of the strange quark is quite different from our approach and $M_\pi = M_K = 442$ MeV, making it difficult to compare the results with ours.

In [95], results are presented from calculations on $N_f = 2 + 1$ ensembles for a range

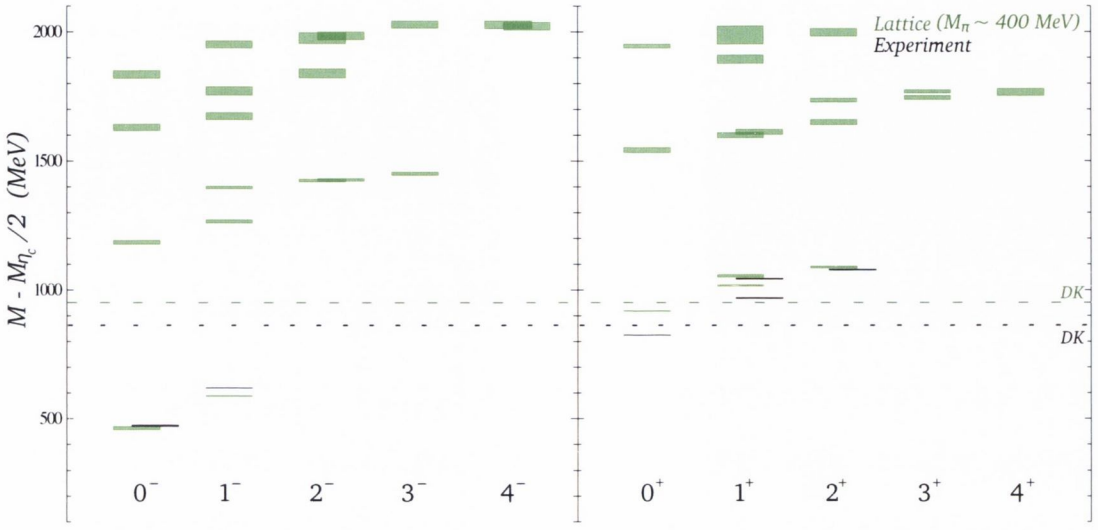

FIGURE 6.4: The charm-strange spectrum up to around 3.8 GeV labelled by J^P. The green boxes are our well determined calculated masses on these ensembles with $M_\pi \sim 400$ MeV, while the black boxes correspond to experimental masses of neutral charm-strange mesons from the PDG summary tables [48]. We present the calculated (experimental) masses with half the calculated (experimental) η_c mass subtracted to reduce the uncertainty from tuning the bare charm-quark mass. The vertical size of each box indicates the one sigma statistical uncertainty on either side of the mean. The dashed lines show the lowest non-interacting $D\pi$ and $D_s\bar{K}$ thresholds using our measured masses (coarse green dashing) and experimental masses (fine black dashing)

of pion masses from 702 MeV down to 156 MeV. Here the focus is mainly on the S and P-wave states, although the first excited multiplet in S-wave of D_s mesons is also presented. In this study they use the Fermi-lab method for the charm quark [56]. In [96], the same authors present results from a $N_f = 2$ calculation of the charm-light spectrum on a single volume with $M_\pi = 266$ MeV, again using the Fermi-lab method for the charm quark, and this time using the distillation method of quark smearing. The lowest lying $0^\pm, 1^\pm$ and $2^\pm$ states are obtained along with some excited 0^- and 1^- states. They also investigate the lowest-lying resonances in the 0^+ and 1^+ channels.

In all of these other studies the interpolator basis is significantly smaller than the basis that we employ; they do not include a wide range of spatial structures and not all of the relevant irreps were considered. Another improvement we have made in this study is the inclusion of interpolators proportional to the field strength tensor, allowing access to gluonic degrees of freedom.

6.3 Interpretation of Open-Charm Spectra

In this section we give an interpretation of our extracted charm-light and charm-strange spectra. As previously mentioned, we show our final results in Figures 6.3 and 6.4. In both spectra we observe that most states appear to fit into the $n^{2S+1}L_J$ pattern expected by quark models. As discussed for the charmonium spectrum, operator-state overlaps, Z, are used to identify the structure of extracted states and make $n^{2S+1}L_J$ assignments.

In the negative parity sector of both spectra we observe a ground state S-wave pair $[0^-, 1^-]$. We find the first excitation of this set around 700 MeV higher. At $M - M_{\eta_c}/2 \sim 1400$ MeV we find a full D-wave set $[(1,2,3)^-, 2^-]$ and the second excitation of the S-wave set around $M - M_{\eta_c}/2 \sim 1900$ MeV. Around $M - M_{\eta_c}/2 \sim 2000$ MeV we see states that appear to be parts of an excited D-wave set and parts of a G-wave set, $[(3,4,5)^-, 4^-]$. Like in the charmonium sector, we do not see the full G-wave compliment due to the lack of four derivative interpolators. We interpret the apparent supernumerary states as hybrid mesons, but delay their discussion until chapter 7.

In the positive parity sector of the charm-light spectrum we find a full P-wave set, $[(0,1,2)^+, 1^+]$, sitting around the $D_s\bar{K}$ threshold, and in the charm-strange spectrum

we observe the same set around the DK threshold. Around 600 MeV higher in each spectrum, we observe the first P-wave excitation, and at $M - M_{\eta_c}/2 \sim 1700$ MeV we see a full F-wave set, $[(2,3,4)^+, 3^+]$. The four states around $M - M_{\eta_c}/2 \sim 1900$ MeV in both spectra we interpret as hybrid mesons, and discuss them in chapter 7.

Our interpretation has been given in terms of non-relativistic quark model supermultiplets, but in the heavy-quark (static) limit, where $m_l < m_s \ll m_c$, one can classify states in a different fashion since the spin of the heavy-quark decouples from the system. In this picture, the total angular momentum, j, of the light degrees of freedom is $j = L \otimes s_q$, where $s_q = 1/2$ is the spin of the light quark. For non-zero angular momentum, the total angular momentum can take two values $j = |L \pm 1/2|$. Now, coupling in the spin of the heavy quark produces multiplets that consist of degenerate doublets. For example, in S-wave there is one doublet with $j^P = [(0,1)^-]$, and in P-wave there are two doublets, $j^P = [(0,1)^+]$ and $[(1,2)^+]$. The heavy-quark limit is discussed further in the context of mixing between spin-singlet and spin-triplet states section 6.5. Even though the charm quark is significantly heavier than the light and strange quarks, we do not expect it to be heavy enough for this limit to apply rigorously, although it can provide a useful guide. This is observed in both spectra, where, for example, the 0^- and 1^- S-wave states are not degenerate.

6.4 Comparison with Experiment

We now compare our extracted spectra to the current experimental situation in the open-charm sector. We show the experimentally confirmed states as black boxes, taken from the PDG [48], in Figures 6.3 and 6.4, where the size of the boxes signifies the uncertainty in the experimental determination. It is clear that in general we see

good qualitative agreement between our extracted states and the experimental ones, but some some comments on the quantitative differences are required.

Firstly, it is important to note that, because we do not include multi-hadron states, our determinations are only accurate up to the hadronic width of a given state. We also have unphysically light quarks, which adds to the systematic uncertainty, but below threshold we do not expect these effects to be important in the charm-strange sector, but near or above thresholds involving mesons containing light quarks, this this could be important.

As discussed in section 4.3, we significantly undershoot the S-wave hyperfine splitting in both the charm-light and charm-strange sectors. We argued that this discrepancy is due to the use of a tree-level tadpole-improved value for the spatial clover coefficient, and our subsequent tests allowed us to assign an approximate value of 20 MeV to our leading $O(a_s)$ systematic uncertainty. In the charm-light spectra, we find our P-wave states higher than their experimental counterparts, which may be due to the unphysically heavy light quarks.

In the charm-strange spectrum, two of our P-wave states are consistent with experiment, but the other two states, expected to correspond to the enigmatic $D^*_{s0}(2317)^{\pm}$ and $D_{s1}(2460)^{\pm}$, are significantly higher than their experimental counterparts. It is important to note that the 0^+ and 1^+ are very close to, respectively, the DK and D^*K thresholds. It is also worth noting that the calculated and experimental 0^+ states lie the same distance from their appropriate thresholds. This may suggest that the unphysically heavy light quarks are responsible for the discrepancy. However, due to the interaction with the threshold, further study is required with multi-hadron interpolators included.

6.5 Mixing of Spin-Singlet and Spin-Triplet States

In this section we discuss the mixing between spin-singlet and spin-triplet states in both the charm-light and charm-strange sectors. Since the charm quark is significantly heavier than the light or strange quarks, $SU(4)$ symmetry is badly broken in QCD. Therefore charm-light and charm-strange mesons are not eigenstates of charge conjugation, or any generalisation of it. It is the absence of such a symmetry that allows mixing between spin-singlet ($^1L_{J=L}$) and spin-triplet ($^3L_{J=L}$) states. A probe of this mixing may help us quantify flavour symmetry breaking.

Using a two-state hypothesis and assuming energy independent mixing, an expansion can be made for states A and B in terms of a spin-singlet and triplet basis. *Choosing* $|B\rangle$ to be the heavier state gives

$$|A\rangle = +\cos(\theta)|^1L_{J=L}\rangle + \sin(\theta)|^3L_{J=L}\rangle \ , \tag{6.1}$$

$$|B\rangle = -\sin(\theta)|^1L_{J=L}\rangle + \cos(\theta)|^3L_{J=L}\rangle \ . \tag{6.2}$$

Within our basis, the interpolators $\left[(\rho-\rho_2)\times D_L^{[L]}\right]_{J=L}$ and $\left[\{\pi,\pi_2\}\times D_L^{[L]}\right]_{J=L}$ only overlap onto the states $^3L_{J=L}$ and $^1L_{J=L}$ respectively in the non-relativistic limit. There are analogous interpolators, $\left[(\rho-\rho_2)\times D_1^{[2]}\right]_{J=1}$ and $\left[\{\pi,\pi_2\}\times D_1^{[2]}\right]_{J=1}$, which overlap onto the spin-singlet and spin-triplet hybrids.

To determine the mixing angle, θ, we take the ratio of the overlap factor of one of the aforementioned interpolators for state A to the overlap factor for state B, with the ratio giving either $\tan(\theta)$ or $\cot(\theta)$ depending on the interpolator used.

We extract mixing angles for the lightest pair of P-wave, 1^+, and D-wave, 2^-, and hybrid, 1^- states. These are shown in Table 6.1 for each of the aforementioned interpolators. θ_{c-l} refers to the mixing angle in the charm-light sector and θ_{c-s}

	J^P	$\|\theta\|/^\circ$			
		$\sim (\rho - \rho_2)$	$\sim \pi$	$\sim \pi_2$	Heavy-quark limit
c-l	1^+	60.1(0.4)	62.6(0.2)	65.4(0.2)	54.7 or 35.3
	2^-	26.7(2.2)	22.2(3.7)	18.9(3.9)	50.8 or 39.2
	1^- (hybrid)	59.7(1.1)	68.4(0.8)	67.4(0.9)	
c-s	1^+	60.9(0.6)	64.9(0.2)	66.4(0.4)	54.7 or 35.3
	2^-	64.9(1.9)	68.7(2.0)	70.9(1.8)	50.8 or 39.2
	1^- (hybrid)	59.9(1.7)	67.9(0.9)	67.3(0.9)	

TABLE 6.1: The absolute value of the mixing angles for the lightest pairs of 1^+, 2^- and hybrid 1^- states in the charm-light (c-l) and charm-strange (c-s) sectors. The angles extracted using different operators are presented; these are labelled by the gamma matrix structure with the derivative structures described in the text. Also shown are the mixing angles expected in the heavy-quark limit. The apparent difference between the charm-light and charm-strange 2^- mixing angles is explained in the text.

the mixing angle in the charm-strange sector. The overall sign of a given mixing angle is not observable in our calculation, and we thus show their absolute values. For each pair of states, the variation between mixing angles determined using the three different operators gives an idea of the size of the systematic uncertainties. As well as the usual systematics, included are systematics arising from our rather simplistic assumptions of a two-state hypothesis with energy-independent mixing, and from assuming that the energy difference between the relevant states is small enough such that the renormalisation factors for the different interpolators do not vary substationally over this energy range. The relatively large variation in the 1^- hybrid mixing angles is to be expected since the assumptions are less justified due to the states lying higher up in the spectrum and there is a relatively large mass gap between the pair of relevant 1^- states. Also shown in Table 6.1 are the mixing angles as calculated in the heavy-quark limit [50].

The P-wave and hybrid mixing angles are similar for both the charm-light and charm-strange sectors, but for the D-wave they appear to be drastically different.

This is because the dominantly ${}^3D_2$ state and the dominantly ${}^1D_2$ state are almost degenerate, and for the charm-strange states, the mass ordering is flipped compared to the charm-light states. This means that $\theta_{c-s} \approx 90 - \theta_{c-l}$.

Our strange quark mass is close to the physical value but the light quarks are unphysically heavy, resulting in M_K/M_π being close to unity. Therefore $SU(3)$ flavour symmetry is not badly broken and we expect to find similar mixing angles in each flavour sector. Hence, the mixing angles in the charm-strange sector should be closer to their physical values.

All of our mixing angles lie between zero mixing, which corresponds to the flavour symmetry limit, and the heavy-quark limit values; this is expected since the charm quark lies at an intermediate scale, larger than the light quarks, but not heavy enough so that the heavy-quark limit applies. Our results are qualitatively consistent with other studies [49, 97–101], that in general, find significant mixing between the spin-singlet and spin-triplet states with, at least for the lightest 1^+ pair, some deviation from the heavy quark limit.

Chapter 7

Exotic and Hybrid Mesons

In this section we now discuss the apparent supernumerary states that appear in Figures 5.3, 6.3 and 6.4. We interpret these states as hybrid mesons and discuss their appearance in the charmonium, charm-light and charm-strange spectra as well as discuss a suggested phenomenology by comparing to previous studies of hybrid mesons.

7.1 Exotic and Hybrid Charmonium Mesons

Figure 7.1 shows the charmonium spectrum calculated on our $24^3 \times 128$ volume, for J^{PC} channels in which we identify candidates for hybrid mesons. We define a hybrid candidate as any given state with a relatively large overlap onto an interpolator that is proportional to the commutator of two covariant derivatives, that is, the field strength tensor.

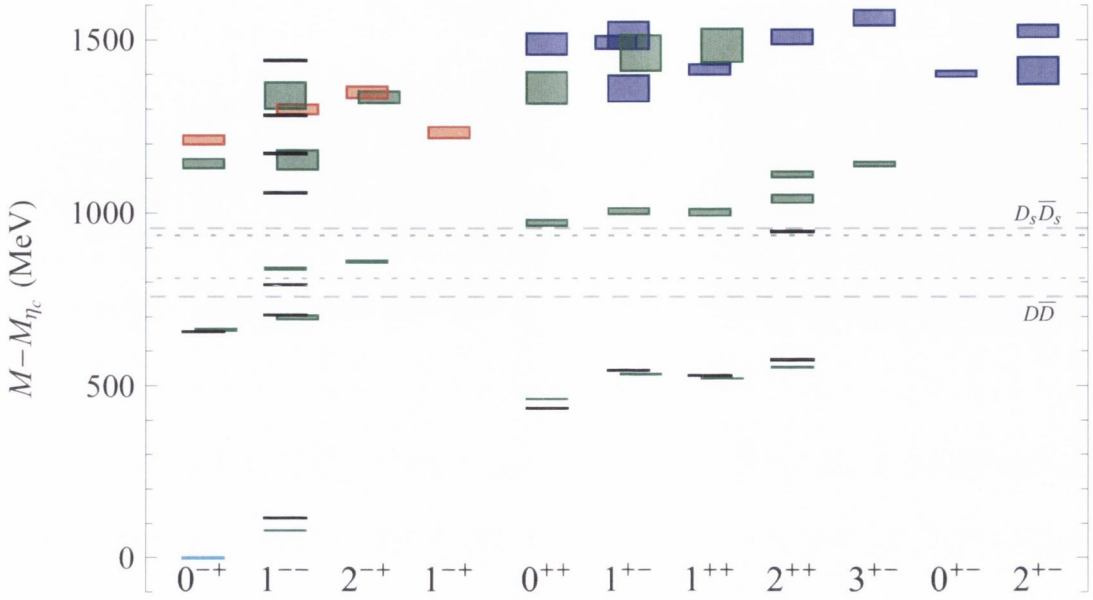

FIGURE 7.1: Charmonium spectrum calculated on our $24^3 \times 128$ volume, up to around 4.5 GeV showing only J^{PC} channels in which we identify candidates for hybrid mesons. Red (dark blue) boxes are states suggested to be members of the lightest (first excited) hybrid supermultiplet as described in the text and green boxes are other states. Black lines are experimental values and the dashed lines indicate the lowest non-interacting $D\bar{D}$ and $D_s\bar{D}_s$ thresholds.

We observe that the lightest exotic meson, that has $J^{PC} = 1^{-+}$, is almost degenerate with three states observed in the negative parity sector. These three states are suggested to be non-exotic hybrids, $(0, 2)^{-+}, 1^{--}$. Higher in mass, we observe two further mesons with exotic quantum numbers, namely the $(0, 2)^{+-}$ states. We also observe another 2^{+-} state slightly higher in mass. Above the range shown in our plots, we find a possible excitation of the 1^{-+} state at ~ 4.6 GeV. We observe an exotic 3^{-+} state around 4.8 GeV, while the lightest 0^{--} exotic does not appear until above 5 GeV.

Our consideration of hybrid mesons becomes more interesting by the observation that there are four almost degenerate candidate hybrids, with $J^{PC} = [(0, 1, 2)^{-+}, 1^{--}]$.

These states are coloured red in Figure 7.1; this is the pattern of states expected to appear in the lightest hybrid supermultiplet of the MIT Bag Model [102], and also in the P-wave quasi-gluon approach [103], which is where a quark-antiquark pair in S-wave is coupled to a colour octet P-wave 1^{+-} gluonic excitation. The lightest two supermultiplet structures expected in this approach are shown in Table 5.1. It is also interesting to note that the pattern of the lightest set of four hybrids is not what is expected from the flux-tube or the S-wave quasi-gluon models, and the appearance of two 2^{+-} states, with one slightly higher in mass than the other, seems to rule out the flux-tube model altogether, as it does not predict two states so close in mass. The pattern of J^{PC} of the lightest hybrids is the same as that found in previous studies of the light meson sector [104]. Furthermore, they appear at a very similar mass scale to those in the light meson sector, that is, at $\sim 1.2 - 1.3$ GeV above the ground state meson of the system.

Thus far, we have claimed that the lightest four hybrid states belong to the same supermultiplet, but we have, so far, only based this on considerations of their masses. To strengthen our claim, we follow [104], and consider the interpolator-state overlaps in more detail. As discussed in [104], the interpolators $(\rho_{NR} \times D^{[2]}_{J=1})^{J=0,1,2}$, which have $J^{PC} = (0,1,2)^{-+}$ have the structure of a colour-octet quark-antiquark pair in S-wave with $S = 1$, coupled to an excited chromomagnetic field with $J_g^{P_g C_g} = 1^{+-}$. Here g represents that the quantum numbers in question are for the gluonic excitation. The interpolator $(\pi_{NR} \times D^{[2]}_{J=1})^{J=1}$, with $J^{PC} = 1^{--}$ has the same structure except that $S = 0$. Figure 7.2 shows that the four candidate states for the lightest Charmonium hybrid supermultiplet have large overlap onto the previously discussed interpolators. As previously discussed, it is expected that the Z values for each of these interpolators will be similar for states of a given supermultiplet, since the structure of the interpolators are essentially the same. Figure 7.2 shows that each of these interpolator-state overlaps are equal in value within statistical precision. This

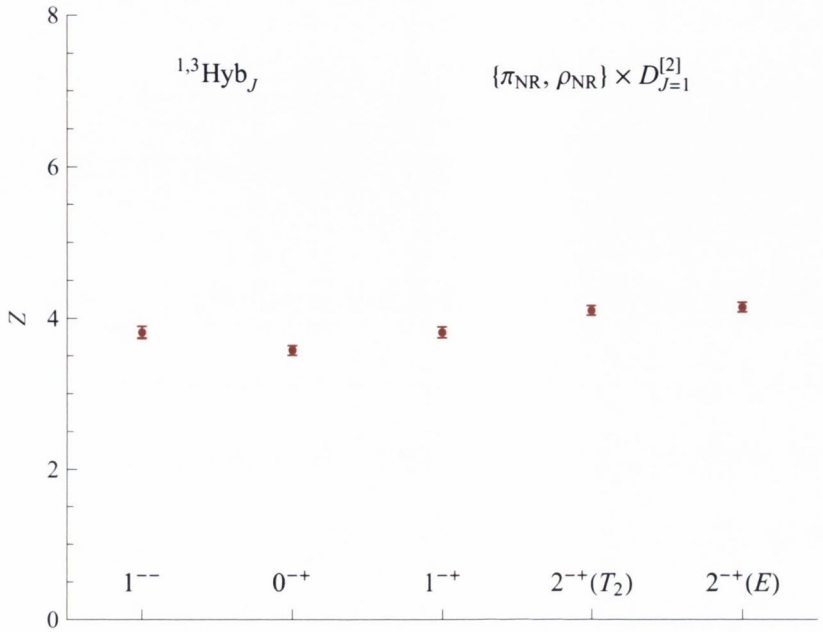

FIGURE 7.2: Overlaps, Z, for the proposed lightest charmonium hybrid supermultiplet with interpolators $\{\pi, \rho\}_{\mathrm{NR}} \times D^{[2]}_{J=1}$.

is further evidence that these states reside within the same supermultiplet, which has a structure of S-wave quark-antiquark coupled to a gluonic excitation with 1^{+-}.

In Figure 7.1, we also point out a set of ten hybrid candidates coloured in blue. If one continues to consider the P-wave quasi-gluon approach, it is expected that the first excited hybrid supermultiplet will appear from P-wave colour-octet quark-antiquark pairs coupled to a 1^{+-} gluonic excitation, giving rise to the set $[0^{+-}, (1^{+-})^3, (2^{+-})^2, 3^{+-}, (0,1,2)^{++}]$, as shown in Table 5.1. The blue coloured hybrid candidates shown in Figure 7.1 appear to match this pattern. Interestingly, this pattern was observed in [104] for the light meson sector, and the consistency between the two sectors may suggest a common phenomenology is emerging.

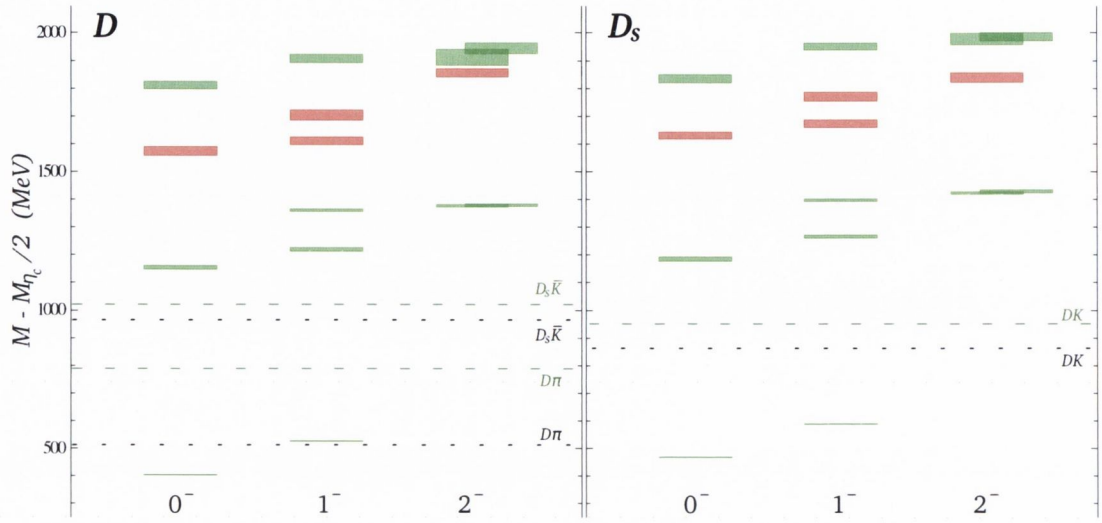

FIGURE 7.3: The negative-parity charm-light (left panel) and charm-strange (right panel) meson spectra showing only channels where we identify hybrid candidates. The red boxes are identified as states belonging to the lightest hybrid supermultiplet as discussed in the text, while the green state show conventional charm-light and charm-strange mesons.

It is worth noting that the inclusion of multi-hadron interpolators could modify the interpretation of states above the open-charm threshold.

7.2 Open-Charm Hybrids

We now move to discuss the apparent supernumerary states in Figures 6.3 and 6.4. We interpret these states as hybrid mesons due to their relatively large overlap with interpolators proportional to the commutator of two covariant derivatives. In Figure 7.3 we highlight these states in red.

As in the charmonium sector, we interpret the four states, $[(0,1,1,2)^-]$, as belonging to the lightest hybrid supermultiplet. As explained earlier, states belonging to the

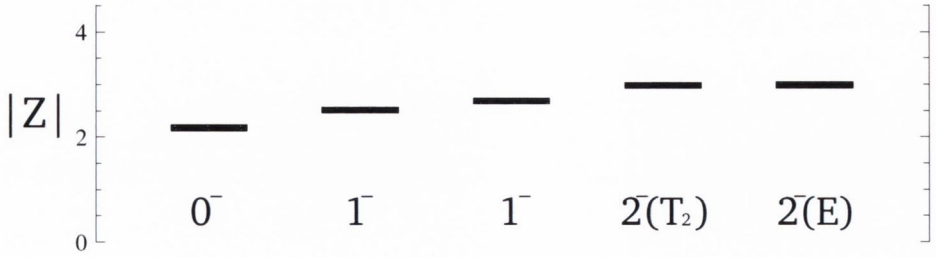

FIGURE 7.4: Overlaps, Z, of the charm-strange states proposed to be members of the lightest hybrid supermultiplet with interpolators that are proportional to the field strength tensor, $\left[\{\pi,\rho\} \times D^{[2]}_{J=1}\right]_J$ subduced into the relevant irreps.

same supermultiplet are expected to have similar interpolator-state overlap values. In Figure 7.4 we show overlaps for the four candidate hybrid states in the charm-strange sector, with interpolators $\left[\pi \times D^{[2]}_{J=1}\right]^J$ and $\left[\rho \times D^{[2]}_{J=1}\right]^J$. As discussed in section 6.5, the two 1^- hybrids are mixtures of spin-singlet and spin-triplet basis states, so they overlap with both the $\left[\pi \times D^{[2]}_{J=1}\right]$ and $\left[\rho \times D^{[2]}_{J=1}\right]$ interpolators. Therefore, for these states we plot $\sqrt{Z_\pi^2 + Z_\rho^2}$, where Z_π and Z_ρ are the overlaps with these two different interpolators. From Figure 7.4 it is clear that the four states have very similar overlap values, suggesting that they have a common structure, which is clear evidence for identifying these four states as members of the lightest hybrid supermultiplet. As in the charmonium sector, the pattern of these four hybrid states can be explained via the P-wave quasi-gluon picture; an S-wave quark-antiquark pair coupled to a 1^{+-} gluonic excitation.

In both the charmonium and light meson [104] sectors, the first excited hybrid supermultiplet is identified. In both the charm-light and charm-strange sectors, we find candidate positive parity hybrid mesons at ~ 1.5 GeV above the respective ground states. Four of these states are shown in the positive parity sectors of Figures 6.3 and 6.4, but because we do not robustly identify all states in that energy region, we can not observe the full set of states in the first excited hybrid supermultiplet.

Chapter 8

Scattering on the Lattice

In this chapter, we turn our attention to scattering on the lattice. We firstly present the problems that scattering processes present to the lattice practitioner, before moving on to discuss the formalism that has allowed (at least some) scattering calculations to be performed in the framework of lattice field theory. We then discuss our implementation of this framework, and finally, we present a preliminary calculation of $D\pi$ scattering in the isospin, $I = 3/2$, channel, and map out the corresponding phase shift, δ_0, which considers only the $l = 0$ partial wave in the A_1 irrep.

The scattering matrix, S, is a map between in and out asymptotic states of a given scattering process. When one assumes asymptotic completeness, that is, that every state has in and out asymptotes, S becomes unitary. All possible states in a given physical system (i.e. in its Hilbert space) can be thought of as either bound states or scattering states. Non-relativistically, bound states appear as poles in the S-matrix in the upper half of the complex momentum plane, while resonances appear as poles in the lower half. An important quantity that is related to the scattering matrix is

known as the *phase shift* $\delta_l(E)$, which is given by

$$S_l(E) = e^{2i\delta_l(E)} \,, \tag{8.1}$$

where l is known as the *partial wave*, which labels the angular momentum of the in going state. The scattering phase shift $\delta_l(E)$ measures the shift in the phase of a scattering wave of a given angular momentum l, as it passes through some potential. It can be written as $\delta(E) = \delta_{bg}(E) + \delta_{res}(E)$ [105], where $\delta_{bg}(E)$ is the part of the phase shift due to direct scattering between the particles without an intermediate resonance being formed. The part entirely due to the formation of the resonance is encoded within $\delta_{res}(E)$. For narrow resonances, it takes the form

$$\delta_{res}(E) = \tan^{-1}\left(\frac{\Gamma}{E_{res} - E}\right) \,, \tag{8.2}$$

showing that the phase shift will vary rapidly by π when the centre of mass energy, E, is close to the energy of the resonance, E_{res}.

In relativistic field theory, the S-matrix is related to the residue of on-shell correlation functions via the LSZ reduction formula. Resonances can then be found as a pole in the correlation function on the second Riemann sheet. One can then derive the relativistic analogue of (8.2) [105],

$$\delta_{res}(E) = \tan^{-1}\left(\frac{m_{res}\Gamma}{m_{res}^2 - E^2}\right) \,, \tag{8.3}$$

where m_{res} is the mass of the resonance.

In this study, calculations are performed within a finite volume of discretised Euclidean space-time. The finite volume has dramatic effects on the Källên-Lehmann

spectral function

$$\Delta(p) = \int_0^\infty d\mu^2 \rho(\mu^2) \frac{1}{p^2 - \mu^2} \,. \tag{8.4}$$

The values of momenta allowed in a finite volume discretises the spectrum, hence transforming the multi-particle branch cut into a series of isolated poles; the spectral function becomes meromorphic and contains no branch cuts. Since resonances are poles on the second Riemann sheet, the finite volume effectively removes them, rendering all would be resonances stable.

Another fundamental difficulty in extracting scattering information, is due to the use of Euclidean space-time. The Maiani-Testa theorem [106] shows the impossibility of directly extracting scattering information from Euclidean three-point (or higher) correlation functions; the form factor of the three-point function loses its complex phase when Wick rotated, and in Minkowski space it is this complex phase that contains the scattering information. With the Maiani-Testa theorem ruling out direct access to scattering information in lattice field theory, indirect methods have appeared. These are based upon the idea that the resonances, having merged with the rest of the spectrum, will have some effect on the spectrum of the theory in a finite volume. The method used in this study has become commonly known as Lüscher's method [77, 107–110], and will be the subject of the following section. For a comparison between alternate methods and Lüscher's method, and a nice discussion of resonances and scattering theory see [105].

8.1 The Lüscher Method

The Lüscher method was derived over a series of five papers [77, 107, 108, 108, 109], which will now be summarised briefly. For a more detailed review of these papers

see [105].

In [107], the effect of a finite volume on single particle states is discussed. Here it was found that the mass shift, due to the finite volume, of a single particle state is related to the forward scattering amplitude. Lüscher also showed that the entire difference between the finite volume and infinite volume cases is due to so-called *around the world propagators*. Furthermore, his estimations show that only Feynman diagrams with one around the world propagator contribute significantly to the finite volume mass shift, and are of order $e^{-\frac{\sqrt{3}}{2}mL}$, where L is the extent of the lattice and m is the mass of the state in question.

In [108], the emphasis shifts to that of scattering states. The results obtained from this paper only apply to two-particle scattering states. It was found that the finite volume effects scattering states in two ways. The first being that around the world propagators cause a shift in the mass in the same way as for single particle states, and the second was that the interaction between the two scattering particles also causes a shift in the mass. It is this second effect that is related to resonances. It is clear that we require the second effect to be dominant in order to maximise the chances of extracting resonance parameters from these mass shifts, as they are expected to be small. In order to safely neglect the effect due to around the world propagation, relatively large lattice extents, L, must be used.

In the remaining three papers of the series [77, 109, 110], what is now commonly known as Lüscher's formula is derived. Firstly this formula is derived in two-dimensions where it is easier to understand. A brief sketch of this derivation is as follows. In $1+1$ non-relativistic quantum mechanics the two-particle wave function is $\psi(r)$, where r is the relative coordinate between the two particles. Due to the finite volume, the phase of this wave function is altered in two ways. The first being the shift due to motion through the finite volume, which in momentum space will be

e^{ipL}. The second is the shift due to the inter-particle potential. These result in the scattering phase shift $e^{2i\delta(p)}$. Now, imposing periodic boundary conditions requires the total phase shift across the volume to vanish, leading us to the two dimensional version of the Lüscher formula

$$e^{ipL} = e^{2i\delta(p)} \ . \tag{8.5}$$

Since one can determine the energy spectrum of the theory numerically on the lattice, this formula allows one to map out the previously inaccessible phase shift. Obviously this formula is not applicable in any useful cases since it is two-dimensional, but it was pioneering in the sense that it showed that a link between lattice observables and the infinite volume phase shift existed.

Using a similar idea, the four-dimensional Lüscher formula was subsequently derived. Again this was derived in the context of non-relativistic quantum mechanics, but this time Lüscher constructed a map so that the quantum mechanical result can be carried over to field theory under some special circumstances, with one such restriction being that the energy of the system in question be below the relevant inelastic threshold. A brief outline of the derivation is as follows. Consider a finite volume where the extent of the finite volume is larger than the range of the inter-particle potential. Denote the region outside of the potential as R. In this region, the Schrödinger equation takes the same form as the infinite volume case. The radial wave function obtained from this equation will also be a solution to the Helmholtz equation,

$$(\Delta + p^2)\psi(r) = 0 \ . \tag{8.6}$$

The point is that any eigenfunction of the Hamiltonian will have two asymptotic forms within the region R; one arising from the Schrödinger equation and the

other from the Helmholtz equation. Matching these two forms leads to the four-dimensional Lüscher formalism.

Since this derivation is in non-relativistic quantum mechanics, the result still needed to be mapped to the field theory case. This is done using the Bethe-Salpeter kernel in [110], resulting in a formalism that can be applied to field theory.

The Lüscher formalism is neatly expressed via the following equation,

$$\det\ [e^{2i\delta_l(p)} - U(p)] = 0\ , \tag{8.7}$$

where

$$U(p) = \frac{M(p) + i}{M(p) - i}\ , \tag{8.8}$$

is a matrix of known functions [110]. The operator $M(p)$ commutes with the rotation operator of the cubic group, and can thus be block diagonalised, so that each block only acts on a specific irreducible representation of the cubic group.

Until recently in [61], most calculations using the Lüscher formalism were performed in the A_1 irrep, only considering the $l = 0$ partial wave, therefore neglecting the effects of higher partial waves. In this scenario, taking the positive parity case as an example, the matrix equation (8.7), is reduced to a one dimensional form

$$e^{2i\delta_0} = U(A_1^+) = \frac{M_{00,00} + i}{M_{00,00} - i}\ , \tag{8.9}$$

where

$$M_{00,00} = \frac{Z(1; q^2)}{\pi^{3/2} q}\ . \tag{8.10}$$

$Z(1;q^2)$ is known as the *Lüscher zeta function* and is given by

$$Z_{js}(1;q^2) = \sum_{\vec{n}\in\mathbb{Z}^3} \frac{r^j Y_{js}(\theta,\phi)}{(\vec{n}^2 - q^2)^2} \ , \tag{8.11}$$

where $Y_{lm}(\theta,\phi)$ are spherical harmonics and $q = pL/2\pi$. It is more instructive to consider equation (8.9) in the following form

$$\delta(p) = -\phi(q) + \pi n \ , \tag{8.12}$$

where

$$\tan(\phi(q)) = \left[\frac{\pi^{3/2} q}{Z_{00}(1;q^2)}\right] \ . \tag{8.13}$$

The major restriction of this formalism is that it is only valid for elastic scattering of the type $2 \to 2$. This restriction is in place for a number of reasons. The most obvious of these being due to the construction of the formalism in non-relativistic quantum mechanics; inelastic scattering of type $A \to B$ can not be accommodated in such a set up. This is very restrictive when attempting to map out the phase shift due to the extremely limited number of states lying below inelastic thresholds at zero momentum.

In order to somewhat circumvent this problem, the Lüscher formalism has been extended to include moving frames [111, 112]. This extension presents the opportunity to include states with non-zero momentum, helping to increase the number of energy levels below inelastic threshold for mapping out the phase shift. The Lorentz boost from the lab frame to the center of mass frame in effect *deforms* the cubic volume, and only some subgroup of the original cubic symmetry group remains. Practically,

this results in a change to the matrix $M(p)$. It becomes

$$M^{\mathbf{d}}_{lm,l'm'}(p) = \gamma^{-1}\frac{(-1)^l}{\pi^{3/2}} \sum_{j=|l-l'|}^{l+l'} \sum_{s=-j}^{j} \frac{i^j}{q^{j+1}} Z^{\mathbf{d}}_{js}(1;q^2) C_{lm,js,l'm'}\ , \tag{8.14}$$

where the *generalised Lüscher zeta function*, $Z^{\mathbf{d}}_{js}(1;q^2)$, is given by

$$Z^{\mathbf{d}}_{lm}(s;q^2) = \sum_{\vec{r}\in P_d} Y_{lm}(\vec{r})(\vec{r}^2 - q^2)^s. \tag{8.15}$$

Here the summation is over the set $P_d = \{\vec{r} \in \mathbb{R}^3 : \vec{r} = \vec{\gamma}^{-1}(\vec{n} + \frac{\vec{d}}{2})\}$. When $\vec{d} = 0$, the lab and center of mass frames coincide ($\gamma = 1$, $P_d = \mathbb{Z}^3$), and equations (8.14) and (8.15) revert to their standard non-boosted forms. For more on this extended set up, see [111, 112].

More recently, further generalisations of the Lüscher formalism have emerged. For example, in [113] they derive a generalised non-relativistic version of the Lüscher formula which includes three particle inelastic channels, while there are ongoing efforts directed towards a multiple-channel generalisation of the Lüscher formula [114, 115].

This concludes our brief introduction of scattering on the lattice, the Lüscher formalism and its extension to moving frames. We will now move to discuss our implementation of these methods for the case of $D\pi$ scattering, beginning with a description of our construction of multi-hadron interpolators.

8.1.1 Multi-Hadron Interpolators

As previously explained, the Lüscher formalism gives a way of extracting scattering information on the lattice, which is calculated from the shift in the energy level of a given state, compared to its non-interacting counterpart. Since these shifts are expected to be very small, one requires interpolating fields that efficiently describe the required multi-hadron state, otherwise, the shift could be drastically miscalculated due to contamination from other states, or in the worst case, lost in the statistical variance. In general, a multi-hadron interpolator can be constructed from the product of two single hadron interpolators $A^\dagger(\vec{k})$ and $B^\dagger(\vec{k})$ via

$$(AB)^{\dagger[\vec{k}_1,\vec{k}_2]}_{\vec{P},\Lambda,\mu} = \sum_{\substack{\vec{k}_i \in \{\vec{k}_i\}^* \\ \vec{k}_1+\vec{k}_2=\vec{P}}} C(\vec{P},\Lambda,\mu;\vec{k}_1,\Lambda_1,\mu_1;\vec{k}_2,\Lambda_2,\mu_2) A^\dagger_{\Lambda_1,\mu_1}(\vec{k}_1) B^\dagger_{\Lambda_2,\mu_2}(\vec{k}_2) \ , \quad (8.16)$$

where C is the Clebsch-Gordan coefficient for $\Lambda_1 \otimes \Lambda_2 \to \Lambda$, and μ is the row of the corresponding irrep. The overall momentum of the state, $\vec{P}$, is given by the sum of the two individual momenta $\vec{k}_1 + \vec{k}_2$. The sum over $\vec{k}_i$ is a sum over all of the momenta in the star of $\vec{k}_i$, that is, all the momenta related to $\vec{k}_i$ by an allowed lattice rotation. A range of relevant Clebsch-Gordan coefficients, C, are listed in [61], where this construction is discussed in greater detail.

One problem encountered when computing multi-hadron two-point functions is that the interpolator used to describe the state AB may have significant overlap with excited states AB^*. Of course, excited state contributions to the correlator will die away quicker than the ground state, but even at modest times the excited state can be present to some degree, and the effective mass plateau will be pushed out to longer times where the effects of finite temporal extent can be felt. As suggested in [61], one solution to this problem is to form so-called *optimised interpolators*. The

strategy is as follows; using the large basis of interpolators discussed in chapter 3, one can construct an optimised single A interpolator by variationally diagonalising a matrix of single-hadron correlation functions. One then takes, as the optimised interpolator used to describe meson A, a linear combination of the single-hadron interpolators with weights chosen according to the significance of their coupling to the state A. One can then build a multi-hadron interpolator that will be dominantly AB from the optimised A and B interpolators. As shown in [61], for the case of the pion, the optimised pion interpolator does indeed force the effective mass to plateau at much earlier times, hence reducing the contamination from excited states and the finite temporal extent.

In our calculation of the $D\pi$ spectrum, we use overall momenta $\vec{P} = [0,0,0]$, $[0,0,1]$, $[0,1,1]$ and $[1,1,1]$. The various combinations of $\vec{k}_1$ and $\vec{k}_2$ that produce these momenta are shown in Table 8.1. The single hadron interpolators, used to construct the optimised two-hadron interpolators, that have momentum $\vec{k} = [0,0,0]$, are those of section 3.3, while the single hadron interpolators with non-zero momentum, used to construct optimised interpolators, are those discussed in section 3.3.1. The number of optimised two-hadron interpolators used within each overall momentum $\vec{P}$ and irrep, for the study of $D\pi$ scattering, is shown in Table 8.2.

8.2 $I = 3/2$ $D\pi$ Multi-Particle Spectrum

It is clear from Figures 6.3 and 6.4 that multi-hadron effects play an important role in both the charm-light and charm-strange spectra. In both sectors, the P-wave supermultiplet lies around the lowest non-interacting thresholds, which are the $D\pi$ and $D_s\bar{K}$ thresholds in the charm-light sector, and the DK threshold in the charm-strange sector. We noted that, in both sectors we find a significant volume

$\vec{P}$	$\vec{k}_1$	$\vec{k}_2$	$\Lambda^{(P)}$
$[0,0,0]$ O_h^D	$[0,0,0]$	$[0,0,0]$	A_1^+
	$[0,0,1]$	$[0,0,-1]$	A_1^+, E^+, T_1^-
	$[0,1,1]$	$[0,-1,-1]$	$A_1^+, E^+, T_2^+, T_1^-, T_2^-$
	$[1,1,1]$	$[-1,-1,-1]$	$A_1^+, T_2^+, T_1^-, A_2^-$
	$[0,0,2]$	$[0,0,2]$	A_1^+, E^+, T_1^-
$[0,0,1]$ Dic_4	$[0,0,0]$	$[0,0,1]$	A_1
	$[0,-1,0]$	$[0,1,1]$	A_1, E_2, B_1
	$[0,-1,-1]$	$[1,1,1]$	A_1, E_2, B_2
	$[0,0,-1]$	$[0,0,2]$	A_1
$[0,1,1]$ Dic_2	$[0,0,0]$	$[0,1,1]$	A_1
	$[0,1,0]$	$[0,0,1]$	A_1, B_1
	$[-1,0,0]$	$[1,1,1]$	A_1, B_2
	$[1,1,0]$	$[-1,0,1]$	A_1, A_2, B_1, B_2
	$[0,1,-1]$	$[0,0,2]$	A_1, B_1
$[1,1,1]$ Dic_3	$[0,0,0]$	$[1,1,1]$	A_1
	$[1,0,0]$	$[0,1,1]$	A_1, E_2
	$[2,0,0]$	$[-1,1,1]$	A_1, E_2

TABLE 8.1: The two-hadron interpolators for each overall momentum $\vec{P}$ and little group. Example momenta, $\vec{k}_1$ and $\vec{k}_2$, that combine to form the overall momentum, $\vec{P}$, are shown. Parity is only a good quantum number for interpolators overall at rest.

dependence in our determination of the lightest states in the 0^+ and 1^+ channels. This suggested that for a full understanding of these states, we require a handle on relevant multi-particle states.

The most obvious place to start in the charm-strange sector is to calculate two-point correlation functions built from interpolators that *look-like* a DK combination, while in the charm-light sector it would be to explore correlation functions built from $D\pi$ interpolators.

$\vec{P}$	$\Lambda^{(P)}$	Number of Interpolators
$[0,0,0]$ O_h^D	A_1^+	5
$[0,0,1]$ Dic_4	A_1	8
$[0,1,1]$ Dic_2	A_1	8
$[1,1,1]$ Dic_3	A_1	6

TABLE 8.2: The number of optimised two-hadron interpolators for each overall momenta $\vec{P}$ and irrep $\Lambda^{(P)}$ used in the calculation of the $D\pi$ energy levels. Parity is only a good quantum number for interpolators overall at rest.

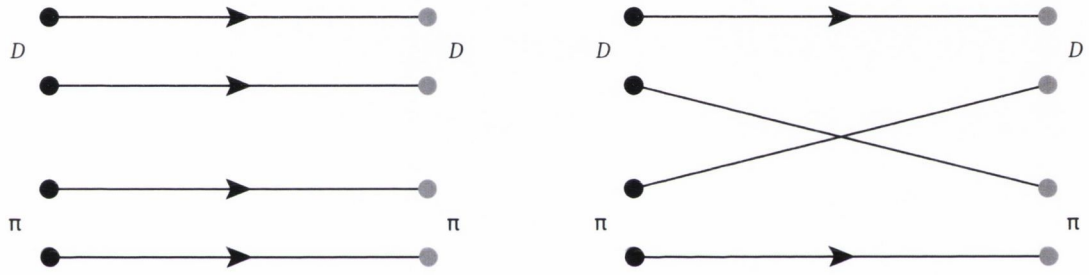

FIGURE 8.1: The $I = 3/2$ Wick diagrams computed in our calculation of the $D\pi$ spectrum. Recall that on our lattices we have degenerate up and down quarks.

This work is currently ongoing, and what is presented in this section is a preliminary study of two-point correlation functions composed of interpolators that *look-like* a $D\pi$ combination in the isospin, $I = 3/2$, channel. We begin with this channel as a test case, since we do not expect any resonances to appear and due to the smaller number of Wick diagrams, which are shown in Figure 8.1, it is computationally cheaper than the $I = 1/2$ case, which will also have an annihilation diagram. In the following section, we then apply the Lüscher formalism to map out the (preliminary) $l = 0$ elastic scattering phase shift.

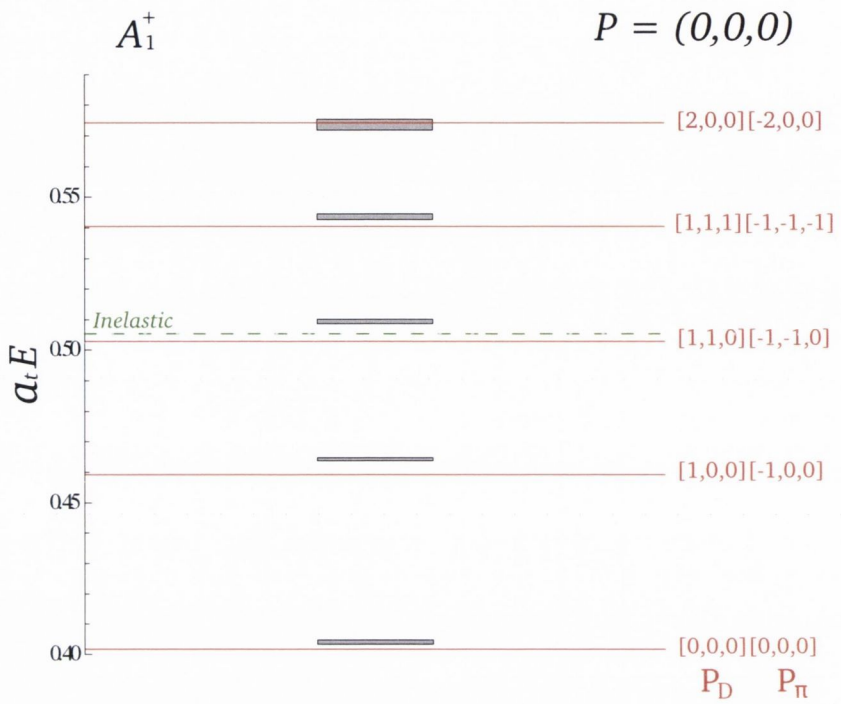

FIGURE 8.2: The $D\pi$ spectrum for overall momentum $P = (0,0,0)$ in the A_1^+ irrep for isospin, $I = 3/2$, calculated on our $20^3 \times 128$ volume. The black boxes correspond to calculated energy levels, while the red lines correspond to the non-interacting threshold obtained by adding together the calculated individual values of the D meson and pion. The green dashing shows the inelastic threshold in this channel, $D^*\rho$. The momenta P_D and P_π indicate the individual momenta of the D meson and pion that combine to make up the overall momentum P.

To compute $D\pi$ spectroscopic states, we employ the same techniques that were applied for the charmonium and open-charm spectra; we compute an $N \times N$ correlation matrix composed of two-point correlation functions, which themselves are built from the optimised interpolators discussed earlier. We include optimised interpolators up to an overall momentum of $P^2 = 3$, and we only consider the relevant $A_1^{(+)}$ irreps (see Table 8.2). Our calculation is performed on our $20^3 \times 128$ volume, the details of which are shown in Table 2.3.

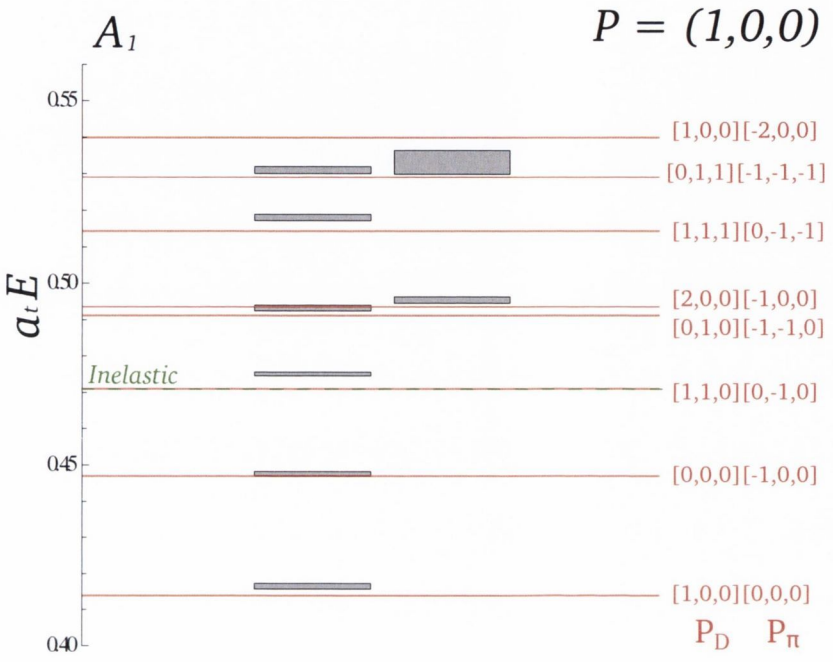

FIGURE 8.3: The $D\pi$ spectrum for overall momentum $P = (0,0,1)$ in the A_1 irrep for isospin, $I = 3/2$, calculated on our $20^3 \times 128$ volume. The black boxes correspond to calculated energy levels, while the red lines correspond to the non-interacting threshold obtained by adding together the calculated individual values of the D meson and pion. The green dashing shows the inelastic threshold in this channel, $D\pi\pi$. The momenta P_D and P_π indicate the individual momenta of the D meson and pion that combine to make up the overall momentum P.

Once we have computed the correlation matrix, we then apply the variational procedure in the same fashion as before. However, there is one difference in the role of the extracted overlap factors, Z. As before, they are used to identify which interpolator(s) has contributed significantly to a given state. In all cases, there is a clear preference for overlap of our extracted $D\pi$ states with a single interpolator. This allows us to identify the internal momentum structure that has mainly contributed to that state, which is crucial when calculating the energy shift from its non-interacting counterpart.

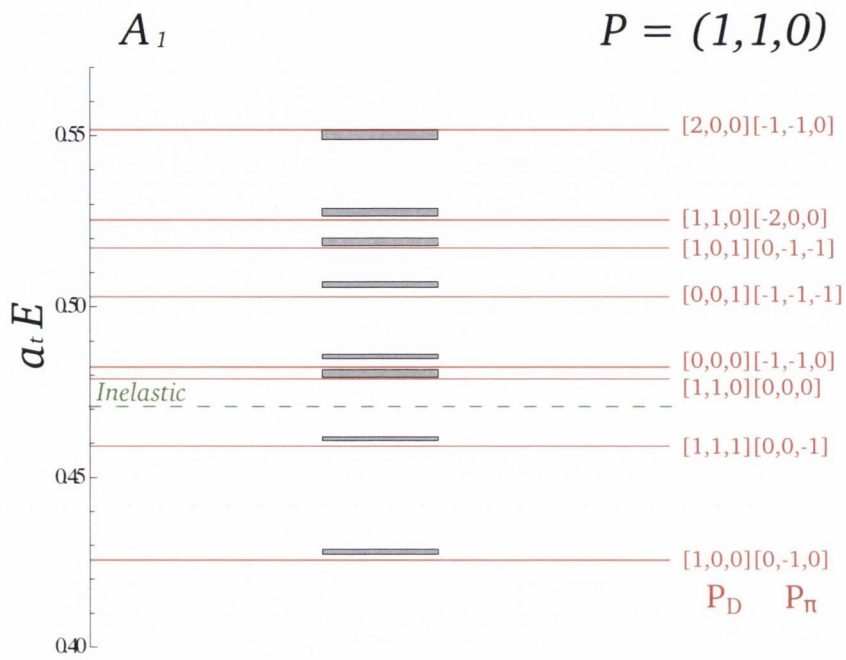

FIGURE 8.4: The $D\pi$ spectrum for overall momentum $P = (0,1,1)$ in the A_1 irrep for isospin, $I = 3/2$, calculated on our $20^3 \times 128$ volume. The black boxes correspond to calculated energy levels, while the red lines correspond to the non-interacting threshold obtained by adding together the calculated individual values of the D meson and pion. The green dashing shows the inelastic threshold in this channel, $D\pi\pi$. The momenta P_D and P_π indicate the individual momenta of the D meson and pion that combine to make up the overall momentum P.

In Figure 8.2 we show the $D\pi$ spectrum, for overall momentum at rest, calculated in the A_1^+ irrep, for isospin $I = 3/2$. The black boxes show the calculated energy levels, and the size of each box corresponds to the one-sigma uncertainty. The red lines correspond to the non-interacting $D\pi$ energy levels, calculated on our ensembles. The green dashing corresponds to the inelastic threshold, $D^*\rho$.

In Figure 8.3, we show a similar plot, but this time it is for overall momentum $\vec{P} = (0,0,1)$, in the A_1 irrep. It is important to note that parity is no longer a

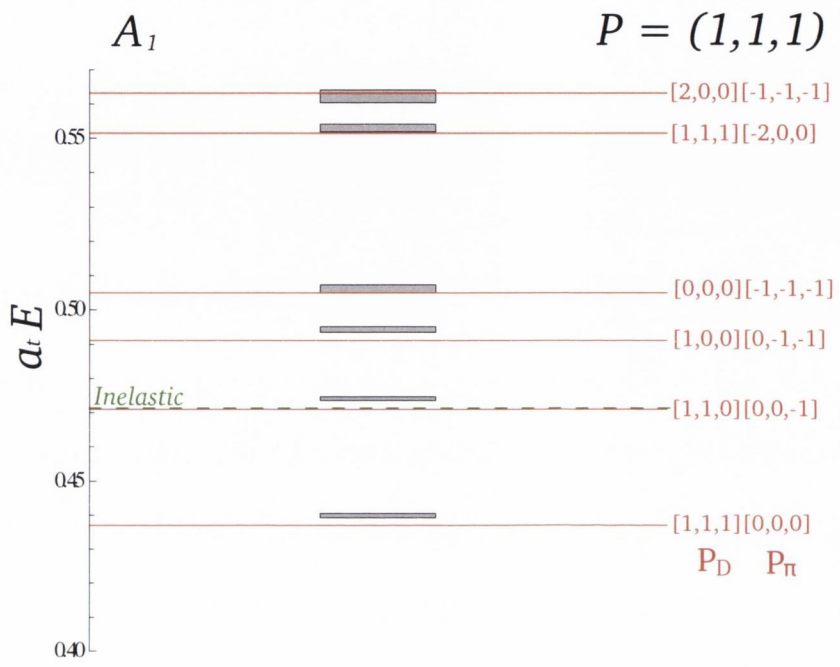

FIGURE 8.5: The $D\pi$ spectrum for overall momentum $P = (1,1,1)$ in the A_1 irrep for isospin, $I = 3/2$, calculated on our $20^3 \times 128$ volume. The black boxes correspond to calculated energy levels, while the red lines correspond to the non-interacting threshold obtained by adding together the calculated individual values of the D meson and pion. The green dashing shows the inelastic threshold in this channel, $D\pi\pi$. The momenta P_D and P_π indicate the individual momenta of the D meson and pion that combine to make up the overall momentum P.

good quantum number for our interpolator construction at non-zero momenta. This means that the inelastic threshold is $D\pi\pi$ for states having non-zero momentum overall. We show similar plots for overall momenta $\vec{P} = (0,1,1)$ and $\vec{P} = (1,1,1)$ in Figures 8.4 and 8.5 respectively.

8.3 $I = 3/2$ $D\pi$ Phase Shift

We now apply the Lüscher formalism and its extension to moving frames, to our $D\pi$ spectra. Recall that the formalism can be expressed by the equation

$$\det\left[\mathbf{E}(p_{cm}) - \mathbf{U}^{(\vec{P},\Lambda)}\left(q^2\right)\right] = 0\ , \tag{8.17}$$

where $\mathbf{U}$ is an infinite dimensional matrix of known functions $U_{l,n;l',n'}$. Here, l are the partial waves in the irrep Λ, and n labels the n^{th} embedding of that l in this irrep. $\mathbf{E}$ is a diagonal matrix whose elements are given by $E_{l,n;l'n'} = e^{2i\delta_l}\delta_{l,l'}\delta_{n,n'}$. As explained in section 8.1, $\mathbf{U}$ is given by

$$\mathbf{U}(q^2) = \frac{\mathbf{M}(q^2) + i}{\mathbf{M}(q^2) - i}\ , \tag{8.18}$$

where the elements of $\mathbf{M}$ are obtained via [80]

$$M^{(\vec{P},\Lambda,\mu)}_{ln;l'n'}(q^2)\delta_{\Lambda,\Lambda'}\delta_{\mu,\mu'} = \sum_{\substack{\lambda \\ m=-l\ldots l}}\ \sum_{\substack{\lambda' \\ m'=-l'\ldots l'}} S^{*\lambda}_{\vec{P},\Lambda,\mu} D^{*(l)}_{m\lambda}(R)\ M^{(\vec{P})}_{lm;l'm'}(q^2)\ S^{*\lambda'}_{\vec{P},\Lambda',\mu'} D^{*(l')}_{m'\lambda'}(R)\ . \tag{8.19}$$

Here, R is a rotation carrying the J_z quantisation axis $(0,0,P)$ to $\vec{P}$, with $D^{(l)}_{m\lambda}(R)$ relating J_z values, m, to helicities, λ. The convention for constructing R is given in [76]. $S^{\lambda}_{\vec{P},\Lambda,\mu}$ is the subduction coefficient from helicity, λ, to the μ^{th} row of irrep Λ. Different magnitudes of helicity give rise to different embeddings n, n'. $M^{(\vec{P})}_{lm;l'm'}(q^2)$ is defined in equation (8.14).

There are infinitely many partial waves to consider in any given irrep. However, in practise it is very difficult to consider more than the first one or two partial waves. Fortunately, at low scattering momentum there is a hierarchy in $\delta_l(p_{cm})$, which follows from angular momentum conservation, $\delta_l(p_{cm}) \sim p_{cm}^{2l+1}$, such that

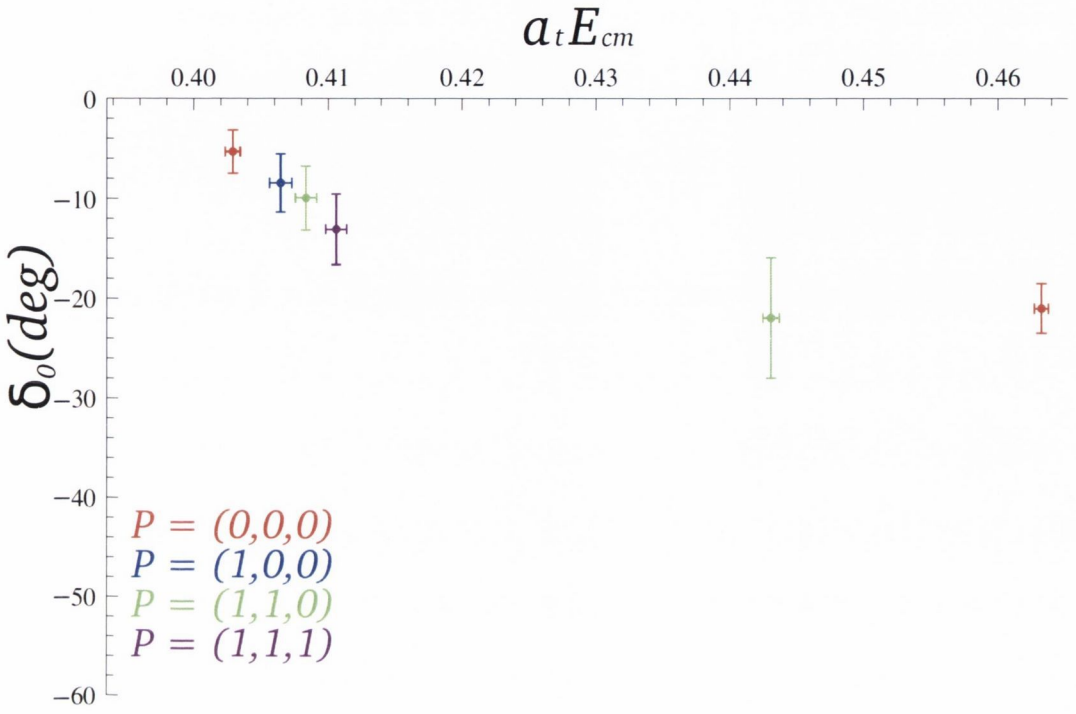

FIGURE 8.6: The phase shift, δ_0, in the elastic scattering region determined from the $D\pi$ spectrum calculated on our $20^3 \times 128$ volume. The error bars represent the statistical uncertainty. The center-of-momentum frame energies are given in lattice units and all points lie below the inelastic threshold in their corresponding symmetry channel.

$\delta_0 \gg \delta_2 \gg \delta_4$. This implies that we are somewhat justified in only considering the first partial wave in the A_1 irreps, $l = 0$.

To compute the $l = 0$ elastic phase shift, δ_0, we solve equation (8.17) using the shift in energy levels obtained from the $D\pi$ spectra. In Figure 8.6 we show δ_0 as a function of center-of-momentum frame energies. As previously mentioned, resonances show up as a rapid variation through 180 degrees in the scattering phase shift, and from Figure 8.6, it is clear that we see no such behaviour, and hence, no resonance.

In [96], the authors also explore $D\pi$ scattering on the lattice. They calculate S-wave

phase shifts for $D\pi$ scattering with $J^P = 0^+$ and $D^*\pi$ scattering with $J^P = 1^+$. Assuming a Breit-Wigner shape in the $J^P = 0^+$ channel, they observe a resonance at a mass of 351(21) MeV above their calculated spin-average $\frac{1}{4}(M_D + 3M_{D^*})$. This is in agreement with the experimentally observed $D^*(2400)$, whose mass is 347(29) MeV above the experimental spin-average value. In the $J^P = 1^+$ channel they find a resonance with a mass of 381(20) MeV above $\frac{1}{4}(M_D + 3M_{D^*})$, which lies significantly lower than the experimental value of 456(40) MeV above $\frac{1}{4}(M_D + 3M_{D^*})$ for the $D_1(2430)$.

As previously mentioned, our study of $D\pi$ scattering is ongoing. The obvious next step would be to add data points to Figure 8.6 by calculating the $D\pi$ multi-hadron spectrum on different volumes. Looking beyond this, we plan to supplement and improve on the study in [96] by considering firstly the $D\pi$ $I = 1/2$ channel, and then by extending our study to include other scattering channels such as the $J^{(P)} = 1^{(+)}$ channel.

Conclusions and Outlook

We have computed extensive spectra in the charmonium, charm-light and charm-strange sectors. The use of distillation, the variational method with a large basis of carefully constructed interpolators and our spin identification scheme has allowed us to extract a high number of states across all possible $J^{P(C)}$ combinations up to and including spin four. We calculate these spectra on two volumes, $16^3 \times 128$ and $24^3 \times 128$.

In the charmonium sector, we find no significant volume dependence and also that the spectrum is stable with respect to changes in the details of the variational analysis and variation of the number of eigenvectors. We carried out an investigation of lattice discretisation effects by varying the spatial clover coefficient, however, a more complete determination of the systematic uncertainty would require several lattice spacings. This work is the first time that a dynamical spectrum of charmonium has been computed that includes the exotic states $(0^{+-}, 1^{-+}, 2^{+-})$. Interestingly, our determination of these states points to the presence of explicit gluonic degrees of freedom. Most of the non-exotic spectrum appears to follow the $n^{2S+1}L_J$ pattern expected by quark models. However, we do find some states that do not appear to fit into this classification. We interpret these states as non-exotic hybrids, and identify the lightest hybrid supermultiplet in the charmonium sector $[(0, 1, 2)^{-+}1^{--}]$. We

also observe an excited hybrid supermultiplet. The pattern of states is consistent with the interpretation of a colour octet quark-antiquark pair coupled to a P-wave 1^{+-} chromomagnetic excitation. Our results allow an interpretation of the $Y(4260)$ as a non-exotic vector hybrid meson, but, based only on mass comparisons, we can not draw definite conclusions. Following the study of [62], we see no clear evidence for multi-hadron states.

In the open-charm spectra, we observe no significant volume dependence except for the lightest states in the 0^+ and 1^+ channels. In general, both the charm-light and charm-strange spectra follow the pattern of states expected by quark models. Although, we do find four states, $[(0,1,1,2)^-]$, in the negative parity sectors of both spectra that we interpret as hybrid mesons due to their relatively large overlap onto interpolators proportional to the field strength tensor. The pattern of these states is consistent with what is found in the light meson sector [104] and in the charmonium sector, which is suggestive of common physics throughout QCD.

Via a non-relativistic interpretation of some of our interpolators, we extracted mixing angles between the P and D-wave spin-singlet and triplet states, 1^+, 2^-, and the hybrid 1^- states. The results we obtain in the charm-light and charm-strange sectors are very similar but we note that $SU(3)$ flavour symmetry is highly suppressed on our ensembles. Nevertheless, we expect the flavour symmetry breaking in the charm-strange sector to be of the correct scale.

We have also presented preliminary results of the isospin $I = 3/2$ $D\pi$ multi-hadron spectrum calculated on our $20^3 \times 128$ volume. We calculate the energy shift of the multi-hadron states from their non-interacting counterparts below the inelastic threshold and employ the Lüscher formalism to map out the elastic scattering phase

shift only considering the $l = 0$ partial wave. As expected we find no resonance in the $I = 3/2$ channel, but to further map out the phase shift we require calculations on more volumes.

In the near future we plan to extend our study of $D\pi$ scattering to the $I = 1/2$ channel, where we expect to detect a resonance. In order to better understand the enigmatic $D_{s0}(2317)^{\pm}$ and $D_{s1}(2460)^{\pm}$ states, we plan to explore DK scattering. We expect this scattering channel to play an important role in the determination of these states as they lie very close to the DK threshold.

Appendix A

Tabulated Results

Table A.1 tabulates the masses as presented in Figure 5.3. The calculated η_c mass has been subtracted in order to reduce the systematic error when setting the mass of the charm quark. Table A.2 tabulates the masses as presented in Figure 6.3. Half of the calculated η_c mass is subtracted to reduce the systematic error when setting the mass of the charm quark. Table A.3 is the same but for masses presented in Figure 6.4.

J^{PC}	$(M - M_{\eta_c})$ (MeV)					
0^{-+}	0	663(3)	1143(13)	1211(13)		
1^{--}	80.2(1)	698(6)	840(3)	1154(28)	1301(14)	1339(38)
2^{-+}	860(3)	1334(17)	1350(17)			
2^{--}	859(5)	1333(18)				
3^{--}	867(3)	1269(26)	1392(12)			
4^{-+}	1444(10)					
4^{--}	1427(9)					
0^{++}	461.6(7)	972(9)	1361(46)	1488(30)		
1^{+-}	534(1)	1006(9)	1360(38)	1462(51)	1493(19)	1513(39)
1^{++}	521.6(9)	1002(10)	1415(14)	1484(48)		
2^{++}	554(1)	1041(12)	1112(8)	1508(21)		
3^{+-}	1142(6)	1564(22)				
3^{++}	1130(9)					
4^{++}	1129(9)					
1^{-+}	1233(16)					
0^{+-}	1402(9)					
2^{+-}	1411(40)	1525(18)				

TABLE A.1: Summary of the charmonium spectrum calculated on our $24^3 \times 128$ volume, as presented in Figure 5.3, with statistical uncertainties shown. Note that $M_\pi \approx 391$ MeV in these simulations. The calculated η_c mass has been subtracted in order to reduce the systematic error from the tuning of the bare charm quark mass. The masses of states with $J \geq 2$ are from joint fits to principal correlators across the relevant irreps.

J^P	$M - M_{\eta_c}/2$ (MeV)					
0^-	403(1)	1155(7)	1575(16)	1811(14)		
1^-	527(1)	1220(7)	1361(5)	1612(14)	1704(19)	1907(14)
2^-	1377(5)	1380(5)	1856(15)	1911(29)	1944(19)	
3^-	1384(9)	1990(17)				
4^-	1968(24)	2028(23)				
0^+	854(3)	1505(11)	1861(16)			
1^+	959(3)	992(3)	1563(11)	1565(11)	1849(21)	1919(13)
2^+	1024(3)	1594(10)	1707(5)	1929(13)		
3^+	1708(6)	1718(8)				
4^+	1720(14)					

TABLE A.2: Summary of the charm-light meson spectrum calculated on our $24^3 \times 128$ volume, as presented in Figure 6.3, with statistical uncertainties shown. Note that $M_\pi \approx 391$ MeV in these computations. Half of the calculated η_c mass has been subtracted in order to reduce the systematic error from the tuning of the bare charm quark mass. The masses of states with $J \geq 2$ are from joint fits to principal correlators across the relevant irreps.

J^P	$M - M_{\eta_c}/2$ (MeV)					
0^-	469(1)	1186(8)	1631(13)	1835(15)		
1^-	589(5)	1267(6)	1398(5)	1674(13)	1771(16)	1952(13)
2^-	1425(4)	1429(4)	1840(18)	1977(21)	1986(15)	
3^-	1452(6)	2030(14)				
4^-	2023(14)	2027(16)				
0^+	920(2)	1543(10)	1945(8)			
1^+	1019(3)	1055(5)	1601(10)	1613(9)	1895(16)	1988(34)
2^+	1087(2)	1651(10)	1736(7)	1998(14)		
3^+	1749(7)	1767(7)				
4^+	1766(14)					

TABLE A.3: Summary of the charm-strange meson spectrum calculated on our $24^3 \times 128$ volume, as presented in Figure 6.4, with statistical uncertainties shown. Note that $M_\pi \approx 391$ MeV in these computations. The calculated η_c mass has been subtracted in order to reduce the systematic error from the tuning of the bare charm quark mass. The masses of states with $J \geq 2$ are from joint fits to principal correlators across the relevant irreps.

Bibliography

[1] J C Maxwell. *A Dynamical Theory of the Electromagnetic Field.* Philosophical Transactions of the Royal Society of London **155**, 459–512, (1865).

[2] A Einstein. *Zur Elektrodynamik Bewegter Körper.* Annalen der Physik 17:891, (1905).

[3] W Heisenberg. *über quantentheoretische umdeutung kinematischer und mechanischer beziehungen.* Zeitschrift für Physik, **33**, 879-893, (1925).

[4] M Born and P Jordan. *Zur Quantenmechanik.* Zeitschrift für Physik, **34**, 858-888, (1925).

[5] M Born et al. *Zur Quantenmechanik II.* Zeitschrift für Physik, **35**, 557-615, (1926).

[6] H Minkowski. *Raum und Zeit.* Nachrichten von der Gesellschaft der Wissenschaften zu Göttingen, Mathematisch-Physikalische Klasse: 53–111, (1908).

[7] J S Bell. *On the Einstein-Podolsky-Rosen paradox.* Physics, 1: 195–200, (1964).

[8] S Kochen and E Specker. *The Problem of Hidden Variables in Quantum Mechanics.* Journal of Mathematics and Mechanics, **17**, 59-87, (1967).

[9] P A M Dirac. *The Quantum Theory of the Emission and Absorption of Radiation.* Proceedings of the Royal Society of London, Series A, Vol. 114, p. 243, (1927).

[10] R Feynman. *The Strange Theory of Light and Matter.* The Strange Theory of Light and Matter. Princeton University Press. p. 128. ISBN 978-0-691-12575-6, (1985).

[11] R Haag. *On Quantum Field Theories.* Matematisk-fysiske Meddelelser, **29**, 12 (1955).

[12] A S Wightman. *A Theorem on Invariant Analytic Functions with Applications to Relativistic Quantum Field Theory.* Matematisk-fysiske Meddelelser, **31**, 1, (1957).

[13] R Schrader. *On the Euclidean Version of Haags Theorem in $P(\phi)_2$ Theories.* Commun. Math. Phys. **36**, 133, (1974).

[14] J Goldstone. *Field Theories with Superconductor Solutions.* Nuovo Cim. **19**, 154, (1961).

[15] Y Nambu. *Axial Vector Current Conservation in Weak Interactions.* Phys. Rev. Lett. **4**, 380, (1960).

[16] A Salam and J C Ward. *On the Gauge Theory of Elementry Interactions.* Nuovo Cim. **19**, 165 (1961).

[17] P W Higgs. *Broken Symmetries, Massless Particles and Gauge Bosons*, . Phys. Lett. **12**, 132, (1964).

[18] P W Higgs. *Broken Symmetries and the Masses of Gauge Bosons*, . Phys. Lett. **13**, 508, (1964).

[19] F Englert and R Brout. *Broken Symmetries and the Mass of Gauge Vector Mesons.* Phys. Rev. Lett. **13**, 321, (1964).

[20] G S Guralnnik et al. *Global Conservation Laws and Massless Particles.* Phys. Rev. Lett. **13**, 585, (1964).

[21] T W B Kibble. *Symmetry Breaking in Non-Abelian Gauge Theories.* Phys. Rev. **155**, 1554, (1967).

[22] L D Fadeev and V N Popov. *Feynman Diagrams for the Yang-Mills Field.* Phys. Lett. B **25**, 29, (1967).

[23] D J Gross. *Twenty Five Years of Asymptotic Freedom.* Nucl. Phys. Proc. Suppl. **74** 426, (1999). arXiv:hep-th/9809060.

[24] K G Wilson. *Confinement of Quarks.* Phys. Rev. D **10**, 2445, (1974).

[25] G Aad et al. *Observation of a New Particle in the Search for the Standard Model Higgs Boson With the ATLAS Detector at the LHC.* Phys. Lett. B **716**, 1, (2012).

[26] S Chatrchyan et al. *Observation of a New Boson at a Mass of* $125GeV$ *With the CMS Experiment at the LHC.* Phys. Lett. B **716**, 1, (2012).

[27] C Grattringer and C B Lang. *Quantum Chromodynamics on the Lattice: An Introductory Presentation.* Springer Lecture Notes in Physics, Vol. 788, (2010).

[28] P T Matthews and A Salam. *Propagators of Quantized Field.* Nuovo Cim. 12, 563, 108 (1954).

[29] H B Nielson and M Ninomiya. *A No-Go Theorem For Regularizing Chiral Fermions.* Phys. Lett. B **105**, 219, (1981).

[30] J Kogut and L Susskind. *Hamiltonian Formulation of Wilson's Lattice Gauge Theory.* Phys. Rev. D **11**, 395, 243, (1975).

[31] R Frezzotti et al. *A Local Formulation of Lattice QCD Without Unphysical Fermion Zero Modes*, . Nucl. Phys. (Proc. Suppl.) **83**, 941, 254, (2000).

[32] R Frezzotti et al. *Lattice QCD with a Chirally Twisted Mass Term*, . JHEP **0107**, 058, 254, 257, (2001).

[33] R Frezzotti et al. *O(a) Improved Twisted Mass Lattice QCD*, . JHEP **048**, 254, 259, (2001).

[34] I Montvay and G Münster. *Quantum Fields on a Lattice.* Cambridge University Press, Cambridge, New York, 141, (1994).

[35] T DeGrand and C DeTar. *Lattice Methods for QuantumChromodynamics.* World Scientific, Singapore, 219, (2006).

[36] K Symanzik. *Continuum Limit and Improved Action in Lattice Theories. 1. Principles and ϕ^4 Theory*, . Nucl. Phys. B **226**, 187, (1983).

[37] K Symanzik. *Continuum Limit and Improved Action in Lattice Theories. 2. $O(N)$ Non-Linear Sigma Model in Perturbation Theory*, . Nucl. Phys. B **226**, 205, (1983).

[38] P Lepage and P B Mackenzie. *Viability of Lattice Perturbation Theory.* Phys. Rev. D **48**, 2250, (1993).

[39] M Lüscher and P Weisz. *On Shell Improved Lattice Gauge Theories.* Commun. Math. Phys. **97**, 59, (1985).

[40] B Sheikholeslami and R Wohlert. *Improved Continuum Limit Lattice Action for QCD with Wilson Fermions.* Nucl. Phys. B. **259**, 572, 216, (1985).

[41] M Lüscher. *Advanced Lattice QCD*, . Notes from lectures given at the Les Houches summer school "Probing the Standard Model of Particle Interactions", July (1997).

[42] R Wohlert. DESY preprint (unpublished) 87-096, (1987).

[43] M Lüscher, S Sint, R Sommer, and P Weisz. *Chiral Symmetry and $O(a)$ Improvement in Lattice QCD*, . Nucl Phys B **478**, 365, 216 (1996).

[44] B J Bjorken and S L Glashow. *Elementary Particles and $SU(4)$*. Phys. Lett. **11**, 255, (1964).

[45] S L Glashow et al. *Weak Interactions with Lepton-Hadron Symmetry*. Phys. Rev. D **2**, 1285, (1970).

[46] J Aubert et al. *Experimental Observation of a Heavy Particle J*, . Phys. Rev. Lett. **33**, 1404, (1974).

[47] J Augustin et al. *Discovery of a Narrow Resonance in e^+e^- Annihilation.* Phys. Rev. Lett. **33**, 1406, (1974).

[48] J Beringer et al. *Review of Particle Physics*. Phys. Rev. D **86**, 010001, (2012).

[49] S Godfrey and N Isgur. *Mesons in a Relativised Quark Model with Chromodynamics*. Phys. Rev. D **32**, 198, (1985).

[50] F Close and E Swanson. *Dynamics and Decay of Heavy-Light Hadrons*. Phys. Rev. D **72**, 094004, (2005).

[51] J Aubert et al. *Observation of a Narrow Meson Decaying to $D_s^+\pi^0$ at a Mass of $2.32GeV/c^2$*, . Phys. Rev. Lett. **90**, 242001, (2003).

[52] D Besson et al. *Observation of a Narrow Resonance of Mass* $2.46GeV/c^2$ *Decaying to* $D_s^* + \pi^0$ *and Confirmation of the* $D_s^*(2317)$ *State.* Phys. Rev. D **68**, 032002, (2003).

[53] S K Choi et al. *Observation of a Narrow Charmonium-Like State in Exclusive* $B^+ \to K^{\pm}\pi^+\pi - J/\psi$ *Decays*, . Phys. Rev. Lett **91**, 262001, (2003).

[54] S K Choi et al. *Observation of a Resonance Like Structure in the* $\pi^{\pm}\psi'$ *Mass Distribution in Exclusive* $B \to K\pi^{\pm}\psi'$ *Decays*, . Phys. Rev. Lett **100**, 142001, (2008).

[55] E Klempt. *Glueballs, Hybrids, Petaquarks: An Introduction to Hadron Spectroscopy and Review of Selected Topics.* Lectures given at HUGS, JLAB, (2003).

[56] A X El-Khadra, A S Kronfeld, and P B Mackenzie. *Massive Fermions in Lattice Gauge Theories.* Phys. Rev. D **55**, 3933, (1997).

[57] E Follana et al. *Highly Improved Staggered Quarks on the Lattice, with Applications to Charm Physics.* Phys. Rev. D **75**, 054502, (2007).

[58] R G Edwards, B Joo, and H W Lin. *Tuning for Three-Flavors of Anisotropic Clover Fermions with Stout-Link Smearing.* Phys. Rev. D**78**, 054501, (2008).

[59] H W Lin et al. *First Results from* $2 + 1$ *Dynamical Quark Flavours on an Anisotropic Lattice: Light Hadron Spectroscopy and Setting the Strange Quark Mass.* Phys. Rev. D**79**, 034502, (2009).

[60] R Morrin et al. *Dynamical QCD Simulations on Anisotropic Lattices.* Phys. Rev. D**74**, 014505, (2006).

[61] J J Dudek, R G Edwards, and C E Thomas. *S and D-wave Phase Shifts in Isospin-2* $\pi\pi$ *Scattering from Lattice QCD*, . Phys. Rev. D **86**, 034031 (2012).

[62] J J Dudek et al. *Toward the Excited Meson Spectrum of Lattice QCD*, . Phys. Rev. D **82**, 034508 (2010).

[63] C Morningstar and M Peardon. *The Glueball Spectrum from an Anisotropic Lattice Study*, . Phys. Rev. D *60*, 034509, (1999).

[64] K Juge et al. *Excitations of Torelons*, . Nucl. Phys. Proc. Suppl. **129**, 703, (2004).

[65] K Juge, J Kuti, and C Morningstar. *QCD String Spectrum 2002*, . Phys. Rev. Lett. **90**, 161601, (2003).

[66] T Blum et al. *Improving Flavour Symmetry in the Kogut-Susskind Hadron Spectrum.* Phys. Rev. D **55**, 1133, (1997).

[67] T DeGrand. *Tests of Hypercubic Fermion Actions.* Phys. Rev. D **58**, 094503, (1998).

[68] M Albanese et al. *Glueball Masses and String Tension in Lattice QCD.* Phys. Lett. B **192**, 163, (1987).

[69] C Morningstar and M Peardon. *Analytic Smearing of $SU(3)$ Link Variables in Lattice QCD*, . Phys. Rev. D **69**, 054501, (2004).

[70] I Horvath, A D Kennedy, and S Sint. *A New Exact Method for Dynamical Fermion Computations with Non-Local Actions.* Nucl. Phys. Proc. Suppl. **73**, 834, (1999).

[71] C R Alton et al. *Gauge-Invariant Smearing and Matrix Correlators Using Wilson Fermions at β = 6.2.* Phys. Rev. D **47**, 5128, (1993).

[72] M Peardon et al. *A Novel Quark-Field Creation Operator Construction for Hadronic Physics in Lattice QCD.* Phys. Rev. D **80**, 054506, (2009).

[73] J J Dudek et al. *Isoscalar Meson Spectroscopy from Lattice QCD*, . Phys. Rev. D**83**, 034508, (2010).

[74] J J Dudek et al. *Highly Excited and Exotic Meson Spectrum From Dynamical Lattice QCD*, . Phys. Rev. Lett. **103**, 262001, (2009).

[75] D C Moore and G T Fleming. *Angular Momentum on the Lattice: The Case of Non-Zero Linear Momentum.* Phys. Rev. D**73**, 014504, (2006).

[76] C E Thomas, R G Edwards, and J J Dudek. *Helicity Operators for Mesons In Flight on the Lattice.* Phys. Rev. D **85**, 014507, (2012).

[77] M Lüscher and U Wolff. *How to Calculate the Elastic Scattering Matrix in Two Dimensional Quantum Field Theories by Numerical Simulation.* Nucl. Phys. B**339**, 222, (1990).

[78] C Michael. *Adjoint Sources in Lattice Gauge Theory.* Nucl. Phys. B**259**, 58, (1985).

[79] B Blossier et al. *On the Generalized Eigenvalue Method for Energies and Matrix Elements in Lattice Field Theory*, . JHEP **0904**, 094, (2009).

[80] J J Dudek et al. *Charmonium Excited State Spectrum in Lattice QCD*, . Phys. Rev. D**77**, 034501, (2008).

[81] J J Dudek et al. *Excited State Baryon Spectroscopy from Lattice QCD*, . Phys. Rev. D**83**, 034508, (2010).

[82] J Bulava et al. *Nucleon, Δ and Ω excited States in $N_f = 2 + 1$ Lattice QCD.* Phys. Rev. D**82**, 014507, (2010).

[83] Z Davoudi and M Savage. *Restoration of Rotational Symmetry in the Continuum Limit of Lattice Gauge Theories.* Phys. Rev. D**86**, 054505, (2012).

[84] L Levkova and C DeTar. *Charm Annihilation Effects on the Hyperfine Splitting in Charmonium.* Phys. Rev. D**83**, 074504, (2011).

[85] G Bali et al. *Spectra of Heavy-Light and Heavy-Heavy Mesons Containing Charm Quarks*, . POS LATTICE 2011, 135, (2011).

[86] M Lüscher et al. *Non-Perturbative $O(a)$ Improvement of Lattice QCD*, . Nucl. Phys. B**491**, 323, (1997).

[87] G Bali, S Collins, and C Ehmann. *Charmonium Spectroscopy and Mixing with Light Qurak and Open-Charm States from $N_f = 2$*, . Phys. Rev. D**84**, 094506, (2011).

[88] T Burch et al. *Quarkonium Mass Splittings in Three-Flavor Lattice QCD*, . Phys. Rev. D**81**, 034508, (2010).

[89] J J Dudek and E Rrapaj. *Charmonium in Lattice QCD and the Non-Relativistic Quark Model.* Phys. Rev. D**78**, 094504, (2008).

[90] T K Pedlar et al. *Observation of the $h_c(1P)$ Using e^+e^- Collisions Above $D\bar{D}$ Threhold.* Phys. Rev. Lett. **107**, 041803, (2011).

[91] R Aaij et al. *Determination of the $X(3872)$ Meson Quantum Numbers.* Phys. Rev. Lett. **110**, 222001, (2013).

[92] Y Namekawa et al. *Charm Quark System at the Physical Point of 2+1 Flavour Lattice QCD.* Phys. Rev. D**84**, 074505, (2011).

[93] C McNeile et al. *Heavy Meson Masses and Decay Constants from Relativistic Heavy Quarks in Full Lattice QCD.* Phys. Rev. D**86**, 074503, (2012).

[94] R Dowdall et al. *Precise Heavy Light Meson Masses and Hyperfine Splittings from Lattice QCD Including Charm Quarks in The Sea.* Phys. Rev. **D**86, 094510 (2012).

[95] D Mohler and R M Woloshyn. *D and D_s Meson Spectroscopy.* Phys. Rev. D**84**, 054505, (2011).

[96] D Mohler, S Prelovsek, and R M Woloshyn. *$D\pi$ Scattering and D Meson Resonances.* Phys. Rev. D**87**, 034501, (2013).

[97] S Godfrey and R Kokoski. *Properties of P-wave Mesons with One Heavy Quark.* Phys. Rev. D**43**, 1679, (1991).

[98] K Abe et al. *Study of $B^- \to D_0^{**}\pi^-(D_0^{**} \to D^{(*)+}\pi^-$ decays.* Phys. Rev. D**69**, 112002, (2004).

[99] A Badalian et al. *The Chiral Transitions in Heavy-Light Mesons.* Phys. Rev. D**77**, 074017, (2008).

[100] A Badalian and B Bakker. *Higher Excitations of the D and D_s Mesons.* Phys. Rev. D**84**, 034006, (2011).

[101] X-G Wu and Q Zhao. *The Mixing of $D_{s1}(2460)$ and $D_{s1}(2536)$.* Phys. Rev. D**85**, 034040, (2011).

[102] T Barnes et al. *Q anti-Q G Hermaphrodite Mesons in the MIT Bag Model.* Nucl. Phys. B**224**, 241, (1983).

[103] P Guo et al. *Heavy Quarkonium Hybrids from Coulomb Gauge QCD.* Phys. Rev. D**78**, 056003, (2008).

[104] J J Dudek. *The Lightest Hybrid Meson Supermultiplet in QCD.* Phys. Rev. D**84**, 074023, (2011).

[105] D McManus. *Resonances and Lattice Field Theory.* PhD thesis, School of Mathematics, Trinity College Dublin, (2011).

[106] L Maiani and M Testa. *Final State Interactions from Euclidean Correlation Functions.* Phys. Rev. B**245**, 585, (1990).

[107] M Lüscher. *Volume Dependence of the Energy Spectrum in Massive Quantum Field Theories I: Stable Particle States*, . Comm. Math. Phys. **104**, 177, (1986).

[108] M Lüscher. *Volume Dependence of the Energy Spectrum in Massive Quantum Field Theories I: Scattering States*, . Comm. Math. Phys. **105**, 153, (1987.

[109] M Lüscher. *Signatures of Unstable Particles in Finite Volumes*, . Nucl. Phys. B**364**, 237, (1991).

[110] M Lüscher. *Two Particle States on a Torus and Their Relation to the Scattering Matrix*, . Nucl. Phys. B**354**, 531, (1991).

[111] K Rummukainen and S Gottlieb. *Resonance Scattering Phase Shifts on a Non-Rest Frame Lattice* . Nucl. Phys. B**450**, 397, (1995).

[112] C H Kim, C T Sachrajda, and S R Sharpe. *Finite-Volume Effects for Two-Hadron States in Moving Frames.* Nucl. Phys. B**727**, 218, (2005).

[113] K Polejaeva and A Rusetsky. *Three Particles in a Finite Volume.* Eur. Phys. J. A**48**, 67, (2012).

[114] S He, X Feng, and C Liu. *Two Particle States and the S-matrix Elements in Multi-channel Scattering.* JHEP 0507, 011, (2005).

[115] M T Hansen and S R Sharpe. *Multiple-Channel Generalization of Lellouch-Lüscher Formula.* Phys. Rev. D**86**, 016007, (2012).